uOttawa

L'Université canadienne
Canada's university

FACULTÉ DES ÉTUDES SUPÉRIEURES ET POSTOCTORALES

uOttawa

L'Université canadienne
Canada's university

FACULTY OF GRADUATE AND POSDOCTORAL STUDIES

Marc D. Doumit
AUTEUR DE LA THÈSE / AUTHOR OF THESIS

Ph.D. (Mechanical Engineering)
GRADE / DEGREE

Department of Mechanical Engineering
FACULTÉ, ÉCOLE, DÉPARTEMENT / FACULTY, SCHOOL, DEPARTMENT

Characterization, Modeling and Design of the Braided Pneumatic Muscle

TITRE DE LA THÈSE / TITLE OF THESIS

Atef Fahim
DIRECTEUR (DIRECTRICE) DE LA THÈSE / THESIS SUPERVISOR

Micheal Munro
CO-DIRECTEUR (CO-DIRECTRICE) DE LA THÈSE / THESIS CO-SUPERVISOR

EXAMINATEURS (EXAMINATRICES) DE LA THÈSE / THESIS EXAMINERS

Mojtaba Ahmadi

Nathalie Baddour

Henry Hong (Concordia University)

Michel Labrosse

Gary W. Slater
Le Doyen de la Faculté des études supérieures et postdoctorales / Dean of the Faculty of Graduate and Postdoctoral Studies

CHARACTERIZATION, MODELING AND DESIGN OF THE BRAIDED PNEUMATIC MUSCLE

Thesis submitted

to the Faculty of Graduate Studies

In partial fulfillment of the requirement for
the degree of Doctor of Philosophy in
Mechanical Engineering

By

Marc D. Doumit

September 2009

Ottawa-Carlton Institute for
Mechanical and Aerospace Engineering

University of Ottawa
Ottawa, Ontario, Canada Kn1 6N5

Your file Votre référence
ISBN: 978-0-494-61359-7
Our file Notre référence
ISBN: 978-0-494-61359-7

ABSTRACT

Electrical motors, hydraulic and pneumatic cylinders are traditionally used as actuators. They are very effective for most industrial applications; however, they are not suitable for devices that interact with human beings. Such devices can be medical assisting robots, robotic prostheses for handicapped people and others. To ensure the safety of the user (*i.e.* patient) and the effectiveness of the device, these applications require an actuator that is compliant and physically flexible, yet powerful and of light weight.

The Braided Pneumatic Muscle, a pneumatic linear actuator, is a candidate device that satisfies the above requirements. Although invented in 1941, limited experimental evaluation of the BPM has hindered its applicability until 1961. Moreover, accurate mechanical models and design processes, as well as the issues of proper control of the device, still limits its wide spread application.

This thesis aims to study the Braided Pneumatic Muscle behaviour, develop mechanical models to characterize this as well as to propose a design process that enables the user to select the Braided Pneumatic Muscle size and configuration based on the required muscle force, the muscle contraction distance and the muscle stiffness. In this thesis, a comprehensive experimental evaluation is achieved which led to the discovery of new muscle properties as well as the understanding of muscle behaviour. Moreover, a novel force-based modeling approach has been developed and has resulted in accuracies of the static and dynamic models that are better than those of published analytical models. Furthermore, the muscle's dynamic behaviour has been modeled using linear and non-linear system identification models. Finally, the closed loop behaviour of the Braided Pneumatic Muscle was analyzed with a Proportional Integral Derivative controller.

ACKNOWLEDGEMENT

My PhD thesis represents the fruit of all the years of education that I achieved. This would not have been possible without the support and the encouragement of many individuals. I would like to first express my gratitude to all my teachers and professors throughout the elementary school, high school as well as university.

Specifically, I would like to express my deepest sense of gratitude to my supervisors, Dr. Atef Fahim and Dr. Michael Munro, for their excellent guidance and support throughout this study. I am truly indebted to their mentorship and boundless support that really helped me achieving this goal.

I would also extend my gratitude to the University of Ottawa, Department of Mechanical Engineering faculty members, administrators as well as machine shop staff that has contributed directly or indirectly to this achievement.

I wish also to express my love and gratitude to my beloved family for their understanding, endless support and encouraging through the duration of my studies.

Finally, I must thanks God for giving me the health, love and endurance that are needed to accomplish this goal.

TABLE OF CONTENTS

LIST OF FIGURES

LIST OF TABLES

Chapter 1

INTRODUCTION

The Braided Pneumatic Muscle (BPM) is a pneumatically-powered actuator whose structure and functionality are completely different from the traditional pneumatic cylinders. In its most common configuration, it consists of an elastic bladder, tubular braided mesh and two end fixtures. The braid wraps around the bladder and both are strapped to the end fixtures for sealing of the bladder and securement of the braid. The BPM's operation is simple, as the bladder inflates; the bladder expands in diameter causing the braid angle to steepen which in turn forces the tubular braid to foreshorten. An example of a BPM prototype developed for this work is shown in Figure 1-1.

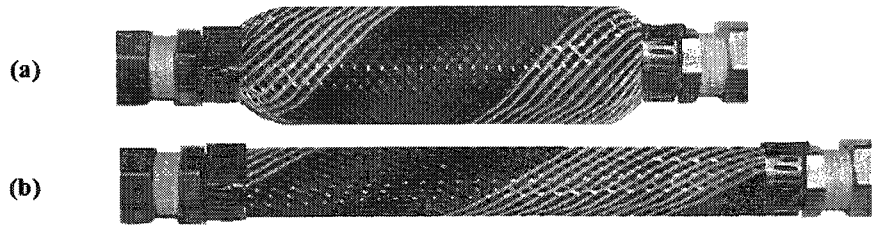

Figure 1-1: BPM prototype: (a) pressurized state (b) deflated state.

Many forms of actuators have been developed for biological muscle-like actuators, namely, electro reactive gels actuators, piezoelectric actuators, ionic polymer-metal composites actuators, shape memory alloy actuators, pneumatic actuators, and others. These actuators are so different that they are difficult to compare to each other. However, the BPM offers a combination of properties that makes it very appealing for biological muscle-like applications. These properties can be characterized as follows:

BPM weight: The main elements of the muscle are a thin braided mesh and an elastic bladder. This makes the device very light. A typical BPM of a length of 30 cm can have a weight range between 0.1 to 0.2 kilogram (including the end fixtures).

BPM force: In spite of its light weight, the muscle produces a substantial force that is approximately six times greater to than that produced by a pneumatic cylinder of the same diameter. This force is mainly a function of the muscle pressure, the muscle diameter as well as the muscle contraction distance. Similar to a biological muscle, the BPM force monotonically decreases to zero as the muscle reaches its maximum contraction distance. A typical BPM of a diameter of 2 cm and a muscle pressure of 200 kPa can produce a force of approximately 800 N.

BPM stiffness: As stated previously, the muscle force is a function of the muscle pressure and the muscle contraction distance and thus, the muscle offers a variable muscle stiffness. A variable muscle stiffness is a positive muscle property that is essential for many applications (*e.g.* legged locomotion). For a range of muscle force, the muscle stiffness can be used to limit the muscle contraction distance.

BPM compliancy: The flexibility of the BPM's outer shell and its inherent pneumatic compliant behaviour permits the muscle to give upon an impact, thus, allowing the BPM to offer a safe interaction with the user.

BPM mechanical connection: The unidirectional contraction distance of the muscle allows for a direct mechanical connection with the apparatus without any transmission mechanism (*e.g.* gear trains). Furthermore, the flexibility of the outer muscle material facilitates a direct mechanical connection without a precise alignment with the apparatus.

BPM speed and bandwidth: The BPM is relatively a fast linear actuator. This is attributed to its unidirectional displacement and its direct mechanical connection (no speed reduction). The BPM speed and bandwidth are functions of the muscle volume, supply pressure and the effective orifice area of the valve that is supplying the air to the muscle.

BPM Contraction distance: The BPM geometrical properties are governed by the tubular braided mesh of the muscle. For a typical BPM, the muscle contraction distance ratio with respect to the muscle original length is approximately 30 %.

Other aspects of the BPM that are important to state are the muscle challenges and disadvantages. Given the muscle fixture design, the BPM can only sustain a limited number of cycling before failure. Moreover, for mobile applications, the air supply tank mass and volume can be a design challenge. However, a container with air stored as a compressed fluid has more energy than a battery of same mass [1]. Finally, the controller design for a BPM pneumatic system can be challenging.

In this study, the BPM is considered for a biological muscle-like application or more precisely, for robotic arm prosthesis. In this case, the muscle design criteria are set such that the muscle maximum force is approximately 1000 N, the muscle contraction range is between 4 to 10 cm and the muscle maximum contraction velocity is approximately 4 cm/s. Based on these requirements, a muscle pressure limit is set to approximately 250 kPa and a pneumatic proportional valve with a specific orifice cross sectional area is selected.

1.1 Objective

The objectives of this thesis are to study the BPM behaviour, develop mechanical models to characterize these behaviours as well as to propose a design process that would allow the user to design or select a BPM that satisfies as set of prescribed requirements. The development of the mechanical models would also allow the sensitivity of geometric, material and control parameters on muscle behaviour to be evaluated.

1.2 Methodology

To achieve the stated objectives, a four step methodology was used to guide the research activities. Firstly, it was deemed important to select and manufacture BPM prototypes. This step included analysis of various BPM structures, BPM materials and BPM operating ranges for obtaining optimum muscle efficiency. Secondly, the BPM properties and behaviours were evaluated by testing prototypes using different experimental setups and operating conditions. After developing a good understanding of the BPM behaviour, the next step included analytical and non-analytical modeling for the BPM static and dynamic operating cases. These models were validated by using BPM prototypes. Furthermore, based on the experimental testing and the analytical models developed, a design process was proposed for selecting the proper BPM prototype. Finally, based on the validated analytical models, a controller was designed to demonstrate the closed loop behaviour of the muscle.

1.3 Contribution of this thesis

- A comprehensive experimental evaluation was performed for understanding the muscle behaviour. More specifically, the muscle contraction distance and the muscle force was extensively studied for different muscle parameters, namely, the original braid length, the original braid diameter, the muscle end fixture size, the muscle hanging mass, the bladder original bladder diameter, and the supply pressure. These experimental results characterize the BPM behaviour.
- Based on the comprehensive experimental evaluation, the end fixture size has been discovered as a factor for the muscle force and the muscle contraction distance. Consequently, this element was included in mechanical models and design process.
- A new analytical geometrical model that is based on a cylinder and two frustum cones has been developed. This model reduced the Normalized Root Mean Square error of the muscle contraction distance from 3.5 % to 1.5 %, as such; it is more accurate than the cylindrical model that is used by most researchers.

- A novel force-based modeling approach that is based on thin-walled pressure theory and netting analysis has been developed. This led to an analytical static model that reduced the Normalized Root Mean Square error of the muscle force by an average of 50 % with comparison to other published analytical models.
- Based on the static model, for the first time, an analytical stiffness model has been developed and experimentally validated for a BPM prototype.
- For the first time, a design process is developed to allow the user to design or select a BPM that satisfies as set of prescribed requirements.
- The static model has been extended to develop the first analytical dynamic model for the BPM. The dynamic model which includes the muscle force, the muscle friction and the muscle fluid dynamics has achieved great accuracy for the muscle steady state phase. Moreover, the model was in a good agreement with the experimental results in the transient phase.
- Linear and non-linear system identification models has been identified and implemented. These models offer an alternative approach for predicting the muscle dynamic behaviour.

1.4 Thesis Outline

This thesis is organized into 10 chapters. Chapter 1 presents an introduction to the BPM, the thesis objective, the adopted methodology as well as the contributions of this thesis. Chapter 2 presents the results of a literature survey. This is organized into categories, namely, BPM historical background, BPM current status and BPM geometrical and mechanical modeling. Moreover, in this chapter, potential research improvements are identified.

Chapter 3 deals with BPM experimental evaluation. The muscle behaviour is analyzed for different operating modes and muscle configurations. Two muscle parameters are extensively used in the analysis; namely, the muscle force and muscle contraction distance. This chapter also includes details of the experimental setups and the muscle development process.

Chapter 4 presents BPM geometrical modeling that is based on a new BPM geometry. Relationships for the muscle contraction distance, muscle surface area, muscle volume, as well as the muscle braid jamming state are derived and experimentally validated.

Chapter 5 exhibits a force-based static model for predicting the muscle force. This model considers thin wall pressure vessel theory, netting analysis as well as experimental evaluation of the BPM's bladder and braid. Moreover, this chapter includes a BPM stiffness model and experimental validation tests for all derived relationships.

Chapter 6 elaborated on a design process for the muscle concentric contraction and the muscle isometric/eccentric contraction. This considers all derived models in this research. The design processes are illustrated using numerical values for the two contraction cases.

Chapter 7 displays a Newtonian-based fully analytical dynamic model for predicting the muscle dynamic behaviour. This includes a linearized model for the muscle pressure, proportional pneumatic valves modeling, dynamic friction modeling and dynamic experimental tests validation for the derived models.

Chapter 8 suggests an alternative solution for predicting the muscle dynamic behaviour. Linear and non-linear system models are used to identify a linear parametric model or an emulator for predicting the muscle dynamic behaviour. Specifically, the linear Auto Regressive models and Neural Network methods are used for this purpose in the chapter. Common algorithms are used for solving the optimization problem for the system models. Finally, experimental validation tests show the accuracy of the system models.

Chapter 9 presents the design and implementation for a linear Proportional Integral Derivative controller for controlling the muscle contraction distance. The controller's robustness is tested with mass disturbances to the system.

Chapter 10 presents conclusions for the thesis. This chapter also presents future research considerations that are recommended for the BPM.

Chapter 2

LITERATURE SURVEY

In this chapter, a literature survey on BPM is presented. Many papers in the open literature simply use the BPM as a purchased component for actuation in their automated apparatus, however, these papers do not offer any BPM testing or modeling. Thus, this survey focuses mainly on the BPM itself. The details are presented in four categories, namely, background of BPMs, BPM analytical and empirical models, BPM experimental testing, and BPM controls. Potential improvements are identified for each of these categories.

2.1 Braided Pneumatic Muscle Background

2.1.1 Historical Background

The earliest reference to what is now known as the BPM is US patent 2238058 "Expansible Cover" invented by Charles R. Johnson and Robert C. Pierce [2] in 1941. The inventors proposed the use of the device as an alternative to dynamite in the mining industry. The Expansible Cover is inserted in a rock seam where its radial expansion would cause the rock to crack open. Their invention did not highlight the longitudinal contraction ability of their device when pressurized. In 1949, De Haven [3] patented the "tensioning device for producing a linear pull", this is a self contained device that is capable of producing a sudden pull when activated. The mechanism is triggered by a charge of gun powder that releases the compressed air within the device. De Haven proposed its application in crash belts apparatus for pilots' safety belts. In 1955, the BPM was rediscovered by Gaylord and subsequently patented as the "fluid actuated motor system and stroking device" [4]. Gaylord proposed the BPM as an alternative actuator to pistons and cylinders given their disadvantages in size, weight and cost. Gaylord's patent 2844126 [4] also provides the first known equation to calculate the force produced by the BPM. The BPM invention was erroneously attributed to the physicist Joseph L. McKibben who popularized its use when he employed it in 1957 to activate a Wrist-Driven Wrist-Hand Orthosis (WDWHO) for his polio stricken daughter. No patent or claim was filed by McKibben with regards to his design. Figure 2-1 shows an application of the McKibben muscle to assist in controlling the fingers of a disabled hand [5].

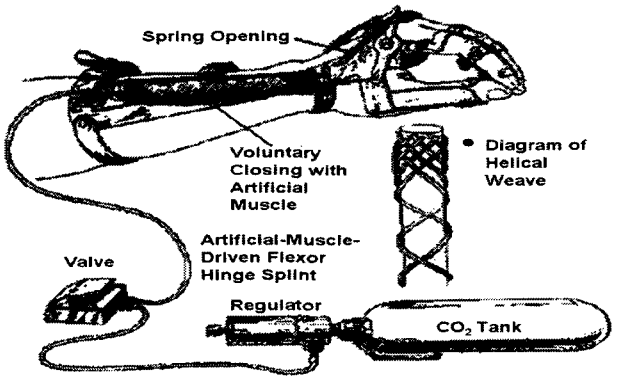

Figure 2-1: McKibben muscle application for an arm orthosis [5].

Although the BPM was perceived as a significant innovation, it had limited success during this era. This was attributed to the BPM's compliant behaviour, the challenges of controlling the BPM pneumatic system, and the large gas tank that is required for applications such as the orthotic arm [5]. Later, starting in the 1980's, researchers and pneumatic equipment manufacturers rediscovered the BPM. The BPM possesses a variable stiffness and a force-length behaviour that can be found in a biological muscle (active mode). Figure 2-2 shows the biological muscle force behaviour as the muscle contracts (active mode) or expands (passive mode) from the muscle original length $L_{m,o}$. With reference to Figure 2-2, the muscle F_m and L_m denote the actual muscle force and length, respectively, where additional subscript o denotes the original state of the muscle. Many researchers sought to imitate the biological muscle by using the BPM as the form of actuation in their mechanical systems.

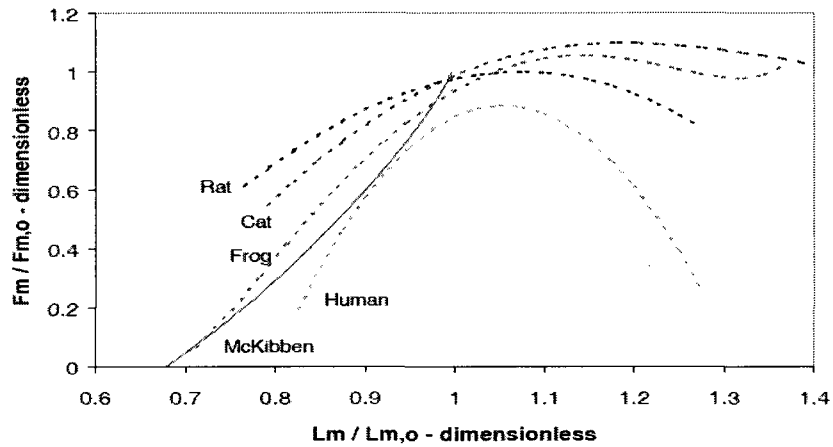

Figure 2-2: Dimensionless isometric contraction results for various animals and the BPM pressurized to 500 kPa [6].

In 1980, Bridgestone Rubber introduced the first commercial BPM for robotic applications. After an unsuccessful market release for their RASC and Soft arm robots [7], their sale stopped in the 1990s. Shadow Robot, a company based in London UK, introduced the Shadow Air Muscle to the market. In addition to individual BPM's, Shadow Robot offers robotic systems that are based on the BPM actuation, *e.g.* the Dexterous Hand shown in Figure 2-3 (a). In 2004, the science fiction movie, "I Robot", featured BPM's as the actuation means for the NS-5 robot (Figure 2-3 (b)). Although the robot appeared in a science fiction context, the robot muscle was inspired by real applications of the BPM, such as the Dexterous Hand by Shadow Robot [8].

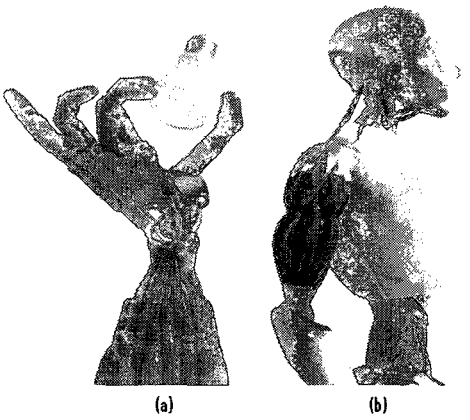

Figure 2-3: (a) Shadow Dextrous Hand from Shadow Robot [8] (b) NS-5 robot from "I Robot" movie [9]

In 2005, the NASA's Robonaut project group [10] ordered the Shadow Dextrous Hand with tactile sensing to be used as technology for their Robonaut development projects. This group of researchers explores robotic technologies that can contribute to an Extra Vehicular Activity (EVA) for astronaut. For the biomedical field, the BPM has been used frequently as a passive or active actuator for medical devices. Figure 2-4 shows a Knee-Ankle-Foot orthosis and lower limb orthosis powered by artificial pneumatic muscles. These robotic orthosis are used for rehabilitation purpose for patients with a spinal cord injury. Moreover, in this lab [8], these robotic orthosis are used to determine how the robotic assistance can affect the metabolic cost of walking for healthy individuals.

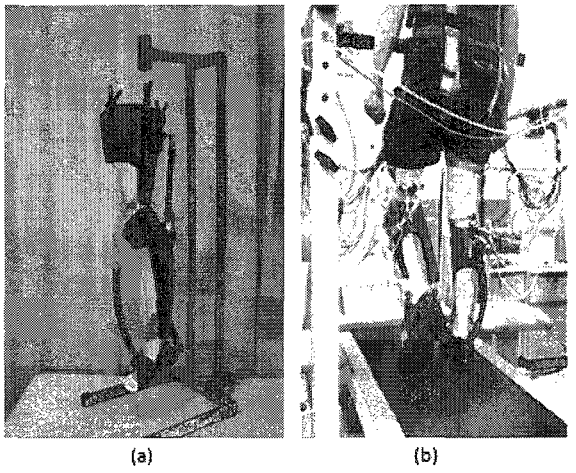

Figure 2-4: (a) Knee-Angle-Foot orthosis [11] (b) lower limb orthosis [12].

2.1.2 Current BPM Status

BPM's are currently manufactured and marketed by two companies, namely, Festo Corporation and Shadow Robot. Each company offers the BPM in different configurations and sizes as shown in Figure 2-5.

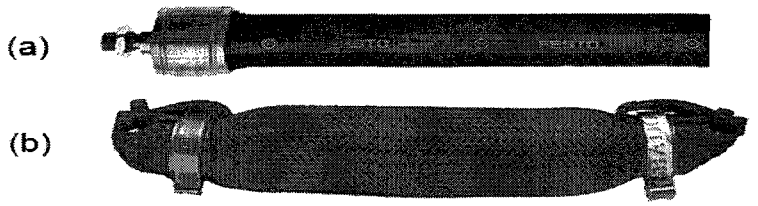

Figure 2-5: (a) The Fluidic Muscle (DMSP) from Festo Corporation [13] (b) The Air Muscle from Shadow Robot Company [8].

The current successful implementation of BPM's lies in fields where other actuators, such as electrical motors and hydraulic cylinders, are not feasible. In 2001, Caldwell et al. [14] proposed the usage of a BPM powered manipulator for retrieval of radioactive material from underwater storage ponds. Such a specific case is governed by precise actuator requirement, such as high power-weight ratio, compliant behaviour, spark free operation and safe interaction with human.

2.2 Braided Pneumatic Muscle Modeling

Modeling is one of the greatest challenges for success of the BPM. Due to muscle hysteresis (the energy loss during a muscle contraction and relaxation cycle) and time-dependant properties, a mathematical model that accurately predicts the muscle behaviour must be non-linear and its development is challenging. The following section presents contributions from researchers towards the development of adequate BPM mechanical models. These contributions are categorized under different subcategories, namely, BPM geometrical modeling, BPM jamming state modeling, BPM static modeling, BPM dynamic modeling, BPM friction modeling, BPM bladder modeling as well as BPM fluid dynamic modeling.

2.2.1 BPM Geometrical Model

The BPM geometrical model forms the basis for any BPM mechanical model. This model defines the muscle geometrical properties such that the muscle motion can be predicted. In 1961, Schulte, Adamski, and Pearson [15] proposed the first model that is based on the muscle cylindrical form assumption. This assumes that the BPM retains a cylindrical shape at all times during operation. An identical approach was also adopted by Chou and Hannaford [16] in 1996. The muscle geometrical relationships are derived by analyzing a fibre within a braided mesh as shown in Figure 2-6.

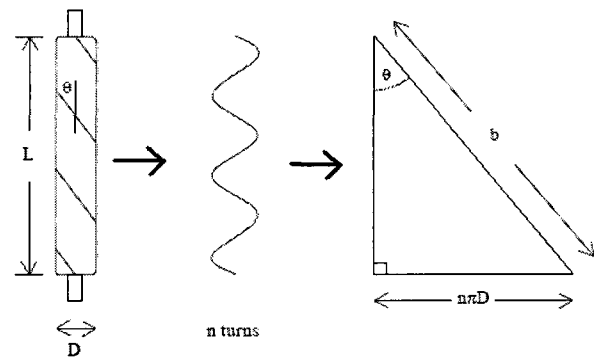

Figure 2-6: Geometrical analysis of a fibre in a braided mesh [16].

With reference to Figure 2-6, θ is the braid angle (angle of fibre with respect to longitudinal axis of muscle), n is the number of fibre revolutions per braid length L, b is the length of the uncoiled fibre and D is the muscle diameter. The BPM geometrical relationships are given by:

$$L = b\cos\theta \tag{2-1}$$

$$D = \frac{b\sin\theta}{n\pi} \tag{2-2}$$

In 1997, Caldwell, Medrano-Cerda, and Bowler [17] adopted an alternative approach for deriving the BPM geometrical model. Their approach was based on the trapezoidal geometry formed by the braided fibres (Figure 2-7). Assuming that the number of trapezoids A and B, within the braid length and circumference, respectively, are known, the muscle length L and diameter D are given by:

$$L = 2 * A * l * cos\,\theta \tag{2-3}$$

$$D = 2 * B * l * \sin\theta \tag{2-4}$$

where l is the trapezoidal length and θ is the braid angle.

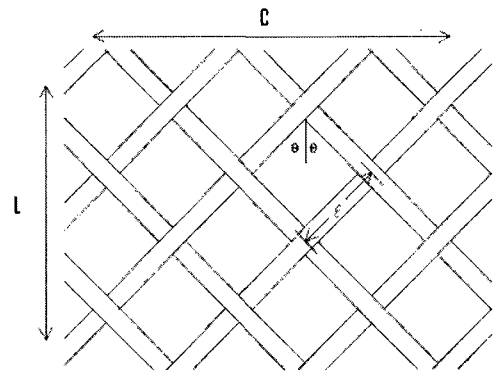

Figure 2-7: Parallelogram muscle braid geometry analysis by Caldwell et al. [17].

If the undulations due to the cross fibre weave are ignored, and cross fibres are assumed to lie flat on top of each other, both models in this section are identical. However, Chou and Hannaford's model is more practical since it is not feasible to measure the number and the length of trapezoids within a braided mesh.

2.2.2 BPM Jamming State Model

As with any open braid, the BPM features two jamming states that occur at both maximum muscle contraction and relaxation. These states represent the physical limits of the muscle operating motion. In 2006, Davis and Caldwell [18] are the first researchers to derive an analytical relationship that predicts these jamming states based on the BPM geometrical properties. Their modeling approach was based on the BPM trapezoidal geometry shown in (Figure 2-7). The contracted jamming state angle θ_{min} is given by:

$$\theta_{min} = \frac{sin^{-1}\left(\frac{D_s N}{\pi D_{90^o}}\right)}{2} \tag{2-5}$$

where D_{90^o} is the muscle diameter when the braid angle is 90°, D_s is the fibre diameter, and N is the number of fibres in the braid.

2.2.3 BPM Static Model

The BPM static model predicts the muscle force in static cases (*e.g.* muscle isometric type of contraction). Designers would use this model to select the BPM size and configuration in light of the muscle force requirement. The first BPM force analysis was that of Gaylord in his 1958 patent [4]. Gaylord found that the muscle force F is a function of the muscle pressure P and the braid angle θ:

$$F = \frac{P\pi D_{90^o}^2}{4}(3cos^2\theta - 1) \tag{2-6}$$

Gaylord had not specified the modeling approach and Equation (2-6) was given as is. In 1961, Schulte, Adamski and Pearson [15] derived the tensile force T which is equivalent to the muscle force F by considering the total longitudinal component of the tension in the braid t_t, the longitudinal force of the bladder t_r, the force of the pressure acting on the ends of the tube t_p, and the frictional forces t_f as follows:

$$T = t_t + t_r - t_p - t_f \tag{2-7}$$

The forces t_t and t_r are determined by the muscle circumferential forces F'' and F', respectively, as follows:

$$2F'' = P''(projected\ area) = P''(DL) \tag{2-8}$$

$$2F' = P'(DL) \tag{2-9}$$

where P'' and P' are the partial muscle pressures that are applied on the braid and bladder, respectively, D is the muscle diameter, and L is the muscle length. The forces t_p and t_f are given as follows:

$$t_p = P\pi\frac{D^2}{4} \tag{2-10}$$

$$t_f = (u_t + u_s)N_f \tag{2-11}$$

where u_t is the coefficient of friction between the braid and the bladder, u_s is the coefficient of friction between the fibres of the braid, and N_f is the normal force between the surfaces. If the muscle bladder and frictional forces are ignored, Equation (2-7) would be identical to those from Equation (2-6). Schulte et al. are not able to validate the derived model (Equation (2-7)) and they have stated that "in view of the finding of this study, prediction of the tensile force-length characteristics for the BPM by analytical methods was set aside in favor of the empirical methods used"[15]. Schulte et al. proposed two empirical equations to predict the muscle force, one for the muscle pressure range of 138 kPa to 345 kPa and the other for 345 kPa to 620 kPa.

In 1996, Chou and Hannaford [16] presented a model based on the principle of virtual work. Assuming that the BPM system is lossless, has no energy storage in its elastic wall, has zero-wall thickness, and retains a cylindrical shape, the muscle force relationship is given by:

$$dW_{out} = dW_{in} \tag{2-12}$$

$$-FdL = PdV \tag{2-13}$$

where, dW_{out} is the system output energy, dW_{in} is the system input energy, F is the muscle force, dL is the muscle length variation and dV is the muscle volume variation. Using Equations (2-1), (2-2) and (2-13), Chou and Hannaford derived their first BPM static model as follows:

$$F = \frac{P\pi D_{90^o}^2}{4}(3cos^2\theta - 1) \tag{2-14}$$

This model is identical to Gaylord's model given by Equation (2-6). Chou and Hannaford proposed to improve the model described in Equation (2-14) by taking into account the muscle membrane thickness; however, they described the new model as more accurate but more complex. This led Chou and Hannaford to consider a simplified model that would consider the BPM as a variable-stiffness elastic element or a gas spring. This model is given by:

$$F = K_g P'(L - L_{min}) \tag{2-15}$$

where K_g is a muscle stiffness constant per unit pressure approximated over a muscle contraction distance range and L_{min} is the minimum length when the muscle force is null. Additional parametric terms are added to consider the energy stored in the BPM bladder and braid and to adjust for the BPM non-cylindrical shape, the new model resulted in:

$$\begin{aligned} F &= K_g(P' - P_{th})(L - L_{min}) + K_p(L - L_o) + nl(L) \quad if\ P' > P_{th} \\ F &= K_p(L - L_o) + nl(L) \quad if\ P' \leq P_{th} \end{aligned} \tag{2-16}$$

where P_{th} is the threshold pressure to overcome the bladder elasticity, K_p is the linearized passive elastic constant for the shearing force of the bladder material and braid and *nl(L)* is a nonlinear term reflecting the non-cylindrical shape of the muscle. The parameter values for this model are estimated using experimental results to fit the model results. Based on their experimental evaluation, Chou and Hannaford also concluded that coulomb friction was the dominant type of friction and suggested adding a constant friction force of 2.5 N that opposes the muscle motion. Chou and Hannaford did not present the accuracy of any of their models, however, Davis et al. [19] stated that both analytical static models derived by Chou and Hannaford exhibit approximately 15 % error between the modeled response and the measured data.

In 2000, Tsagarakis and Caldwell [20] proposed two BPM static models that are based on the principle of conservation of energy. Their first prediction is identical to Equation (2-6) with the exception of a muscle end cap force term. Tsagarakis and Caldwell claimed that the force acting on the muscle end cap should be subtracted from the muscle force. The model considers that the input energy is transformed into two resulting forces and a displacement. The two force components are the radial forces created by the muscle pressure on the muscle walls and the expansion forces created by the muscle pressure at each end cap of the muscle. The muscle force F is given by:

$$F = F_{cont} - F_{exp} \tag{2-17}$$

where F_{cont} is the muscle force portion resulting from the loading on the muscle walls and F_{exp} is muscle force portion resulting from the loading on the end caps (Figure 2-8).

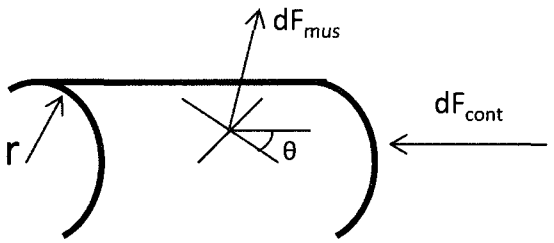

Figure 2-8: Muscle force analysis by Tsagarakis and Caldwell [20]

Assuming a system conservation of energy, the energy consumed by expanding the muscle dW_{mus} is equivalent to the energy that is required to contract the muscle dW_{cont}. The relationships are as follows:

$$dW_{cont} = F_{cont}(-dL) \tag{2-18}$$

$$dW_{mus} = F_{mus}dr \tag{2-19}$$

where, dL and dr are the muscle length and the muscle radius variance, respectively. Using Equations (2-18), (2-19) and the muscle geometrical relationship (Equations (2-1) and (2-2)), Tsagarakis and Caldwell determined the muscle force as follows:

$$F = \frac{\pi D_o^2 P}{4}(3cos^2\theta - 1) \quad if\ \theta > sin^{-1}\frac{D_{cap}}{D_o} \tag{2-20}$$

$$F = \frac{\pi P}{4}\left(2D_o^2 cos^2\theta - \mathrm{D}_{\mathrm{cap}}^2\right) \quad if\ \theta < sin^{-1}\frac{D_{cap}}{D_o} \tag{2-21}$$

where D_{cap} is the end cap diameter. Similar to Chou and Hannaford, their second model incorporates the muscle wall thickness. In order to further improve their model accuracy, Tsagarakis and Caldwell adopted an integration technique to determine an accurate end muscle surface area. Based on experimental results for a rubber liner, they determined a stress relationship for rubber material that considers the hoop elasticity of the muscle bladder. Finally, based on the scheme revised by Chou and Hannaford, they estimated a constant friction force of 70 N for the model. Based on model simulation and experimental results, Tsagarakis and Caldwell claim that their final model achieved an accuracy that is 30 to 50 % better than that of the Chou and Hannaford model in [16].

In 2000, Tondu and Lopez [21] modeled the BPM using the conservation of energy principle but adopted a different approach from other authors. They split the muscle internal loading into a lateral and an axial component. Using the virtual work principle, they formulated the following relationship:

$$\delta W_{Lateral\,pressure} + \delta W_{Axial\,pressure} + \delta W_{Equilibrium\,force} = 0 \tag{2-22}$$

where the work by the lateral pressure $W_{Lateral\,pressures}$ is the loading on the muscle walls time its radial expansion, the work of the axial pressure $W_{Axial\,pressure}$ is the loading on muscle cap times the muscle end displacement and the work of the muscle force $W_{Equilibrium\,force}$ is the muscle force times the muscle end displacement. Mathematically this is given by:

$$(2\pi rlP)(+\delta r) - (\pi r^2 P)(-\delta l) - F(-\delta l) = 0 \tag{2-23}$$

where r is the muscle radius, P is the muscle pressure, l is the muscle length, δr is the muscle radius variance, δl is the muscle length variance and F is the muscle force. Using Equations (2-23), (2-1) and (2-2) Tondu and Lopez derived the following relationship for the BPM static model:

$$F(\alpha, P) = \left(\pi r_{90^o}^2\right) P[3cos^2\alpha - 1] \tag{2-24}$$

where α is the fibre braid angle. This relationship is identical to Equation (2-6). Once again, in order to improve the accuracy of the developed model, Tondu and Lopez introduce a new factor k that models the muscle non-cylindrical form as follows:

$$F(\epsilon, P) = \left(\pi r_{90^o}^2\right) P[a(1 - k\epsilon)^2 - b] \tag{2-25}$$

where ε is the muscle contraction ratio. The value of the new parameter k is estimated based on experimental data. From model validation results, Tondu and Lopez concluded that this model is inaccurate at low pressures (less than 200 kPa). This is attributed to bladder rubber elasticity and the interaction between the braid and the bladder. In order to further improve the accuracy of their model, they incorporated additional parameters that are functions of muscle pressure. Again, the new parameters are estimated experimentally. Finally, Tondu and Lopez developed a friction model that is a function of fibre to fibre contact surface and muscle pressure. The friction model was also fine tuned using experimental data. The final model results are shown

graphically as to have greater accuracy compared to their original model. This must be calculated by estimating values from their figures.

In 2002, Davis et al. [19] stated that all model refinements achieved in references [16], [20], [22] & [23] have substantially improved the static model but there is still a significant error when the muscle is operated at high pressure (450 kPa). Davis et al. claim that the braid fibres go through a deformation which is a function of muscle pressure and muscle geometry. Assuming that the fibres deformation occurs due to longitudinal muscle force and muscle radial forces, the length of a single fibre b is calculated as follows:

$$b = b_{min} + \delta b_{long} + \delta b_{rad} \tag{2-26}$$

where b_{min} is the fibre length when the BPM is deflated, δb_{long} is the fibre length deformation due to the muscle force and δb_{rad} is the fibre length deformation due to the radial loading on muscle walls. Davis et al. claim that when Equation (2-26) is used to calculate the muscle length, the predicted muscle force is more accurate than any of the previous models. To validate this, a muscle prototype having a length of 1.77 m, 450 strands and a strand diameter of 0.2 mm was tested. However, the graphical results in [19] show that the new model reduced the muscle force error by Equation (2-14) approximately from 15 % to 8 %.

All the existing BPM static models have been based on virtual work or conservation of energy principles with the exception of the original work of Schulte et al. The implementation of these principles neglects all system losses. All authors added experimentally estimated parameters to validate the BPM experimental data, however, this approach makes the BPM static model valid for a specific BPM only.

2.2.4 BPM Dynamic Model

The BPM dynamic model predicts the muscle motion as a function of time. Such a model is necessary for BPM design for the muscle concentric contraction case. In 2000, Tondu and Lopez [21] further modified the aforementioned static model by including a BPM dynamic force F_{dyn} for the case of the BPM suspended vertically. This term takes into consideration the muscle force F and the friction forces as follows:

$$F_{dyn} = F - f_f \tag{2-27}$$

The muscle motion governing equation is given by:

$$F_{dyn} - mg = m\ddot{x} \tag{2-28}$$

where f_f is the muscle friction, m is the mass of the hanging load, g is the gravitational constant and x is the muscle contraction distance. The parameters of this lumped model are selected and adjusted based on experimental results. Figure 2-9 shows the model and the experimental results for a muscle prototype having a length of 30 cm and a radius of 1.4 cm for a braid angle of 20 degrees. In this test, the muscle is subjected to a supply pressure of 400 kPa while carrying a mass of 30 kg. The model in [21] has an estimated normalized accuracy ranges of 0 % to 12 % and 0 % to 7 % for muscle force and muscle contraction distance, respectively.

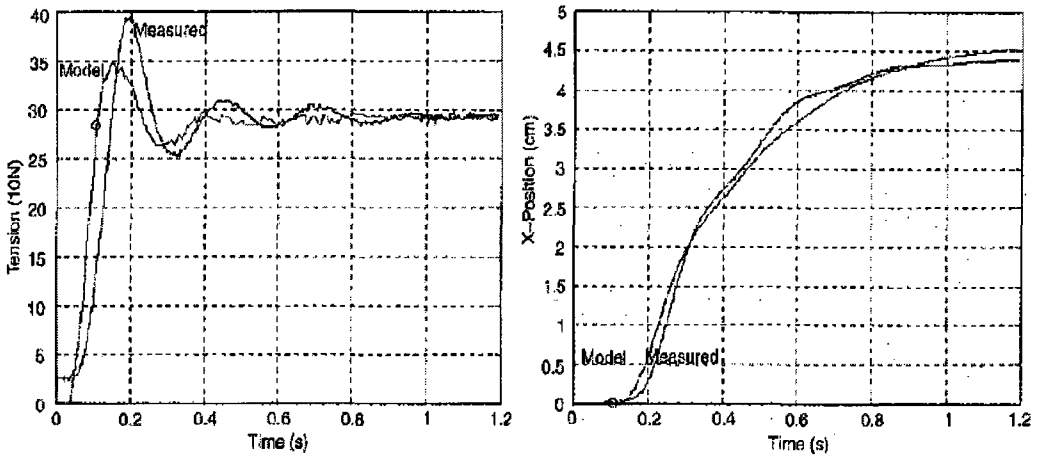

Figure 2-9: Experimental and dynamic model results for the net muscle force (tension) and the muscle contraction distance (X-position) [21].

In 2001, Thongchai, Goldfarb, Sarkar and Kawamura [24] adopted a frequency modeling approach to predict the dynamic behaviour of a BPM set. Using the Intelligent Machine Architecture (IMA) framework, Thongchai *et al.* succeeded in developing three linear third order dynamic models, each for a specific frequency range. The open loop accuracy of the developed models has not been reported.

In 2002, Petrovic first developed a static model based on the virtual work principle [25]. Assuming the BPM to be a gas spring with a non-linear stiffness and incorporating the system inertial and frictional forces, the static model is transformed to a dynamic model as follows:

$$M\ddot{q} + \mu(q, \dot{q})p + f(q)p = \tau \tag{2-29}$$

where M is the mass of the system, p is the muscle pressure, q is the muscle contraction distance, $\mu(q, \dot{q})p$ denotes the lumped model of the total system friction forces, $f(q)p$ denotes the relationship for the static actuating force (muscle force), and τ is the dynamic actuating force. Petrovic gave no indication as to the accuracy of this model.

Later in 2003, Reynolds, Repperger, Phillips and Bandry [26] developed a BPM dynamic model based on the Voigt Viscoelastic model. The model consists of a mechanical spring, dashpot and a contractile force element in parallel (Figure 2-10).

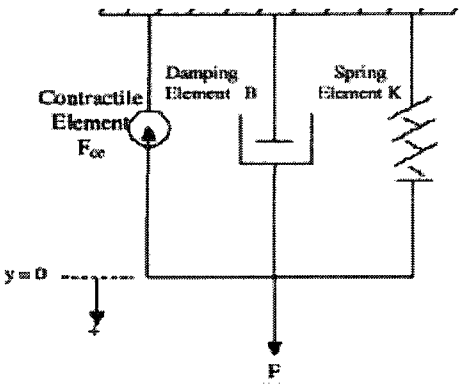

Figure 2-10: Dynamic model configuration [26].

The proposed mechanical configuration (Figure 2-10) gives the following relationship:

$$M\ddot{y} + B\dot{y} + Ky = F_{ce} - Mg \tag{2-30}$$

where M is the load mass, B is the system damping coefficient, K is the spring stiffness constant, and F_{ce} is the effective force provided by the contractile element. The values of these parameters are identified experimentally for a step perturbation of the load at constant pressure. Two lumped parameter models are derived to predict the BPM motion in the contraction and in the relaxation phases. The developed models are experimentally validated for a triangular wave input of muscle

pressure between 55 kPa and 124 kPa (Figure 2-11). Reynolds *et al.* [26] determined their models accuracy is 15 % with respect to the average muscle contraction distance. This accuracy is calculated based on the normalized root mean square error.

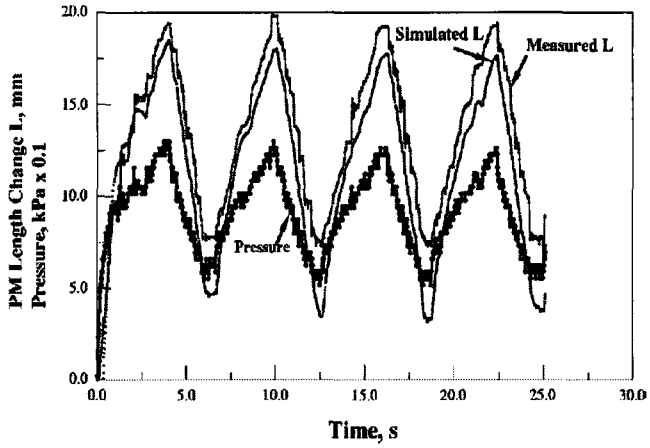

Figure 2-11: Experimental and dynamic model results for the muscle pressure for a triangular wave input of muscle pressure between 55 and 124 kPa [26].

Sanchez, Mahout and Tondu [27] recognized the challenges in developing an analytical BPM dynamic model; instead, they proposed the damped Gauss-Newton algorithm as an estimator for achieving a nonlinear parametric identification for the BPM. The schematic diagram of this modeling process is shown in Figure 2-12. Sanchez et al. claim that this method considers the BPM mechanical behaviour in the model structure; however, this is not explained in the paper. The authors concluded that they have achieved acceptable prediction of BPM dynamics. Figure 2-13 shows the muscle contraction distance as a function of time. Sanchez et al did not provide any information about the physical characteristic of the muscle or the step perturbation introduced to the system.

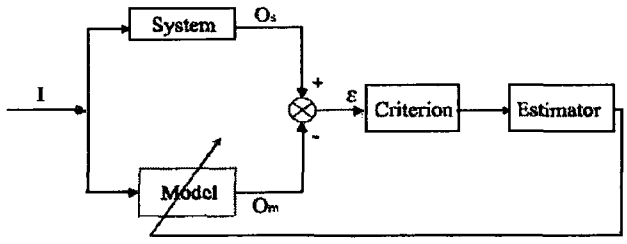

Figure 2-12: Modeling schematic for the BPM nonlinear parametric identification [27].

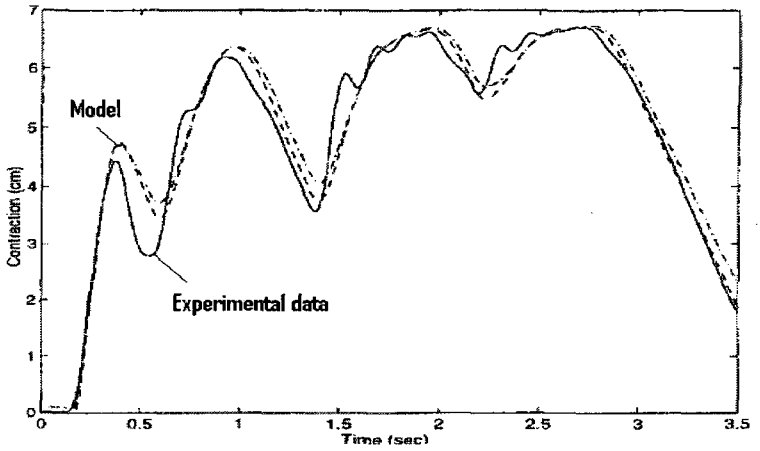

Figure 2-13: Experimental and dynamic model results. The physical characteristic of the muscle and the step perturbation introduced to the system are unknown [27].

The literature reviewed for the BPM dynamic models are either empirical in nature or are gross approximations with parameters fitted using experimental data. Furthermore, none of these models includes the fluid dynamics of the pressurized gas and its analysis in the derivation.

2.2.5 BPM Friction Model

The muscle friction represents the main source of the loss of energy for the BPM and, as such, its modeling is important for achieving an accurate BPM static or dynamic model. Very few researchers have investigated thoroughly the effect of muscle friction. The main challenges for modeling the friction are the identification of the type of friction, the source of the friction and the surface area over which the friction acts. Two types of friction exist for the BPM, namely, static and dynamic. The source for the friction has been identified by Chou and Hannaford [16] to be the fibre to fibre contact, fibre to bladder contact, and the changing shape of the bladder. Chou and Hannaford have demonstrated experimentally that the muscle hysteresis is unchanged for different muscle contraction velocities. This result led Chou and Hannaford to conclude that the muscle hysteresis is dominated by coulomb friction. Several methods have been adopted to model the static friction of the muscle. Some researchers including Chou and Hannaford have recognized the difficulty of modeling the friction. From experimental testing, Chou and Hannaford identified a constant friction value of 2.5 N [16]. This value is added to the BPM

static model when the muscle is expanding, or subtracted from the static model, if the muscle is contracting. Schulte et al. [15] estimated the muscle friction as a function of the muscle surface area, the coefficient of friction between the braided mesh and the bladder u_t, the coefficient of friction between the fibres of the braided mesh u_s and the normal force between the surfaces N as follows:

$$t_f = (u_t + u_s)N \tag{2-31}$$

The normal force is calculated as follows:

$$N_f = P''(LD) \tag{2-32}$$

where P'' is the partial muscle pressure that is applied on the braid. Tondu and Lopez [22] have specified the source of friction as fibre to fibre contact. They claimed that, during muscle operation, the fibres of the braid are locked with the bladder and thus no sliding occurs between them. Therefore, the friction relationship is given by:

$$\left|F_{static\ friction}\right| = f_s S_{contact} P \tag{2-33}$$

where f_s is the static friction coefficient, $S_{contact}$ is the fibre to fibre contact surface and P is the muscle pressure. The fibre to fibre contact surface is determined by defining the surface area for an elementary surface (pantograph networks) as a function of the braid angle. The total contact surface is derived as a function of the initial muscle surface area (jamming state) as follows:

$$S_{contact} = (2\pi r_o l_o)\frac{S_{elem\ current}}{S_{elem\ init}} \tag{2-34}$$

where $S_{elem\ init}$ is the contact surface formed by the pantograph (Figure 2-14 (a)) at the deflated state condition and $S_{elem\ current}$ is the contact surface formed by the pantograph (Figure 2-14 b) at a particular braid angle.

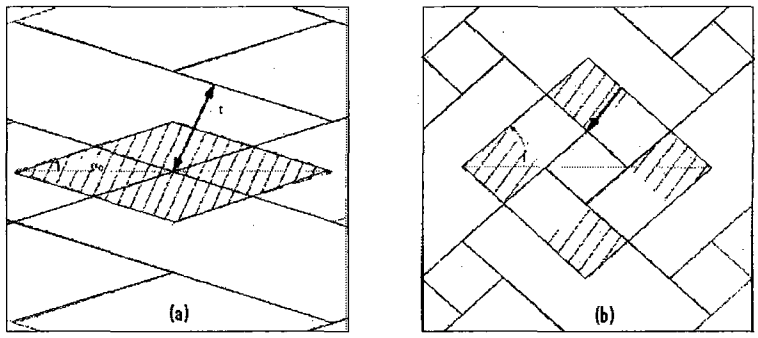

Figure 2-14: Contact surface pantograph analysis: (a) unstressed muscle condition (b) current muscle condition [22].

Using experimental data, Tondu and Lopez concluded that the calculated static friction coefficient was too low compared to the theoretical coefficient for the braid material. It was then estimated that only 1/13 of $S_{contact}$ corresponds to the actual fibre to fibre surface contact. This is attributed to the curved shape of the braid threads. Thus, the friction model is transformed to:

$$|F_{static\ friction}| = f_s\left(\frac{1}{13}\right)S_{contact}P \tag{2-35}$$

where $F_{static\ friction}$ is the BPM static frictional force. Tondu and Lopez's friction model assumes that there is a linear motion between fibres. Davis and Caldwell [18] are in an agreement with Tondu and Lopez's physical interpretation of the fibre to fibre contact surface. However, Davis and Caldwell [18] proposed an analytical approach to determine the ratio S_{scale}. This approach is based on Hertzian contact area theory done by Brydson [28]. Davis and Caldwell assumed that the fibres S_{scale} value is similar to the contact surface ratio between two spheres and between two disks of similar diameters. The governing equation is given by:

$$S_{scale} = \frac{D_s}{1.442\left(F_{comp}.\frac{D_s}{2}.Ce\right)^{\frac{1}{3}}} \tag{2-36}$$

where D_s is sphere diameter, F_{comp} is the force between the two fibres and C_e is a constant which is a function of the fibre Poisson's ratio and Young's modulus. Based on the derived S_{scale} relationship (2-36) , Davis and Caldwell determined this ratio to be 18.1 and 15.8 for a 200 kPa and 300 kPa supply pressures, respectively. Davis and Caldwell claim that such results match the ratio value obtained experimentally within 10 %.

2.2.6 BPM Bladder Model

The BPM bladder is a major physical component for the muscle; however, its mechanical contribution to the muscle is limited since most commonly used bladder materials have a very low elastic modulus. In 2000, Klute et al. [29] are the first authors to propose an analytical model for the muscle bladder based on a non-linear material model developed by Mooney and Rivlin in the 1940s. The model is based on the relationship proposed by Mooney and Rivlin which models the relationship between the stress σ, the strain ε, and the strain energy constant w as follows:

$$\sigma = \frac{dw}{d\epsilon} \tag{2-37}$$

The bladder relationship was incorporated in Chou and Hannaford static model (Equation (2-14)). This resulted in a complex mathematical relationship [29]. The results of this new model showed an improvement in accuracy when compared to the original model but there are still differences between the model and experimental results. Klute et al. suggested that the elastic energy storage of the system should be considered along with other factors in order to achieve optimum results. It is important to note that in this work, Klute et al. are using a natural latex rubber bladder which was typically much stiffer than average rubber tubes. Schulte et al. [15], Chou and Hannaford [16] and Tsagarakis et al. [20] proposed empirical models to include the bladder mechanical behaviour. In all cases, an elastic constant has been used for the bladder such that the bladder mechanical contribution is calculated.

2.2.7 BPM Fluid Dynamic Modeling

Based on a literature search, no researchers have developed a BPM model that considers the BPM fluid dynamic modeling; more specifically, a model that would predict the non-linear muscle pressure as a function of the muscle volume, muscle contraction distance, input flow rate and output flow rate. Chou and Hannaford [16] modeled the pneumatic circuit that feeds the BPM in their physical setup. They claimed difficulty in modeling the pneumatic circuit (Figure 2-15) since it is a distributed-parameter system and it is very sensitive to geometry changes.

Therefore, Chou and Hannaford adopted a lumped parameter model for the pneumatic circuit. The electro-valve modeling was not included since it was claimed to be complex to derive.

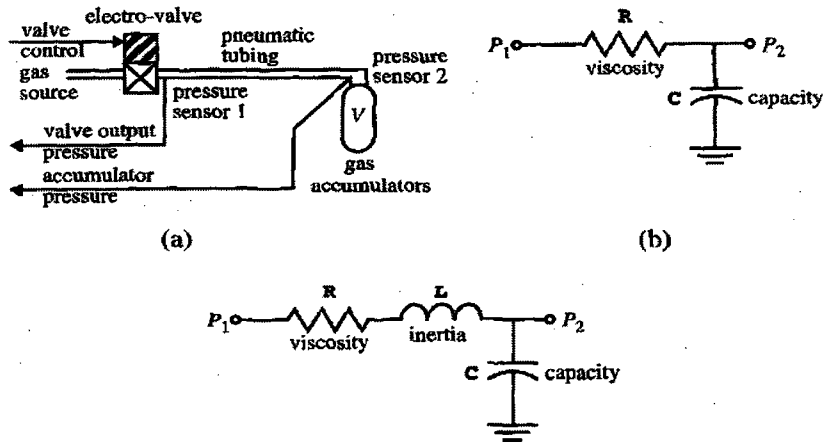

Figure 2-15: Schematics for (a) pneumatic circuit, (b) lumped parameter model with resistor and capacitance, and (c) lumped parameter model with gas inertia factor [16].

By neglecting the volumes of the tubes that supplies the air to the BPM, Chou and Hannaford modeled the pneumatic circuit as a resistance-capacitance network as shown in Figure 2-15 (b). The flow was derived as a function of the pressure drop in the tube and the resistance R as follows:

$$\frac{P_1 - P_2}{R} = w \tag{2-38}$$

where P_1 and P_2 are the input and output pressure of the pneumatic circuit, respectively. The flow is also modeled as a function of the capacitance C and P_2 as follows:

$$w = -C\frac{dP_2}{dt} \tag{2-39}$$

Using Equations (2-38) and (2-39), a first order system is modeled as follows:

$$P_1 - P_2 = RC\frac{dP_2}{dt} \tag{2-40}$$

By using the resistor relationship and adding the gas inertia factor to the pneumatic circuit model, Chou and Hannaford obtained the following relationship:

$$P_1 - P_2 = R_1\left(\frac{w}{\rho_t A_t}\right) + R_2\left(\frac{w}{\rho_t A_t}\right)^2 + L\frac{dw}{dt} \tag{2-41}$$

where ρ_t is the gas density and A_t is effective cross-sectioned area of tube and connectors.

2.3 BPM Experimental Evaluation

The BPM experimental evaluation is an important step in understanding the muscle's behaviour. Schulte et al. [15] are the only authors that have conducted a comprehensive BPM experimental evaluation. Surprisingly, this contribution is seldom quoted by others. Schulte et al. built five different prototypes that varied in size and braid type. Their experimental testing revealed many findings that are stated below:

The muscle force behaviour varies as the ambient temperature varies. The experimental results showed that the maximum muscle force dropped by 5 % as the ambient temperature increased from 21.1 °C to 32.2 °C (the muscle pressure was 280 kPa). This was attributed to the change in the material properties of the braid nylon with temperature.

Typically, the BPM starts contracting or generating a muscle force only after it is partially inflated. Thus some gas is exhausted without creating any work. Schulte et al. proposed to replace this dead volume by an aluminum plug and thus reduce the gas consumption. This would extend the life span of the compressed gas tank.

Numerous muscle isometric contraction tests for different BPM prototypes sizes are accomplished. This allowed Schulte et al. to conclude that the muscle force is a function of the muscle diameter and the muscle pressure. Thus, the greater the muscle diameter and pressure, the greater the muscle force.

Gaylord et al. used two different types of weave for the BPM, namely, a single and a double crossing of fibres. There was no apparent difference in behaviour of the different braids.

Gaylord et al. also analyzed the muscle behaviour as the braid density was varied when the braid was originally manufactured, namely tight, loose, and very loose braids. It was found that with a very loose braid, the BPM contracted to a greater length. The tight braid configuration allowed limited motion and thus a small BPM contraction distance.

The BPM efficiency has been rarely determined by researchers. Chou and Hannaford [16] are the first and only authors to do this. They experimentally determined the BPM efficiency for a quasi-stationary and isotropic shortening case as shown in Figure 2-16.

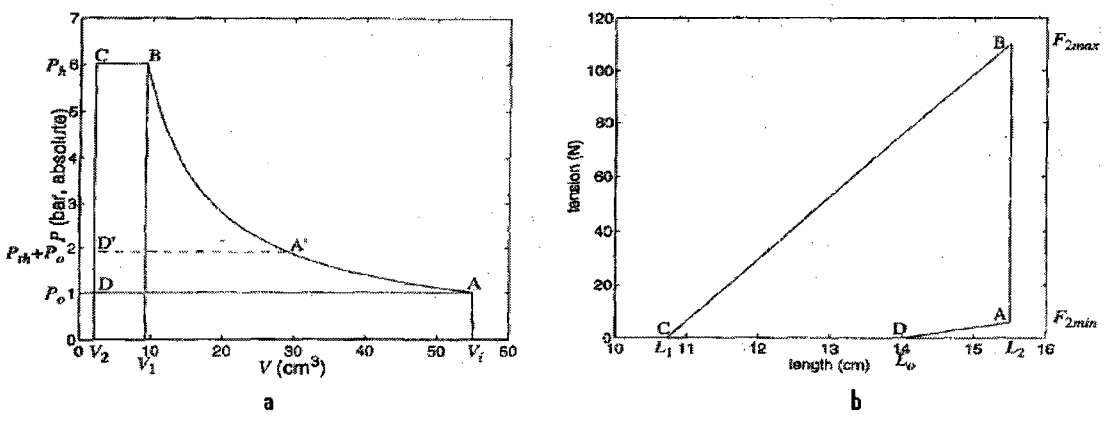

Figure 2-16: Chou and Hannaford BPM efficiency for quasi-stationary and isotropic shortening: (a) Pneumatic cycle of hypothetical compressor, and (b) Mechanical cycle of actuator **[16]**.

In the two cases, the muscle was inflated by a compressor with a known volume from *A* to *B*, allowed to contract from *B* to *C* till the muscle force was zero, deflated from *C* to *D* to the original pressure and finally, filled by a compressor (from *D* to *A*) to return to the initial condition. The efficiency E_a was determined as follows:

$$E_a = \frac{W_a}{W_{01} + W_{12}} \tag{2-42}$$

where W_a is the actuator output energy determined by the surface area composed by the curve *ABCD* in Figure 2-16 b, W_{01} is the input energy determined by the supply pressured air in step *A* to B and W_{12} is the input work from *B* to *C*. Chou and Hannaford determined the maximum efficiency to be approximatively 30 %.

A number of researchers made structural modifications to the BPM in order to improve its efficiency and behaviour. Davis, Tsagarakis, Canderle and Caldwell [19] recognized the BPM bandwidth (cut-off frequency) limitation and proposed to reduce the capacitance of the system (muscle volume). The BPM bandwidth corresponds to the frequency range in which the actuator could feasibly function; the greater the bandwidth, the faster the BPM operates. Davis et al. tested and analyzed three types of fillers for the BPM. The fillers are granular (5 mm in length and 2 mm in diameter), solid (solid tubes of same diameters as BPM dilated jamming sate) and liquid (water). Results showed 55 %, 250 % and 400 % bandwidth improvement by using granular, solid, and liquid fillers, respectively. These results illustrate great improvement in muscle operation; however, the authors explained that such additions might introduce complexity and system design challenges. It is important to keep the filler in the muscle away from the inlet and outlet muscle orifices. A filler has the same effect as the aluminum plug proposed by Schulte et al. [15].

The biological muscle differs from a BPM in numerous aspects; mechanically, the most relevant difference is the viscous damping that governs the relationship between the biological muscle force and the contraction speed. Figure 2-17 shows the biological muscle and the skeletal models results for the dimensionless load vs. the dimensionless velocity range for four different animals and four published biomechanic models [6].

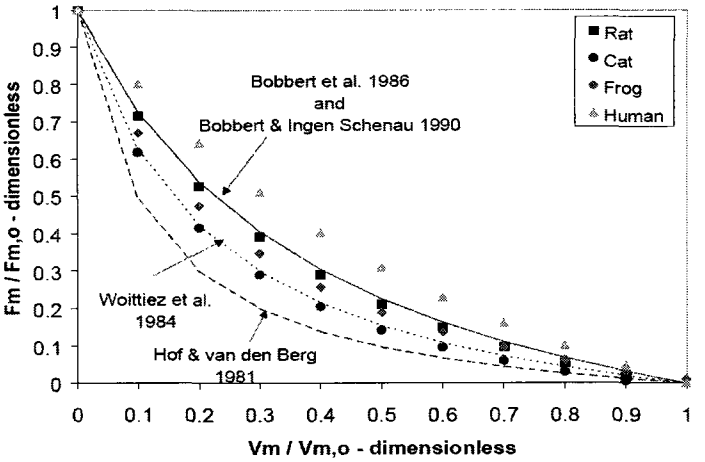

Figure 2-17: Predicted output force over a muscle's velocity range for four different animals and four published biomechanic models [6].

where F_m and V_m denote the muscle force and velocity, respectively. Klute et al. [6] has successfully duplicated the biological muscle viscous behaviour by designing a hydraulic damper with fixed orifices that is placed in parallel with the BPM. The mechanical configuration shown in Figure 2-18 results in BPM viscous behaviour.

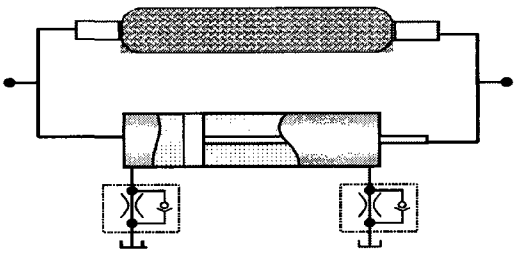

Figure 2-18: Hydraulic damper with flow control valves placed in parallel with the BPM [6].

2.4 BPM Controls

The number of published articles on BPM controls is far greater than any other category in the literature survey. For two reasons, firstly with the recent evolution of controls technology, researchers have sought to overcome previous pneumatic control issues. Secondly, since there

are no analytical BPM dynamic models, researchers have overcome this problem by adopting advanced controllers which do not require an accurate model.

For the BPM, control aspects include linear/non-linear control, adaptive control, optimal predictive control, and soft computing methods including fuzzy logic, Neural Network and hybrid structures of both. Given the large number and the wide range of controls technology, only a brief discussion can be given about the methods and the results obtained in the following selected papers.

In 1990, Osuka, Kimura and Ono [30] recognized that the dynamics of the actuator is not well defined and highly non-linear. They adopted the H^{∞} control theory which was originally developed by Zames in 1981 [31]. Using this theory, they derived a robust controller for operating a dual BPM system (*i.e.* autagomistic pair). This system consist of two BPM's that work together; while one muscle contracts, the other relaxes thus producing a rotating motion for the system pulley (Figure 2-19 (b)). The system movement is tracked based on the angular displacement of the pulley. The experimental result for the proposed controller (as the system is subjected to a step perturbation) is shown in Figure 2-19 (a). Osuka et al. did not provide any information about the system input or the BPM physical characteristics.

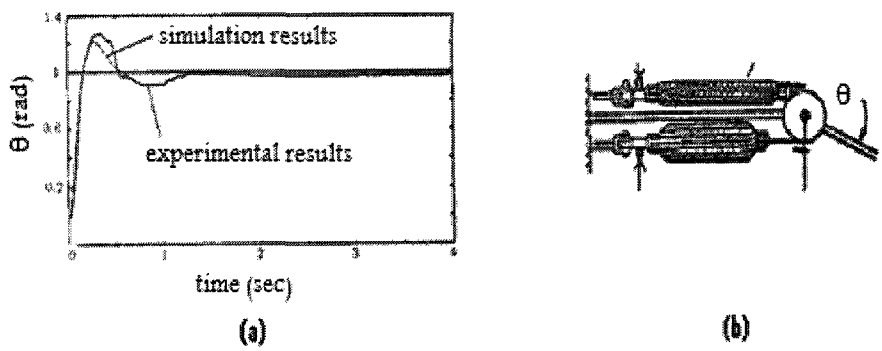

Figure 2-19: (a) Experimental and model simulation results (b) Autagomistic pair setup [30].

Nouri, Gauvert, Tondu and Lopez [32] are the first to apply adaptive control with a system reference model technique for a robot arm that uses the BPM for actuation. Their reference model is a second order system and the adaptive mechanism was chosen as a sliding regime for a dynamical variable structure. The implemented control law for their adaptive controller was the Generalized Variable Structure (GVS) law. Nouri et al. claimed that the developed algorithm

(GVS-MRAC) requires only an approximate identification of the system for effective implementation. The experimental validation of the proposed controller shows a good accuracy response when a step perturbation is introduced to the system (Figure 2-20).

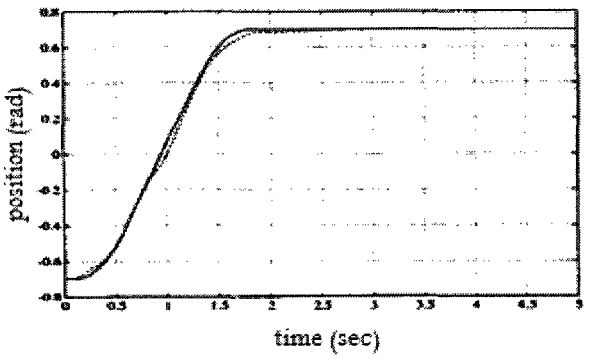

Figure 2-20: Validation results for a robot arm motion. Dash and solid curves represent the model and experimental results, respectively [32].

Nouri et al. did not provide any information about the physical characteristic of the robot or the step perturbation introduced to the system (Figure 2-20). Caldwell, Medrano-Cerda, and Goodwin [33] attempted to implement a discrete time Proportional Integral Derivative controller with a feed-forward term for a BPM powered system but are not successful. Caldwell et al. attributed this failure on the controller sensitivity to error in the feed-forward term. The feed-forward term could have been improved by a superior BPM model however the authors proceeded with model estimation using the Least Square algorithm and an adaptive control law. They estimated the parameters for a linear discrete model and used pole placement for controller design. In order to validate the new controller, the authors designed a lower section of an elbow joint that is composed of 5 BPMs. Caldwell et al. demonstrated good accuracy for the robot when it was subjected to the input shown in Figure 2-21.

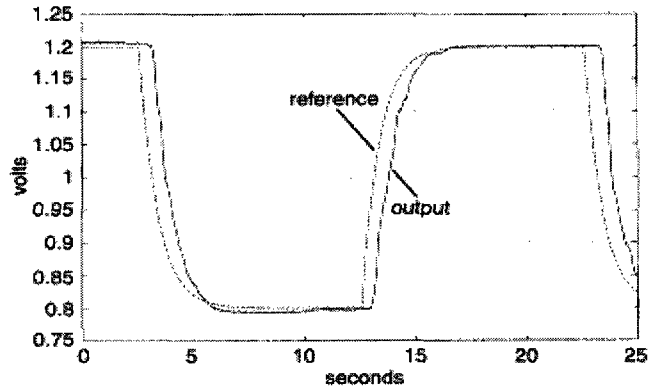

Figure 2-21: Results for a smoothed square wave reference input.

Caldwell et al. also stated that an accuracy of 1 degree (0.045 volts) at the elbow joint could be achieved for a constant set point. Very similar results were also published by Medrano-Cerda, Bowler and Caldwell [34] who used the adaptive pole-placement technique to develop a controller for a dual BPM system [33].

Cai and Yamaura [35] implemented a sliding mode controller to achieve accurate tracking control of a manipulator that is driven by BPM's. The full dynamic model for the manipulator was derived using a second order Euler-Lagrange equation for which the numerical values for its parameters are estimated. Cai and Yamaura ignored any system friction or disturbance. Cai and Yamaura did not present experimental validation for the proposed controller. They stated "some simulation results show that the presented control scheme has a good robust performance ..."[35].

Kimura, Hara, Fujita and Kagawa [36] proposed to use feedback linearization in order to adequately control the experimental apparatus shown in Figure 2-22. Feed-back linearization was implemented to eliminate the system non-linearities such that the authors could use the linear control design approach (pole placement technique). For feed-back linearization, an analytical model of the system is required; the authors adapted the model derived by [37] which is described as a third order non-linear system. Furthermore, by measuring the disturbance (assuming to be a step-type), Kimura et al. implemented feed-back linearization with disturbance rejection for better system accuracy. The steady state errors shown in Figure 2-23 are due to the presence of the system hysteresis. No quantitative accuracy was given for the new developed controller.

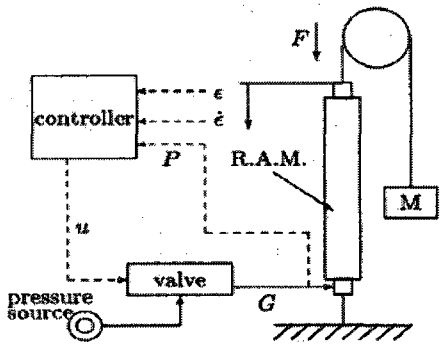

Figure 2-22: Schematic of experimental apparatus [36].

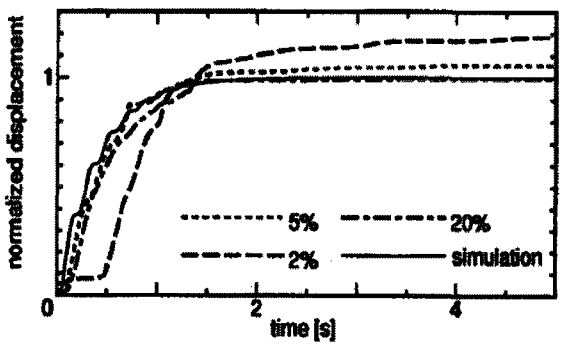

Figure 2-23: System response due a step perturbation of 2 %, 5 % and 20 % [36].

Soft computing is another approach that has been used to control BPM driven manipulators. Fuzzy systems, Neural Network and genetic algorithms are the most common approaches. They can model system uncertainties and vagueness for a low cost in computing resources. Carbonell, Jiang, and Repperger [38] analyzed a fuzzy back-stepping controller using three fuzzy sets. Two of the fuzzy sets modeled the inflation and relaxation mode of the BPM and the third mode represents the transient region. The fuzzy controller was used to describe uncertain system internal dynamics that are challenging to derive analytically. The authors concluded that their work offers a solution for the control of a BPM with different operational modes. Unfortunately, the authors did not include any experimental results that would have showed controller accuracy or performance. Previous work of Carbonell, Jiang, and Repperger [39] also covered the

implementation of three stable non-linear controllers for BPM's, namely: robust back-stepping, adaptive back-stepping and sliding mode.

Ozkan, Inoue, Negishi and Yamanaka [40] explored Neural Network technology to adequately control a Bridgestone hybrid robot that was driven by BPMs as shown in Figure 2-24.

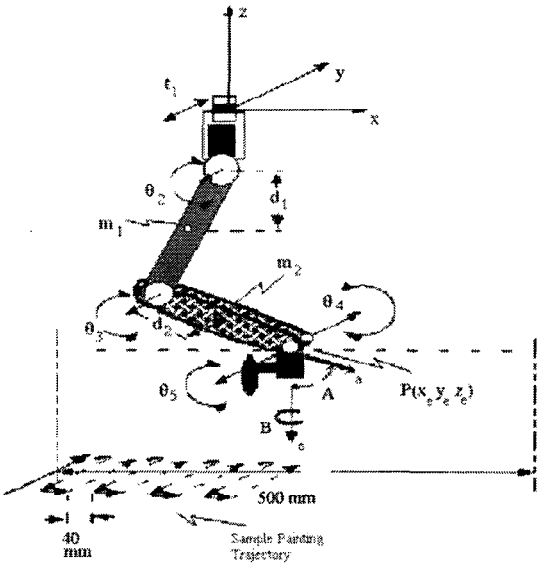

Figure 2-24: Five-degree of freedom Bridgestone painting robot arm [40].

Distinctively, Ozkan et al. developed a Neural Network topology that was based on the physical model of the robot. This model was derived by analyzing the Lagrangian Mechanics of the Bridgestone Robot Arm (Figure 2-24). The specific details of the system are used in the Neural Network to improve its efficiency and assure the network convergence to a generic solution in an optimum time. A similar approach was also adapted by Miyamoto, Kawato, Setonaya and Suzuki [41] for another Bridgestone robot-arm. The Neural Network controller by [40] was trained using a Back-propagation algorithm and the generalized delta rule (gradient descent). The controller performance was compared with a well tuned PID controller. It has been shown to have a superior accuracy when controlling the robot (Figure 2-25).

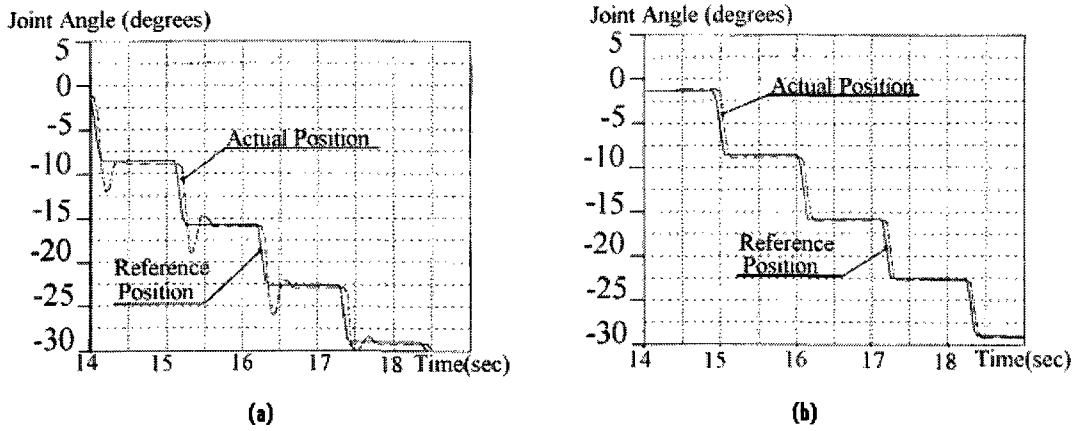

Figure 2-25: Robot trajectory validation results using (a) PID controller (b) NN controller [40].

A Proportional Integral Derivative (PID) controller is the most common controller in industry. It possesses a simple architecture, easy to tune, inexpensive and offers excellent performance for linear systems. However, this conventional controller does not perform too well for non-linear systems with parameter and structural inaccuracies. In order to use the PID controller architecture for these cases, various modified types of PID controllers, such as intelligent PID control, self-tuning discrete PID controller and self-tuning predictive PID controller [42] have been developed. In 2005, Thanh and Ahn [43] have also developed a new controller that is composed of a conventional PID controller and a neural network. More specifically, the PID controller has an adaptive control capability where its parameters are optimized by the Neural Network. In this paper the authors seek to control a dual BPM shown in Figure 2-26.

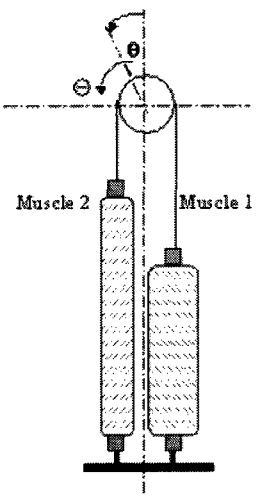

Figure 2-26: Dual BPM setup [43].

The newly developed nonlinear PID controller using a neural network by Thanh and Ahn has shown a capability to adequately control the position of the dual BPM system. Figure 2-27 shows the result of this controller with respect to a conventional PID controller.

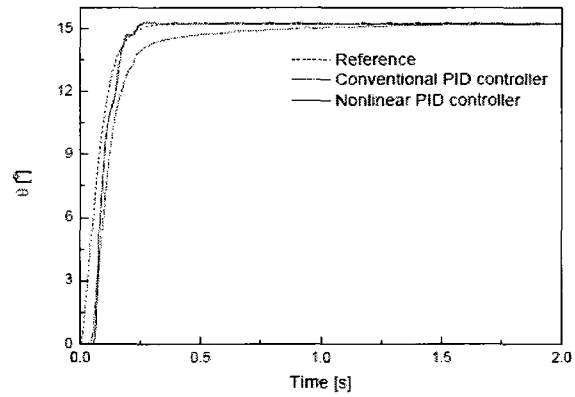

Figure 2-27: Trajectory validation for conventional PID controller and Non-linear controller [43].

Chapter 3

BPM Experimental Evaluation

Although there are a number of publications for the BPM as detailed in Chapter 2, there has been no comprehensive experimental evaluation achieved by any authors that would characterize the muscle behaviour. Thus, if such BPM characterization is missing, the BPM mechanical models cannot be optimally developed. In this chapter, a comprehensive experimental evaluation is presented for the BPM. This evaluation will identify the critical parameters to be considered in the mechanical modeling phase of the work and provide experimental results to confirm the models. Moreover, the development process for the BPM prototypes and the experimental setups are presented in this chapter. Finally, the BPM efficiency is experimental calculated for the developed muscle prototype.

3.1 Experimental Setup

To analyze the BPM characteristics, *three experimental setups* are designed and built. These setups are designed based on the three required types of muscle contraction tests, namely, the *muscle isometric contraction*, the *muscle eccentric contraction* and the *muscle concentric contraction*. These three contraction modes are identical to those identified for biological muscles. Each experimental setup operates (open loop) and controls (closed loop) BPM activities while monitoring and collecting key muscle properties. These properties are the muscle length, the muscle diameter, the braid angle, the muscle volume, the muscle force, the muscle pressure and the supply pressure.

An isometric contraction occurs when the muscle produces an increasing muscle force while maintaining a constant length. The BPM isometric contraction test was carried out by the experimental setup shown in Figure 3-1. Firstly, the BPM is restrained to a given length in the Instron tensile testing machine then it is inflated to a specific pressure. The muscle pressure and the muscle force are measured by a pressure transducer and by the Instron machine loading cell, respectively. These measurements are saved using a data acquisition system (*i.e.* LABVIEW) that is running on a PC.

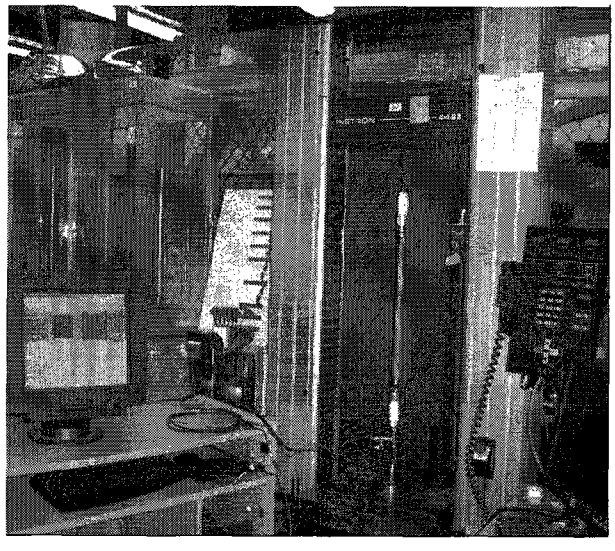

Figure 3-1: Experimental setup for the BPM isometric and eccentric contraction tests.

An eccentric contraction occurs when the pulling forces on the muscle are greater than the generated muscle force and the muscle elongates. This test was also carried out by the experimental setup shown in Figure 3-1. Firstly, the muscle is inflated to a specific contracted length and a specific muscle pressure. Subsequently, while maintaining a constant gas mass inside the muscle, the prototype is forced to elongate in the Instron tensile testing machine. The decrease of the muscle volume due to the elongation raises the muscle pressure. The muscle force and the muscle length are measured by the Instron machine load cell and displacement sensor, respectively. Moreover, the muscle pressure is measured by a pressure transducer and all measurements are saved using a data acquisition system.

A concentric contraction occurs when the generated muscle force exceeds the pulling forces and the muscle contracts. The BPM concentric contraction test was carried out by the experimental setup shown in Figure 3-2. In this case, the muscle is suspended vertically while being fixed at one end and attached to a mass on its other end. For the concentric contraction case, the muscle contraction was monitored using a rotary potentiometer mounted on the pulley as shown in Figure 3-2. In similar experimental setups, the muscle contraction was also monitored using a Linear Variable Displacement Transducers (LVDT) sensor.

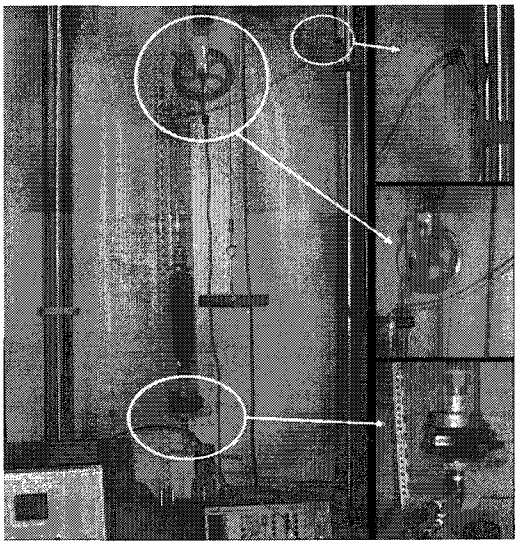

Figure 3-2: Experimental setup for the BPM concentric contraction test.

For the concentric contraction test, two proportionally controlled electro-mechanical valves are used to inflate and deflate the muscle. This also controls the muscle contraction length. Figure

3-2 shows the muscle is submerged in a water tank with a pressure transducer that measures the water height as a function of pressure. The water height is used to calculate the muscle volume. The muscle pressure is measured by a pressure transducer and the supply pressure is controlled using a pressure regulator and a capacitance tank. A schematic diagram for the BPM concentric test is shown in Figure 3-3.

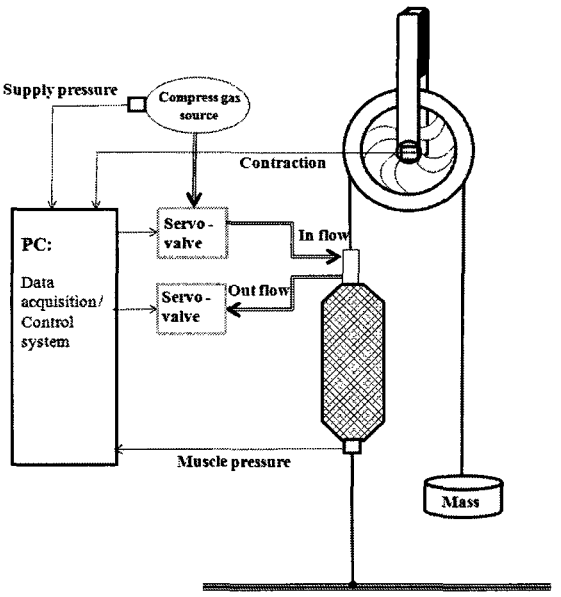

Figure 3-3: Schematic diagram for the BPM concentric test.

The system shown in Figure 3-3 is controlled by a software program using Laboratory Virtual Instrumentation Engineering Workbench (LabVIEW) that is running on a personal computer. Also, the same program acts as a data acquisition system for the muscle parameters. The sampling time for LabVIEW was 0.01 seconds.

3.2 Muscle Development

BPMs are currently manufactured and marketed by two companies, namely, Festo Corporation and Shadow Robot. Each company offers the BPM in different configurations and sizes. While the design and construction from the two companies are different, they share the same design concepts and have similar operating characteristics. Consequently, it was deemed important to

evaluate the key BPM operating characteristics and physical parameters that define the muscle's mechanical behaviour. The flexibility of varying the design parameters and muscle materials in the muscle prototypes are considered desirable features in this research program. Therefore, rather than purchase commercial BPMs, muscle prototypes are built for this study. In this process, 25 prototypes with different materials, size and configuration are built in the laboratory. An example is shown in Figure 3-4.

Figure 3-4: BPM prototype.

The muscle geometrical parameters are the number of fibre revolutions per muscle length n, the original braid diameter D_o, and the end fixture diameter d. The original braid diameter D_o and length L_o are measured when the braid angle θ is 20 degrees. This angle is approximately the braiding angle used when manufacturing the mesh. Due to the large number of BPM prototypes developed and tested, the designation code nx_Dxx_Exx is used for identification. With reference to Figure 3-5, the key to the code designation is as follows:

nx: x is the number of fibre revolutions per muscle length

Dxx: xx is the original braid diameter (cm)

Exx: xx is the end fixture diameter (cm)

Pxxx: xxx is the muscle pressure (kPa)

Lxxx: xxx is the contracted muscle length (cm)

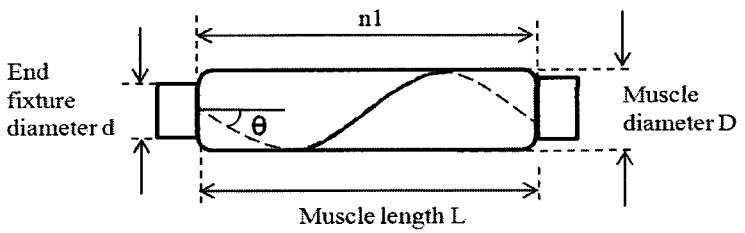

Figure 3-5: Salient muscle geometry parameters.

3.2.1 Muscle Materials

Prior to conducting the BPM experimental evaluation, the chosen BPM materials are independently tested. The aramid (Kevlar) and the polyethylene terephthalate (PET) are the main candidates for the braid material. The Kevlar braids are manufactured in the Composite Materials Laboratory at the University of Ottawa using an automated braiding machine for specific parameters, namely, the braid angle and the braid diameter. The PET braids are available from several manufacturers (*e.g.* TechFlex [44]). Experimental testing of both braids has shown that the PET is a superior candidate. The prototype that is made from the Kevlar braid experienced contraction stiction (un-continuous muscle contraction). The muscle resumed contracting only when a threshold of muscle pressure is reached for each step of the muscle contraction. Lubricating the Kevlar braids with dry Teflon did not solve the problem. On the other hand, the prototype made from the PET braid experienced smooth continuous contraction. This performance is attributed to the fibre shape of each braid. The PET fibre corresponds to a rigid round shape, so the fibre to fibre contact surface is limited, however, the aramid fibre is soft and flat, and thus the fibre to fibre contact surface is greater. A greater fibre to fibre contact surface increases the muscle friction and thus results in contraction stiction. In both cases, the braid properties offered sufficient surface coverage to prevent the bladder from bulging between the fibres. Further, the PET braid was available in different fibre colors; a feature that allows visual identification of the braid angle and the number of fibre revolutions per muscle length (Figure 3-6).

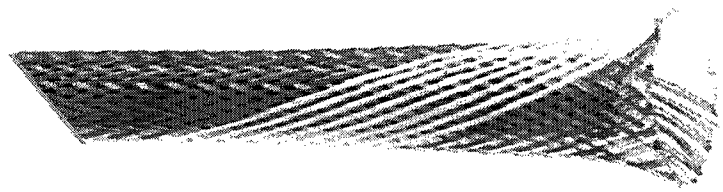

Figure 3-6: TechFlex PET braids [44].

The muscle bladder material main candidates are latex tubing, thick rubber tubing and butyl rubber (bicycle tire tubing). The latex and thick rubber tubing had high material stiffnesses, however, this required a high muscle pressure threshold (approximatively 150 kPa) for initial muscle inflation. This muscle pressure constraint reduces the BPM efficiency and limits the

feasibility of the BPM for many low pressure operating applications. In this work, the bladder acts as a gas seal and is not required to be rigid. Rigidity would be required only to prevent the bladder from bulging between openings in the braid. Larger openings would require more rigid bladder. A compromise between rigidity, size of openings, and amount of bulging can be struck. Experimental testing has shown that the bicycle tire tubes provide the required bladder rigidity without the considerable pressure threshold for initial inflation. The bicycle tube is available in different diameters that match the prototypes sizes. Based on these advantages, the bicycle tire tube was selected for the prototype development. For the muscle prototypes, brass couplings are selected to form the muscle ends and to provide the inlet and outlet orifices for the gas. The brass couplings are available in different sizes and forms. Mechanical straps are used to hold the bladder and the braided mesh on the fittings. The assembly of this muscle is simple and provides the flexibility of varying many muscle parameters for this research work. However, more robust structures should be designed for actual muscles.

Prior to conducting the experiments and collecting experimental data, the muscle length sensors are calibrated and validated using the n2_D1.9 prototype. The LVDT and the visual measurement (Getdata Graph Digitizer [45]) for muscle contraction distance conformed to each other at an accuracy of 0.3 % as shown in Figure 3-7. The visual measurement was particularly used to identify the muscle contour function to numerically calculate the surface area and the volume of the muscle.

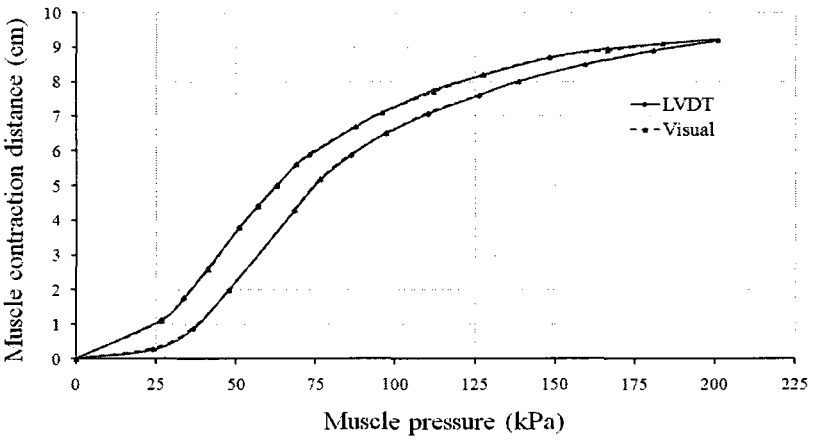

Figure 3-7: Comparison of the muscle contraction distance measurement taken by the LVDT and the digital imaging process (visual) for the n2_D1.9 prototype.

3.3 Experimental Evaluation

The BPM experimental evaluation is an important step for understanding the muscle behaviour and thus enabling optimum muscle modeling and design. This section covers a large number of static and dynamic tests for different muscle physical and operating parameters. Two muscle parameters are focused on, namely, the muscle contraction distance ΔL and the muscle force F. These parameters are studied for different muscle parameters, namely, the original braid length L_o, the original braid diameter D_o, the muscle end fixture size d, the muscle hanging mass M, the bladder original bladder diameter B, and the supply pressure P_s.

The effect of the muscle contraction velocity on BPM parameters was first discussed by Chou and Hannaford [16]. They claimed that damping or viscous friction is absent from the BPM. This was confirmed in this work by examining the n2_D1.9 prototype behaviour for two different contraction speeds. Figure 3-8 shows the muscle contraction distance as the muscle is inflated using two supply pressures of 138 kPa and 207 kPa. The higher supply pressure causes a greater air inflow to the muscle and thus leads to a faster muscle contraction. In this case, the muscle contracted at maximum speed of 3 cm/s and 1.92 cm/s for supply pressures of 207 kPa and 138 kPa, respectively.

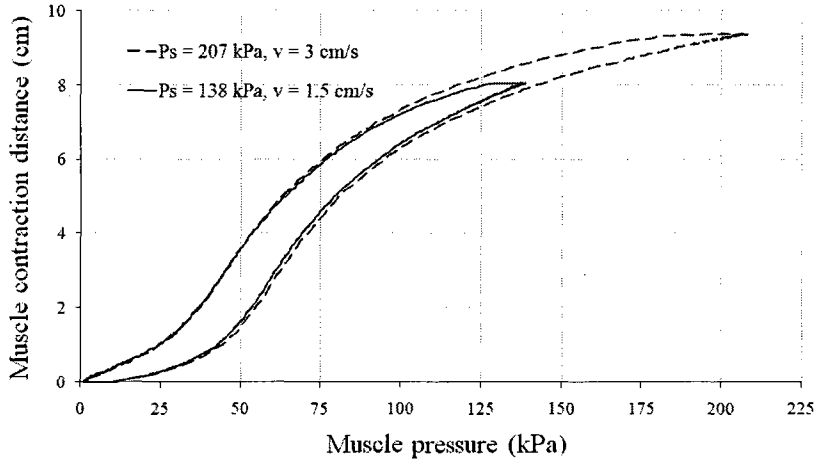

Figure 3-8: Muscle concentric contraction test results for the n2_D1.9 prototype for muscle supply pressures of 138 kPa and 207 kPa.

In Figure 3-8, the higher pressure curve (207 kPa) retraces the other curve up to approximately 120 kPa. This shows that the muscle contraction distance and the muscle hysteresis (the energy loss during a muscle contraction and relaxation cycle) are independent of the muscle contraction velocity. Thus, the remaining experimental testing and analysis focuses on quasi-static testing for two mechanical parameters, namely, the muscle force F and the muscle contraction distance ΔL. These two parameters are evaluated for different combination of muscle sizes and configurations (n = 1, 2, 3, 4 and 5; D_o = 0.9 and 1.9 cm; d = 2.5, 1.6 and 1.3 cm; and supply pressures P_s of 138 and 207 kPa).

3.3.1 Effect of Original Braid Length or n

Muscle contraction distance:

The original braid length L_o is evaluated when the braid angle θ is 20°. Figure 3-9 shows the muscle concentric contraction test results for three prototypes having different original braid lengths L_o of 17 cm (n1), 34 cm (n2) and 51 cm (n3) cm. The results show an increase in muscle contraction distance as the original braid length or n increases. However, the muscle contraction distance ratios for the original braid lengths of 17 cm (n1), 34 cm (n2) and 51 cm (n3) cm are 23.84 %, 27.7 % and 27.8 %, respectively. This ratio was calculated based on the maximum muscle contraction distance and the original braid length. This shows that this ratio is independent of the original braid length L_o or n. The discrepancy in results for the L_o of 17 cm (n1) is due to the muscle end distortion; this aspect is explained in Section 3.4.3.

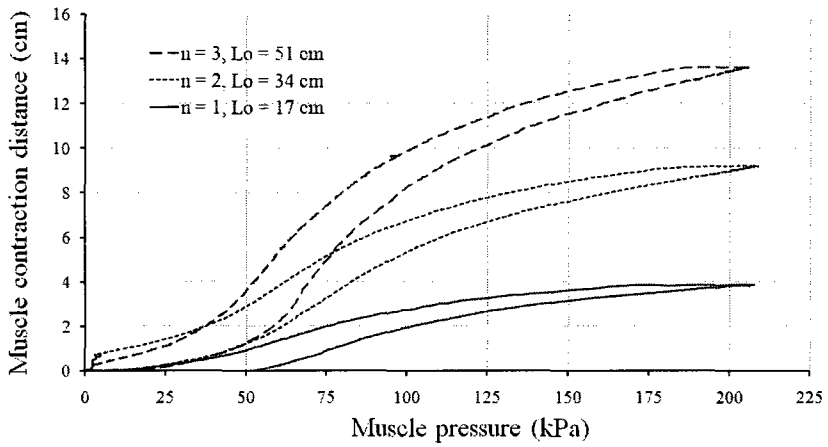

Figure 3-9: Muscle concentric contraction test results for the D1.9_E1.3 prototype for three muscle braid original lengths of 17 (n1), 34 (n2) and 51 (n3) cm.

Muscle force:

Figure 3-10 shows the muscle isometric contraction test results for three prototypes having different original braid length L_o of 17 (n1), 34 (n2) and 51 (n3) cm. All prototypes reached approximately similar maximum muscle forces of 590 N when the muscle pressure reached 207 kPa. For these tests, all prototypes had approximately the muscle diameter D of 2.4 cm. This result indicates that the muscle force is independent of original braid length L_o or n. The muscle force is rather a function of the muscle diameter D and the supply pressure P_s as discussed next.

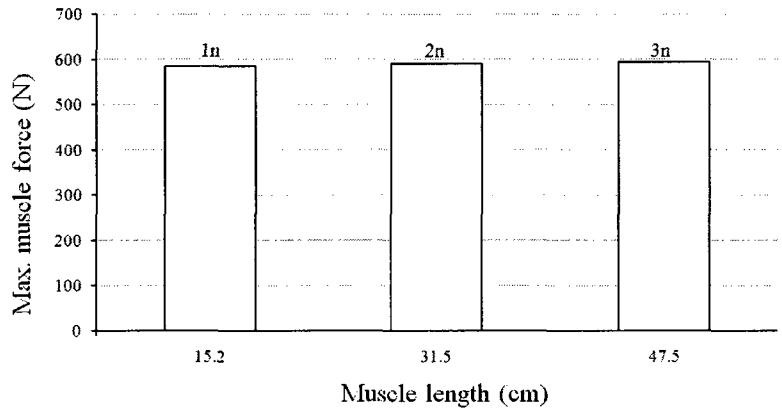

Figure 3-10: Maximum muscle forces for isometric contraction for the D1.9_E1.3 prototype for three original braid lengths of 17 (n1), 34 (n2) and 51 (n3) cm.

3.3.2 Effect of Original Braid Diameter

Muscle contraction distance:

The original braid diameter D_o is evaluated when the braid angle θ is 20°. This diameter is a function of the braid angle, fibre diameter, and the number of fibres. This parameter is first examined for the muscle contraction distance. Figure 3-11 shows a muscle concentric contraction test results for two original braid diameters of 0.9 cm and 1.9 cm.

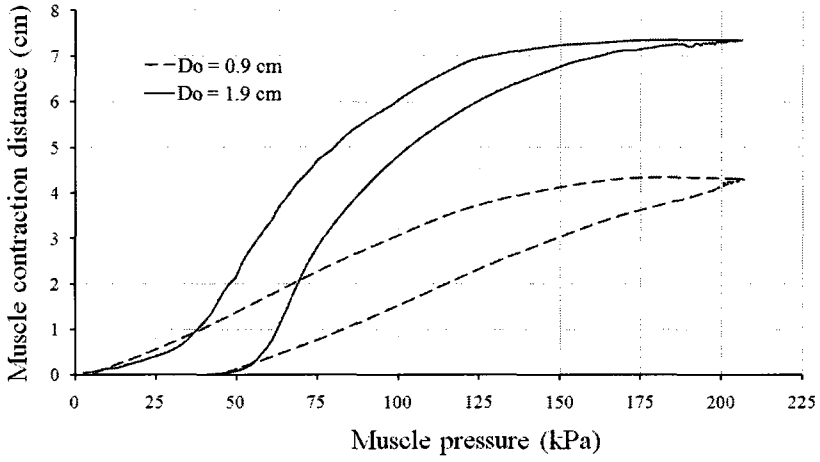

Figure 3-11: Muscle concentric contraction test results for the n2_E12.7 prototype for two original braid diameters of 0.9 cm and 1.9 cm.

Figure 3-11 shows that the muscle contraction distance ratio for the prototypes with original braid diameters of 1.9 cm and 0.9 cm are 29.1 % and 16.97 %, respectively. These results show significant differences between the contraction distance characteristics of the two muscles. This conclusion, however, is contradicted in Section 4.2. In this test, the initial braid angle for the two prototypes was different and thus one prototype had a greater contraction ratio than the other. The final braid angle for both muscle prototypes was approximately 48°. The difference in braid angle is attributed to the initial braid expansion by the bladder.

Muscle force:

In the previous section, the original braid length was shown to have negligible effect on muscle force; however, experimental results in Figure 3-12 show that the original braid diameter has considerably affected the muscle force capability. The prototype with an original braid diameter of 1.9 cm reached a muscle force that is approximately 6 times greater than the prototype having an original braid diameter of 0.9 cm (both prototypes are tested for an isometric muscle length of 31 cm).

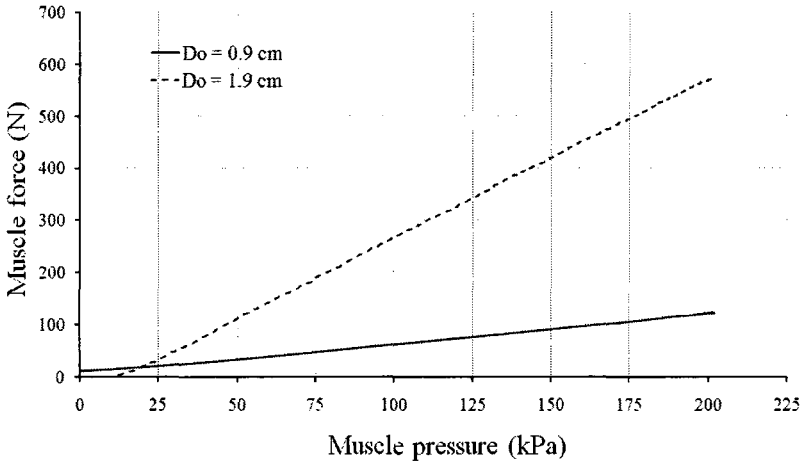

Figure 3-12: Muscle isometric contraction test results for the n2_D1.9 and 4.5n_D0.9 prototypes for a contracted muscle length of 31 cm.

3.3.3 Effect of Muscle End Diameter

Muscle contraction distance:

The muscle end diameter *d* reflects the end fixtures size to which the muscle braid and bladder are attached. Figure 3-13 shows concentric contraction test results for three end fixture diameters (1.3 cm, 1.6 cm and 2.5 cm) for otherwise identical BPM prototypes.

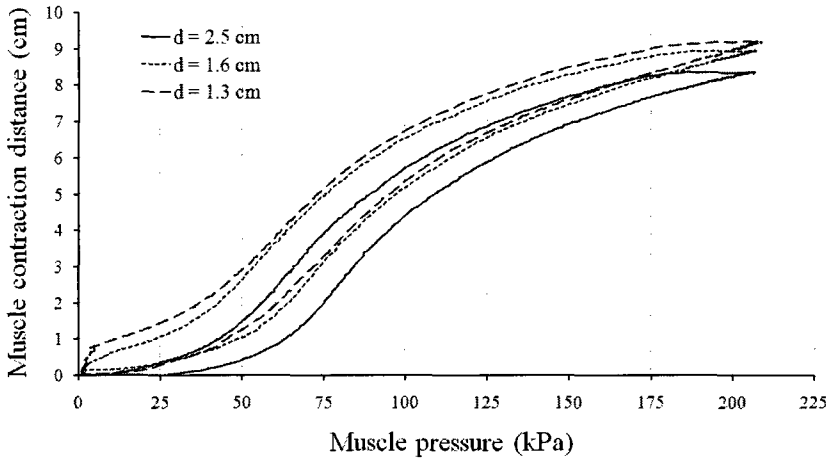

Figure 3-13: Muscle concentric contraction test results for the n2_D1.9 prototype for three different muscle end diameters 1.3 cm, 1.6 cm and 2.5 cm.

The experimental results in Figure 3-13 show increasing muscle contraction distances for decreasing muscle end diameters. This is due to the larger braid angle change that the muscle goes through for smaller end diameters. In the case of a larger muscle end diameter, the braid is initially expanded to fill the end fixtures such that the ends become a zone with no contraction abilities.

Muscle force:

Figure 3-14 and Figure 3-16 show isometric contraction test results for an isometric muscle length that model near full muscle relaxation and contraction states, respectively. Each figure shows the muscle force generated for two various end size fixture diameters (1.3 cm and 2.5 cm).

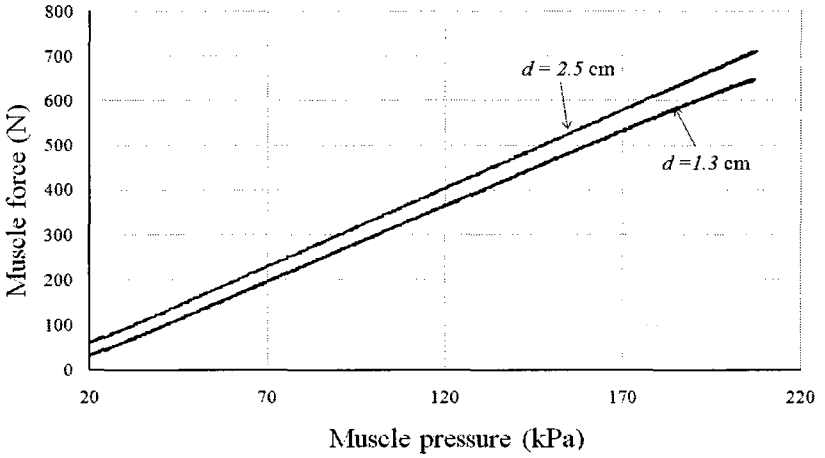

Figure 3-14: Muscle isometric contraction test results for the n3_D1.9 prototype for two different muscle end diameters (1.3 cm and 2.5 cm) at a muscle contracted length of 49 cm.

Figure 3-14 shows that the prototype having a larger muscle end diameter had a greater muscle force. As the muscle is inflated, the muscle average diameter increases while the muscle end diameters stay fixed. Thus for smaller end fixtures, a greater distortion will result at the muscle ends. This reduces the muscle force since the braid fibres are at an inclination angle, β (Figure 3-15). This phenomenon is analyzed further in Chapter 5.

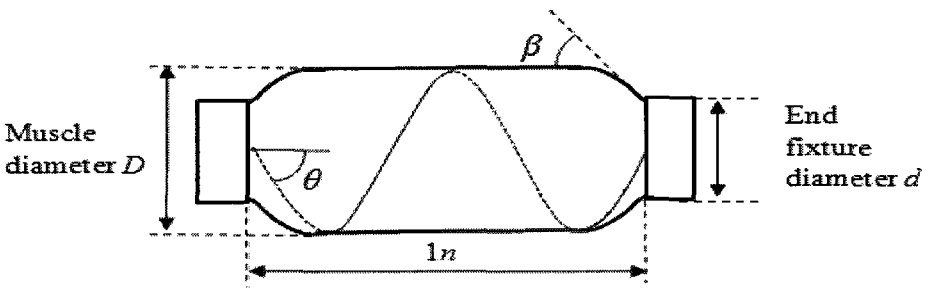

Figure 3-15: Illustration of the BPM prototype in a contracted state with muscle end inclination angle β.

Another factor that contributes to the results in Figure 3-14 is the muscle diameter D of both prototypes. While both tests are carried out at a similar muscle contracted length of 49 cm, the muscle prototype with larger end muscle diameter possess a slightly smaller muscle diameter at this length and thus contributes to a greater muscle force. To eliminate this second factor, Figure

3-16 show isometric contraction test results for the n2_D1.9 prototypes with two different muscle end diameters (1.3 cm and 2.5 cm) but tested at the same muscle diameter of 3.8 cm.

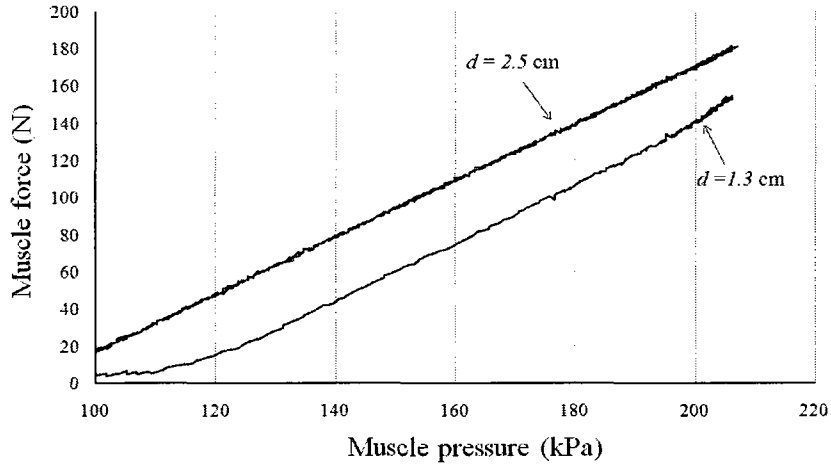

Figure 3-16: Muscle isometric contraction test results for the n2_D1.9 prototype for two muscle end diameters (1.3 cm and 2.5 cm) with muscle diameter of 3.8 cm.

The experimental results in Figure 3-13 and Figure 3-16 clearly show a change in the muscle behaviour with a change in the muscle end diameter.

3.3.4 Effect of Static Mass

Muscle contraction distance:

The static mass corresponds to the load that the muscle is pulling during a concentric contraction test. This test can be also described as a muscle isotonic contraction if this load is considered equivalent to the muscle force. To demonstrate the effect of the static mass on muscle behaviour, the n2_D1.9_P138 prototype was tested for three different static mass, 2.3 kg, 4.6 kg and 9.1 kg (Figure 3-17). The same experiment was repeated and the results shown in Figure 3-18 but for a higher supply pressure of 207 kPa.

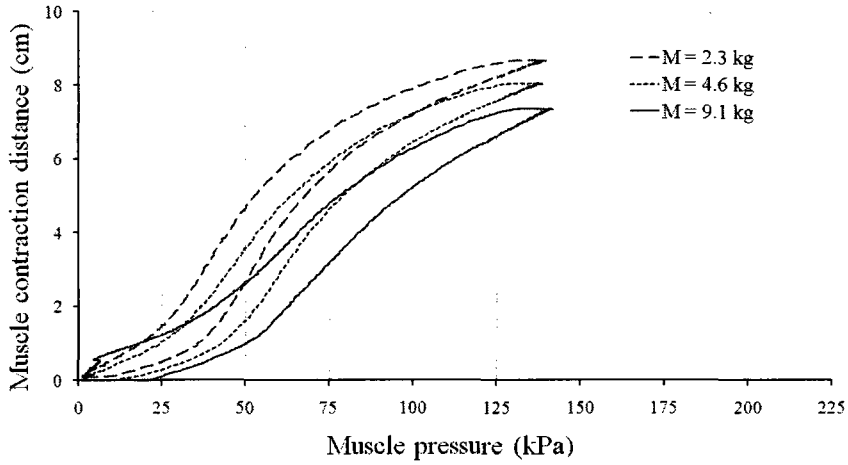

Figure 3-17: Muscle concentric contraction test results for the n2_D1.9_P138 prototype for three static masses of 2.3 kg, 4.6 kg and 9.1 kg.

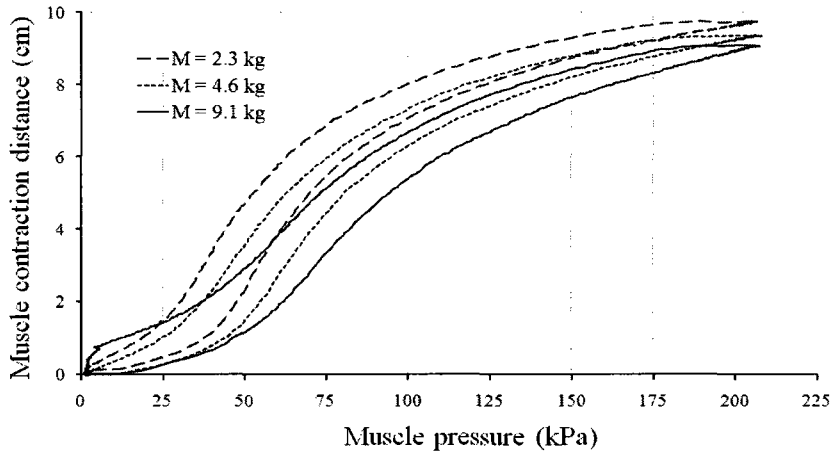

Figure 3-18: Muscle concentric contraction test results for the n2_D1.9_P207 prototype for three static masses of 2.3 kg, 4.6 kg and 9.1 kg.

In Figure 3-17 and Figure 3-18, the muscle prototype starts contracting at different muscle lengths. This is attributed to the mass which stretches the muscle more with a larger static load. However, in Figure 3-17 and Figure 3-18, the curves have been shifted vertically to the origin such that the results can be compared (Figure 3-19 shows the unmodified results for n2_D1.9_P138). These results could be interpreted differently if the muscle length elongation caused by the static mass is not considered part of the muscle contraction distance range.

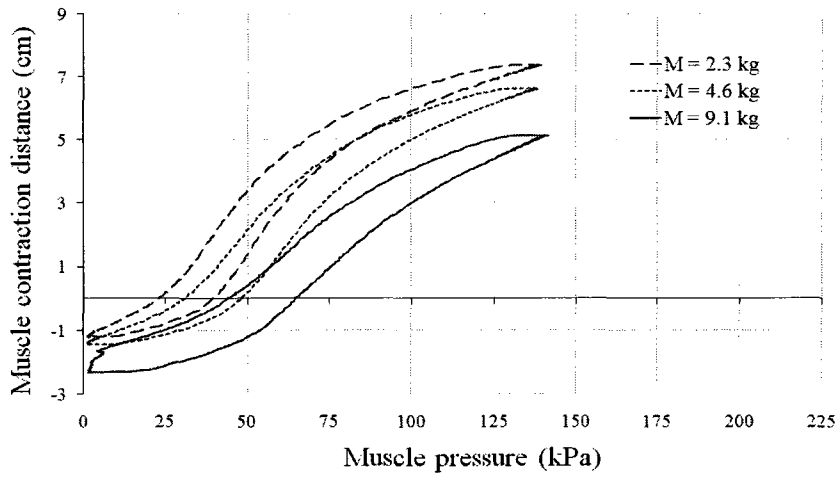

Figure 3-19: Original muscle concentric contraction test results for the n2_D1.9_P138 prototype for three static masses of 2.3 kg, 4.6 kg and 9.1 kg.

The results in Figure 3-17, Figure 3-18 and Figure 3-19 show that by increasing the static mass and keeping all other muscle parameters constant, the muscle contraction distance ratio tends to be reduced. For a supply pressure of 207 kPa, the prototypes that are supporting a static mass of 2.3 Kg and 4.6 Kg achieved muscle contraction distance ratios of 30.9 % and 29.1 %, respectively. Thus, in the presence of a large supply pressure (*e.g.* 207 kPa); the muscle tends to reach similar contraction ratios.

3.3.5 Effect of Bladder Original Diameter

Muscle contraction distance:

The original bladder diameter D_b is taken to be the bicycle tube diameter that was used for the prototype. The original bladder length and diameter are selected to match the original braid length and diameter, respectively. This design criterion is adopted such that the bladder does not become a passive elastic element if the muscle is stretched. The passive elastic element could be useful for particular applications but such a design option is not considered in this work. To analyze the effect of the original bladder diameter, two identical prototypes are tested using two

original bladder diameters, 1.4 cm and 2.0 cm. Both bladders have identical material and thickness.

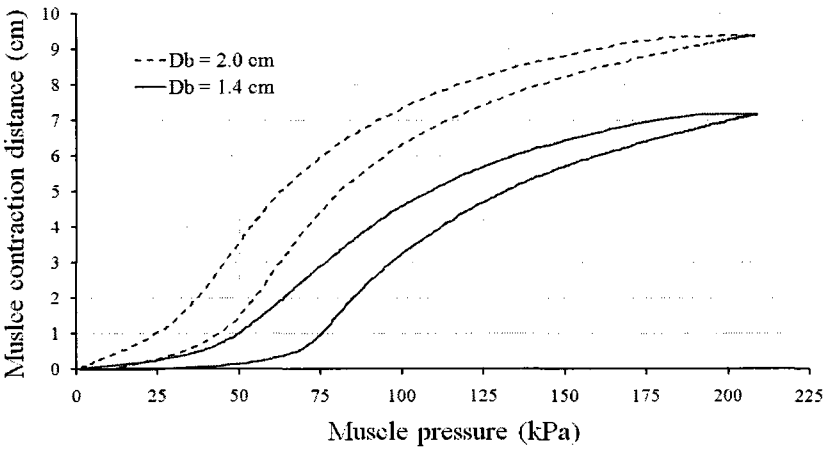

Figure 3-20: Muscle concentric contraction test results for the n2_D14.5 prototype for two original bladder diameters of 1.4 cm and 2.0 cm.

Figure 3-20 shows a change in muscle contraction distance when the bladder original diameter is changed from 1.4 cm to 2.0 cm. This is attributed to the bladder mechanical material properties. On a stress-strain curve, the curve increases linearly within the muscle circumference expansion range. A reduction in the bladder original diameter results in an increase in the elastic energy stored in the bladder material and an increase in the system hysteresis (Figure 3-20). The maximum bladder original diameter size is limited to the original braid diameter otherwise the bladder is initially deformed and this can lead to a disproportional inflation of the bladder and the muscle.

Muscle force:

The muscle force increases as the bladder original diameter is increased. This is because with larger bladder original diameter, less energy is consumed in expanding the bladder and hence more energy is used to produce additional muscle force.

3.3.6 Effect of Supply Pressure

Muscle contraction distance:

The supply pressure P_s is the pressure of the gas that is introduced into the system. During testing, the supply pressure is always maintained at a constant value by a pressure regulator. To explore the effect of the supply pressure, concentric contraction tests are done for the n2_D1.9 prototype for two supply pressures of 138 kPa and 207 kPa. As shown in Figure 3-21, the muscle pressure increases and becomes equal to the supply pressure when no further contraction occurs.

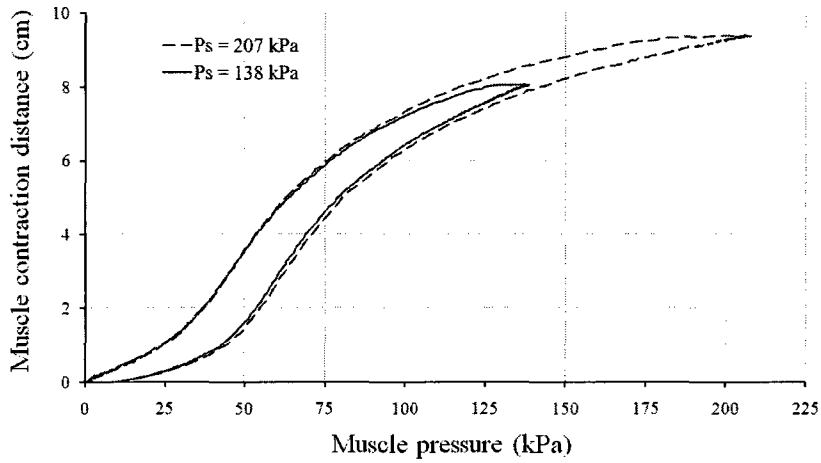

Figure 3-21: Muscle concentric contraction test results for the n2_D1.9 prototype for two gas supply pressures of 138 kPa and 207 kPa.

Figure 3-21 shows that the muscle reaches a higher contraction distance as the supply pressure increases. However, the experimental trend shows that the muscle contraction distance converges to a maximum point for increasing values of the muscle pressure. The experimental results show that increasing the supply pressure had little effect on the system hysteresis (up to 138 kPa). This phenomenon can be explained by the absence of damping in the muscle system.

Muscle force:

In all previous isometric contraction tests, the muscle force was shown to be proportional to the muscle pressure. Therefore, if the muscle supply pressure increases, the muscle pressure will increase accordingly and so does the muscle force. The muscle force and muscle pressure relationship are derived in Chapter 5.

3.4 Muscle Contraction Distance

The muscle's longitudinal motion is a key factor in muscle evaluation. It is important to analyze the muscle contraction distance with respect to different muscle configurations and muscle operating modes. Numerous muscle prototypes are developed and tested in a concentric contraction mode. Appendix A, Table A-1 and Table A-2 present over 70 experimental tests results for muscle contraction distance ratio with respect to six different parameters, namely, the fibre number of revolutions per braid, original braid diameter, muscle end diameter, supply pressure, static mass and bladder original diameter. The experimental results show that these parameters affect the muscle contraction distance ratio. The maximum muscle contraction distance was achieved by the n2_D1.9_E1.3_P207_M2.3 prototype. This corresponds to a muscle contraction distance ratio of 30.9 %. The average muscle contractions distance ratio for an original braid diameter of 1.9 cm and 0.9 cm are approximately 28 % and 16 %, respectively. Exceptions occurred when a prototype's end fixture diameter was different as was explained in Section 3.4.3.

The braid angle is a key parameter that affects the BPM contraction distance. The muscle contraction distance occurs over a specific braid angle range. This range is limited by the jamming state of the fibres at one end and by the muscle force equilibrium state at the other end. Experimentally, this braid angle range was determined to be 15 degrees to 48 degrees. In order to maximize the muscle contraction distance, the braid angle range must be extended. This could be achieved by manufacturing braids that possess a jamming state less than 15 degrees. This is achieved by reducing the number of fibres in the braid but without hampering the muscle structural strength or requires an increase in bladder rigidity to counteract bulging. The braid

angle range may also be enlarged if an efficient muscle prototype is produced such that it reaches a braid angle beyond the 48 degrees. An efficient muscle prototype transforms a higher ratio of input energy into output energy.

3.5 BPM Loss of Energy

Based on the literature survey, the source of loss of energy within the BPM system is not well understood. Many researchers have assumed that the loss of energy is solely from the coulomb friction between the braid fibres. However, the damped shape of the muscle transient response in the experimental testing results raises questions about the absence of any damping in the system. In order to shed the light on this issue, the prototype n2_D1.9 was lubricated using motor oil (5w30) and tested in a concentric contraction mode.

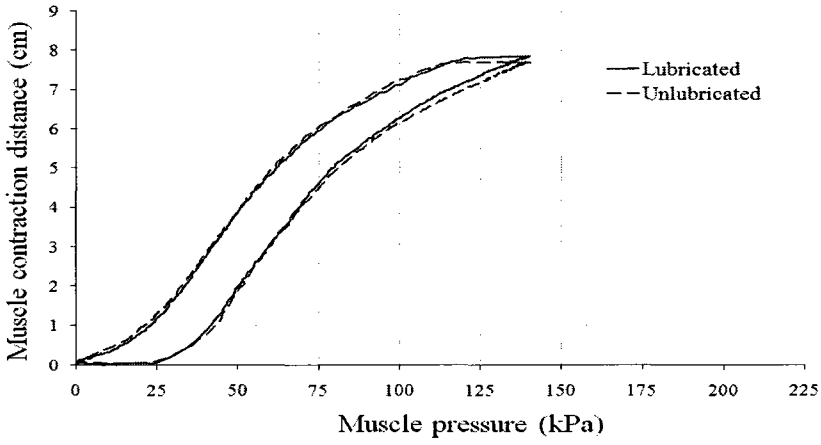

Figure 3-22: Muscle concentric contraction test results for the n2_D1.9 prototype (lubricated and unlubricated).

Figure 3-22 shows that lubrication has slightly reduced the muscle hysteresis and allowed limited increase in muscle contraction distance. A greater reduction in hysteresis was expected especially that the lubrication was applied at the main source of friction that is the fibre-fibre contact. It was observed that the braid fibres and the bladder are locked together through most of the contraction phase. This eliminates any loss of energy between the braid fibres and the muscle

bladder. Therefore, if static coulomb friction only exists between the braid fibres as it is claimed, the muscle response should oscillate but this is not the case. The answer to this can be found by analyzing the fibre to fibre contact surface as the muscle contracts. The first common mistake is to assume that the fibre to fibre contact surface is flat and constant and the second mistake is to assume that the fibre material's friction coefficient is valid for this case. As the muscle contracts, the braid fibre to fibre contact surface increases and so does the friction coefficient mainly due to fibre to fibre entanglement. This yields a greater friction force as the muscle contracts. This phenomenon would produce damped muscle behaviour as the muscle contracts. It is also important to note that while the muscle frictional force increases as the muscle contracts, the generated muscle force decreases to zero at the maximum muscle contraction distance. This confirms that the fibre to fibre friction is the main source of loss energy for the muscle; however its magnitude varies as the muscle contracts. This analysis is expressed in Chapter 5.

3.6 Muscle Passive Properties

In this section, the muscle passive properties are analyzed by achieving muscle eccentric contraction tests. Figure 3-23, Figure 3-24 and Figure 3-25 show the muscle experimental results when the muscle is initially inflated and then elongated by the Instron machine. The initial n2_D1.9 prototype length was 26.5 cm and the muscle pressure was 96 kPa.

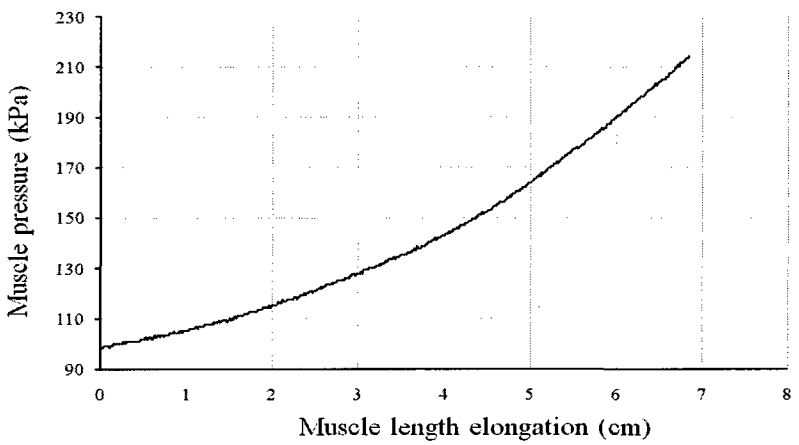

Figure 3-23: Muscle eccentric contraction test results for the n2_D1.9 prototype.

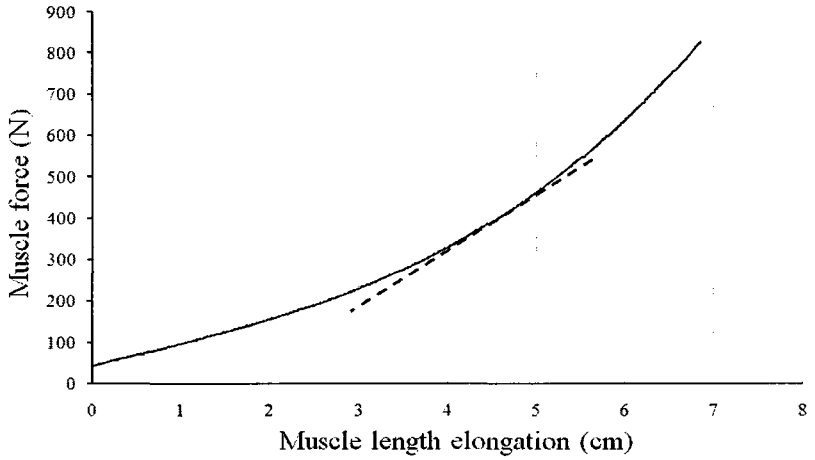

Figure 3-24: Muscle eccentric contraction test results for the n2_D1.9 prototype.

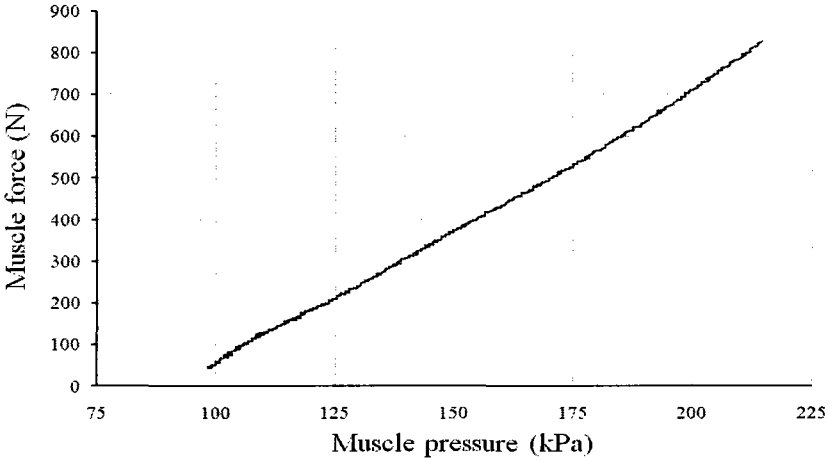

Figure 3-25: Muscle eccentric contraction test results for the n2_D1.9 prototype.

As the prototype is elongated in the previous test, this decreased the muscle volume, raised the muscle pressure and created a muscle force. Figure 3-25 shows a linear relationship between the muscle force and the muscle pressure. This was also confirmed by the isometric contraction test earlier on (Figure 3-12). Using Figure 3-23, a linear estimation of the BPM stiffness K is determined to vary between 5 kN/m and 26 kN/m. This confirms an earlier statement that the BPM behaves like a variable stiffness spring. Figure 3-24 shows that the muscle pressure and the muscle length relationship is not linear.

The next set of experiments examines the muscle force as a function of the muscle pressure. This was achieved by testing the n3_D1.9 prototypes in an isometric contraction mode at seven muscle contracted lengths between 39 cm to 49 cm (Figure 3-26). The muscle lengths of 39 cm and 49 cm represent near full muscle contraction and extension states, respectively.

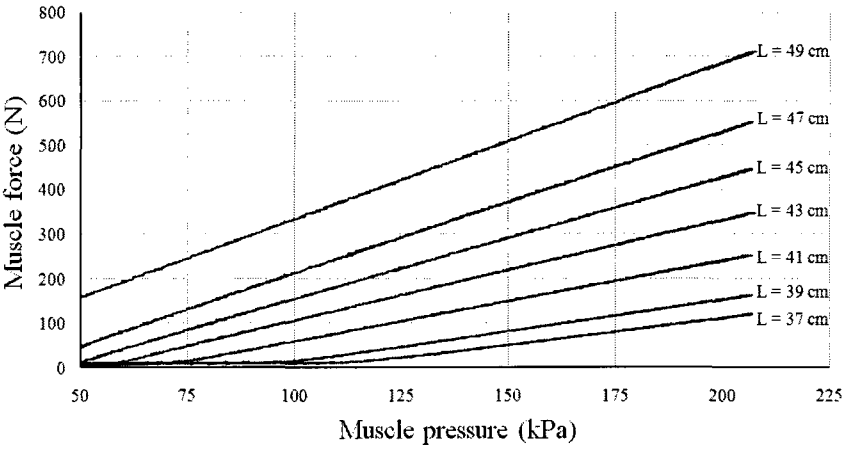

Figure 3-26: Muscle isometric contraction test results for the n3_D1.9 prototype for different muscle contracted length.

Figure 3-26 results reconfirm the linear relationship between the muscle force and the muscle pressure. A greater muscle force occurred when the BPM was tested at a longer contracted length. Further, the muscle force went to zero as the muscle contracts to its minimum length. This characteristic is also true for a biological muscle.

3.7 Muscle Damping Ratio

The damping ratio ζ is a measure of the system actual damping with respect to the critical damping case. To determine this ratio, the muscle is subjected to an input perturbation and the output response of the muscle is measured. This was accomplished by suspending an inflated muscle vertically and then manually pulling the muscle vertically downward by a cord and instantly releasing the cord after achieving an approximately 1 cm of muscle elongation. The

muscle has a constant air mass during the perturbation. In this case, the muscle pressure and the muscle contraction distance are recorded using a pressure transducer and an LVDT.

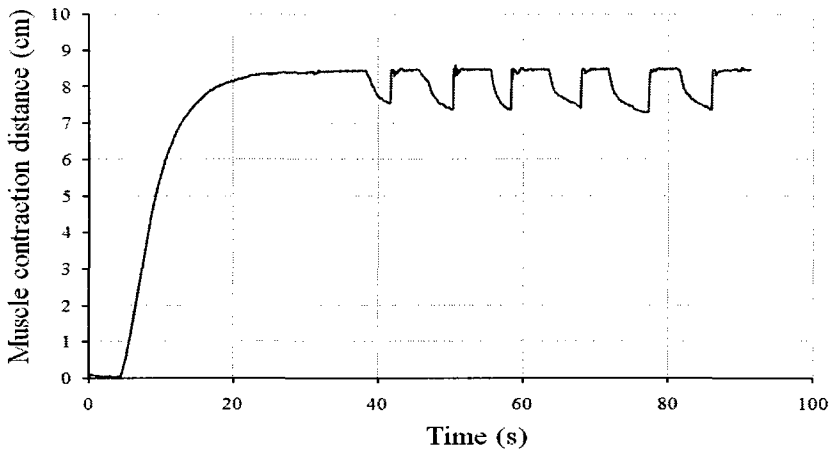

Figure 3-27: Muscle damping ratio test results for the n2_D1.9 prototype.

Figure 3-27 shows the muscle being inflated to a muscle contraction distance of approximately 8 cm and then while maintaining a constant muscle air mass at this position, the system is subjected to six perturbations. The amplitude of these perturbations is approximately 1 cm in muscle elongation. The results in Figure 3-27 confirms that very limited system oscillation exist after each perturbation. This reaffirmed the original belief that the system is highly damped. The same prototype was further tested at different muscle contracted lengths. The muscle oscillation diminishes to zero as the muscle contraction distance decreases. This is attributed to the low muscle stiffness when the muscle is extended. Given the limited amplitude of the oscillation, it is hard to determine an accurate value for the damping ratio. However, the results confirm that the BPM is a damped system and its damping ratio does vary as a function of the muscle length.

3.8 BPM Efficiency

The muscle efficiency is an indication of the muscle's ability to transfer the input energy to output energy. This ratio may vary drastically depending on what is considered as an input

energy and an output energy. In order to determine and analyze the system efficiency, an experimental setup was used. The muscle was hanged with a static mass on the lower end. Starting from a deflated state, the muscle was inflated by a measured pressurized tank volume. The data acquisition system monitored the tank pressure, the muscle pressure and the muscle length till the tank and the muscle system reached a steady state. The muscle input energy, the muscle conserved energy, the muscle potential energy and the muscle loss energy are shown in Appendix A, Table A-3 for a range of static masses and tank pressures. The muscle input energy is that transferred from the tank to the system, the muscle conserved energy is that contained in the pressurized air inside the muscle volume, the potential energy is the static mass potential energy, measured from the steady state position, and the lost energy is the balance. Table A-4 shows two muscle efficiencies, η_1 and η_2 that are calculated as follows:

$$\eta_1 = \frac{Potential\ energy + Conserved\ energy}{Input\ energy} \tag{3-1}$$

$$\eta_2 = \frac{Potential\ energy}{Input\ energy} \tag{3-2}$$

where η_2 considers the conserved energy as a loss energy rather than an output energy as in η_1. In an isometric contraction case, the energy conserved by the muscle pressure is never lost and helps regain the muscle state after the contraction. The results in Table A-4 show that the muscle efficiency increases proportionally with initial tank pressure and static mass. As the initial tank pressure increases, the muscle contracts further and thus reaches an optimum surface area where its efficiency is at its highest. Also, since the output energy is defined as a function of the potential energy, the BPM efficiency increases as the static mass increases. The optimum muscle η_1 obtained is 84.34 % for the n2_D1.9_P207_M9.1 prototype while the optimum muscle η_2 obtained is 10.2 % for the n2_D1.9_P138_M9.1 prototype. The lost energy varied between 15 - 40 % for the tested prototypes. Figure 3-28 shows the energy values for the n2_D1.9_P138 prototype as it contracts until it reached an equilibrium pressure between the muscle system and the tank pressure.

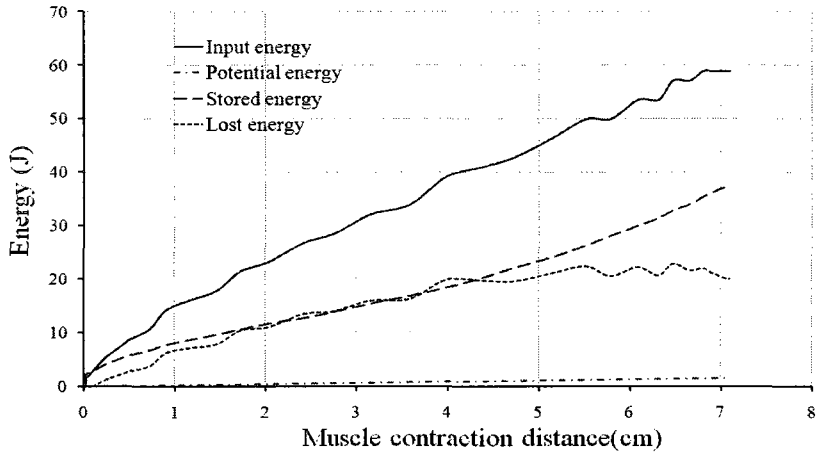

Figure 3-28: Muscle efficiency test results for n2_D1.9_P138 prototype.

Chapter 4

BPM GEOMETRICAL MODELING

The BPM experimental evaluation results provide a good understanding of the muscle behaviour, however, for design purposes, the interrelationships between the geometry and functional parameters are required. It was noted during the experimental work that the muscle ends experience distortion as the muscle contracts. This effect is generally ignored in popular muscle models. These models assume a purely cylindrical muscle. More realistic muscle geometry is used in this work. Based on this new muscle geometry, analytical models are developed to identify the muscle length, its surface area, its volume and the braid jamming states. Moreover, tests are conducted to aid in analyzing the BPM geometrical properties, and the data generated are later used to validate the proposed analytical models. The experimental results in this chapter show that the proposed geometrical model reduces the Normalized Root Mean Square error of for the muscle length from 3.5 % to 1.5 % which is produced by the prevalent geometrical model adopted by most researchers.

4.1 BPM Geometrical Model

The BPM is composed of an elastic bladder, a braided mesh and two end fixtures. The braid wraps around the bladder and both are attached to end fixtures by mechanical straps. In a deflated state, the muscle braid takes approximately a cylindrical form. However, as the muscle inflates, the average muscle diameter increases substantially beyond the end fixture diameter and thus creating an irregular shape for the muscle ends sections (Figure 4-1).

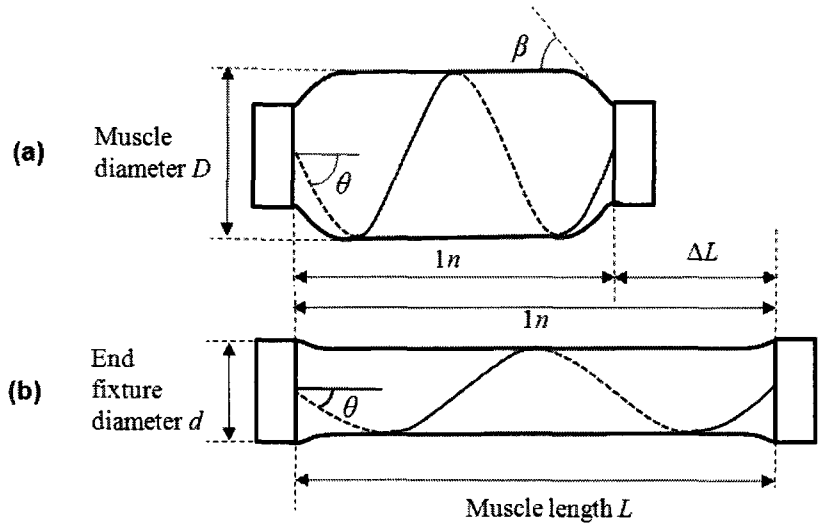

Figure 4-1: BPM prototype: (a) pressurized state (b) deflated state.

To model the muscle's true form, a more realistic muscle geometry shown in Figure 4-2 is used in this work. The proposed geometry is composed of three shape elements; a partial cone that models each muscle end and a cylinder to model the muscle middle section.

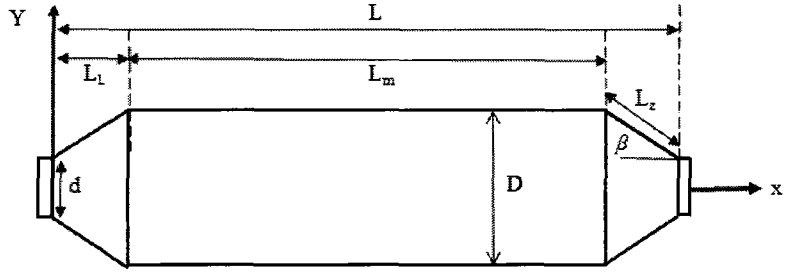

Figure 4-2: The Muscle's structure for geometrical modeling.

With reference to Figure 4-2, L is the overall muscle length, L_m is the muscle middle section length, L_L is the horizontal length of the cone, L_z is the cone generator length, and β is the cone angle of the muscle ends. Among these parameters, only L_z is assumed to be invariant with muscle contraction, and is determined experimentally. All other parameters are a function of the muscle contracted length.

As was previously indicated, the BPM consists of an elastic bladder that is enclosed by a braided mesh. The muscle middle section geometry is governed primarily by the deformation of the braid and its relationship is based on a helix form shown in Figure 4-3.

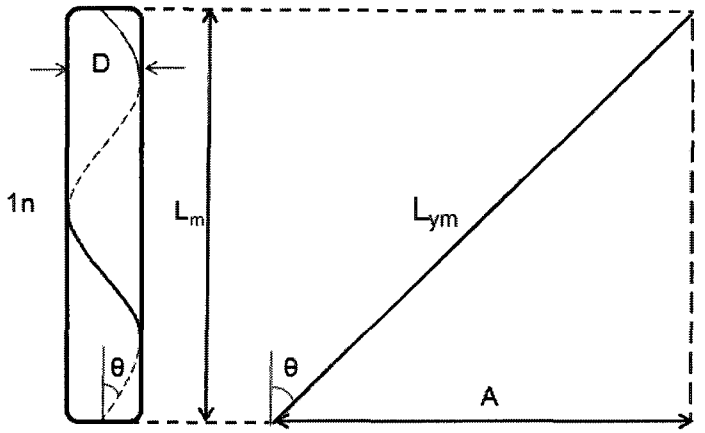

Figure 4-3: Geometrical properties for the braided mesh that reflects the muscle middle section.

With reference to Figure 4-3, θ is the braid angle, L_{ym} is the uncoiled fiber length and n is the number of fiber revolutions over the length L_m. The relationships between the muscle diameter D and the muscle middle section length L_m are given by:

$$D = \frac{L_{ym} sin\theta}{\pi n} \tag{4-1}$$

$$L_m = L_{ym} \cos\theta \tag{4-2}$$

Using Equations (4-1) and (4-2), the braid angle is eliminated and the braid diameter is given by:

$$D = \frac{\sqrt{L_{ym}^2 - L_m^2}}{\pi n} \tag{4-3}$$

The muscle end geometry is modeled as a frustum of a cone as shown in Figure 4-2. The cone base diameter expands beyond the end fixture diameter as the muscle contracts.

The cone horizontal length L_L is derived as follows:

$$L_L = \sqrt{L_z^2 - \left(\frac{D}{2} - \frac{d}{2}\right)^2} \tag{4-4}$$

The total muscle length is hence given by:

$$L = L_m + 2 * L_L \tag{4-5}$$

4.2 Braid Jamming State

Two braid jamming states may occur; a stretched state where the braid cannot elongate any further and a compressed state where the braid cannot contract beyond. The braid jamming states are characterized by parallel fibers in close contact with each other, thus preventing further mesh movement. The muscle contracted length range starts from the stretched braid jamming state to the length where the muscle forces reach an equilibrium state. Muscle concentric contraction is impossible to achieve beyond this point. Davis and Caldwell [46] derived an expression for the stretched muscle jamming state. Their relationship depends on experimental measurements of the trapezoid formed by the braid fibers. This makes the proposed solution impractical for design purposes as it is specific muscle dependent. Ko et al. [47] assumed that for a jamming state, there are no gaps between the braid fibers. Therefore, the braid geometry is solely formed by the two groups of fibers that interlace with each other based on the braid angle. The braid circumference at jamming state is formed by the effective fiber diameter d_f' of one of the interlacing fiber groups as shown in Figure 4-4.

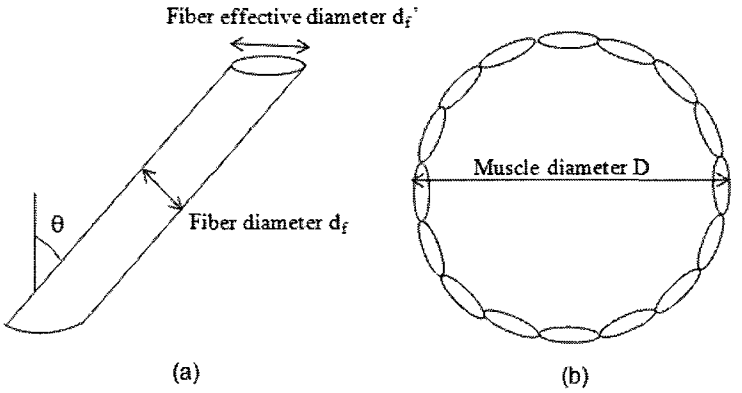

Figure 4-4: Illustration of (a) fibre diameter d_f and fibre effective diameter d_f' (b) muscle diameter D formed by the fibre effective diameter [47].

For the stretched braid jamming state, the muscle circumference C_j is given by:

$$C_j = \frac{Nd'}{2} \tag{4-6}$$

or

$$C_j = \frac{Nd}{2\cos\theta_{js}} \tag{4-7}$$

where N is the number of fibers and θ_{js} is the braid angle when the mesh is at maximum length. The mesh diameter at this state represents the minimum diameter D_{min} that the mesh could physically reach and is given by:

$$D_{min} = \frac{Nd}{2\pi\cos\theta_{js}} \tag{4-8}$$

For this jamming condition or when the braid angle $\theta = \theta_{js}$, the mesh reaches its maximum length L_{max}:

$$L_{max} = L_y \cos\theta_{js} \tag{4-9}$$

where L_y is the uncoiled fiber length for the muscle braid. Using Equation (4-1) to determine the braid circumference and then comparing it to Equation (4-7) results in the condition for the braid jamming state as follows:

$$\sin\theta_{js}\cos\theta_{js} = \frac{Nd}{2L_{yn}} \tag{4-10}$$

where L_{yn} is the fiber length per unit n. The solution for this relationship generates two angles. A stretched jamming state angle θ_{js} and a compressed jamming state angle at θ_{jc}.

The braid diameter and length at this jamming angle represents the maximum muscle diameter D_{max} and the minimum length L_{min} which the mesh can physically attain are given respectively by:

$$D_{max} = \frac{L_y \sin\theta_{jc}}{\pi n} \tag{4-11}$$

$$L_{min} = L_y \cos\theta_{jc} \tag{4-12}$$

This braid jamming state model allows a BPM designer to predicting the muscle's range of axial movement prior to prototype development.

4.3 BPM Volume and Area

The BPM volume and surface area are geometrical parameters that the muscle mechanical modeling is based on. It is deemed important for this work to develop and validate analytical relationships for these parameters which are also unfeasible to measure. The BPM volume and surface area relationships are calculated based on the BPM proposed structure (Figure 4-2). Using common geometrical relationships for a partial cone and a cylinder, the BPM geometrical models are given in Table 4-1.

Table 4-1: BPM geometrical relationships based on Figure 4-2

	$0 \leq x \leq L_L$	$L_L < x \leq L - L_L$	$L - L_L < x \leq L$
BPM volume	$\frac{1}{3}\pi L_L\left[\left(\frac{D}{2}\right)^2 + \left(\frac{d}{2}\right)^2 + \frac{dD}{4}\right]$	$\pi\frac{D^2}{4}(L - 2L_L)$	$\frac{1}{3}\pi L_L\left[\left(\frac{D}{2}\right)^2 + \left(\frac{d}{2}\right)^2 + \frac{dD}{4}\right]$
BPM area	$\pi\left(\frac{D}{2} + \frac{d}{2}\right)\sqrt{\left(\frac{D}{2} - \frac{d}{2}\right)^2 + L_L^2}$	$\pi D(L - 2L_L)$	$\pi\left(\frac{D}{2} + \frac{d}{2}\right)\sqrt{\left(\frac{D}{2} - \frac{d}{2}\right)^2 + L_L^2}$

For experimental measurement of the BPM surface area and volume, an integration technique is used based on the muscle contour function. The contour function retraces the muscle surface (Figure 4-5) with respect to the middle axes of the muscle.

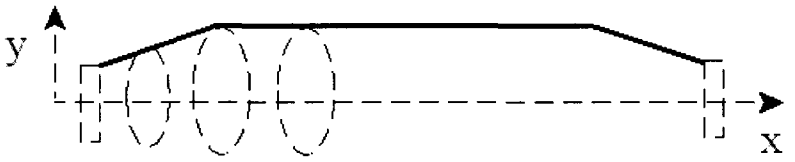

Figure 4-5: Muscle contour shape and its curve as it forms the muscle surface.

The BPM volume is determined by the sum of BPM cross sectional area times a length segment *dx*. The BPM cross sectional area represent the circular area covered by the radius (Figure 4-5) that is defined by the BPM contour function. The BPM surface area is the sum of the product for muscle circumference and the length segment *dx*. The muscle contour function is determined from digital pictures of the muscle for different contraction distance using the software DataGraph.

4.4 BPM Geometric Models Validation

Based on the literature survey, most geometrical models that are employed to analyze the muscle motion rely on the assumption that the muscle retains a cylindrical shape throughout its operation. To show the inaccuracies of this, two experiments are conducted, the first experiment examines the geometrical muscle properties for the entire muscle (Figure 4-6, sections A, B and C) and the second experiment examines the geometrical muscle properties for the muscle cylindrical part (Figure 4-6, section B). Figure 4-7 shows the experimental length results and the calculated length results using the Equation (4-2) for the entire muscle. This equation was derived based on cylindrical braid shape assumption.

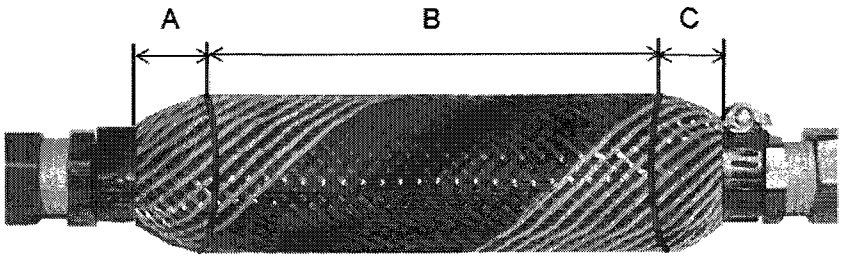

Figure 4-6: Illustration of the BPM prototype with the marked lines that show the entire muscle (sections A, B and C) and the cylindrical part (section B).

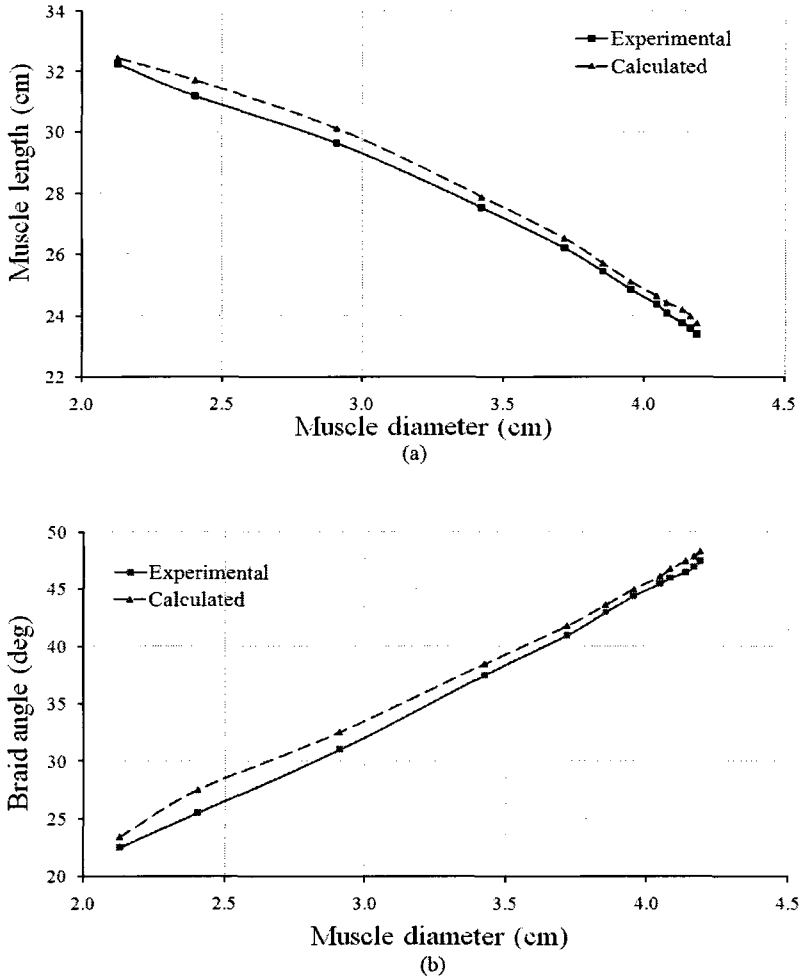

Figure 4-7: Muscle length (a) and braid angle (b) validation results of the n2_D1.9_E1.3 prototype for the entire muscle (sections A, B and C).

Figure 4-7 shows that the calculated length for the entire muscle yields to significant errors mainly in full muscle relaxation and contraction positions. The calculated values overestimate the muscle geometrical properties. This is attributed to the cylindrical assumption of the muscle shape. The Root Mean Square (RMS) error for the muscle length and the braid angle are determined to be 0.31 cm and 0.99 degrees, respectively. The Normalized Root Mean Square (NRMS) error for the muscle length and the braid angle are determined to be 3.5 % and 3.9 %, respectively.

$$RMS = \sqrt{\frac{\sum_{i=1}^{n}\left(v_{m,i} - v_{e,i}\right)^2}{n}} \tag{4-13}$$

$$NRMS = \frac{RMS}{v_{em} - v_{ei}} \tag{4-14}$$

where v_m is the model value, v_e is the experimental value, v_{em} and v_{ei} are the experimental maximum and minimum values, respectively. To show the validation of a cylindrical shape assumption for the muscle middle section, the experimental length results for the section B is compared to the results obtained using the Equation (4-2). The validation result of this experiment is shown in Figure 4-8. The middle section length experimental value is measured by physically marking the section B on the muscle braid.

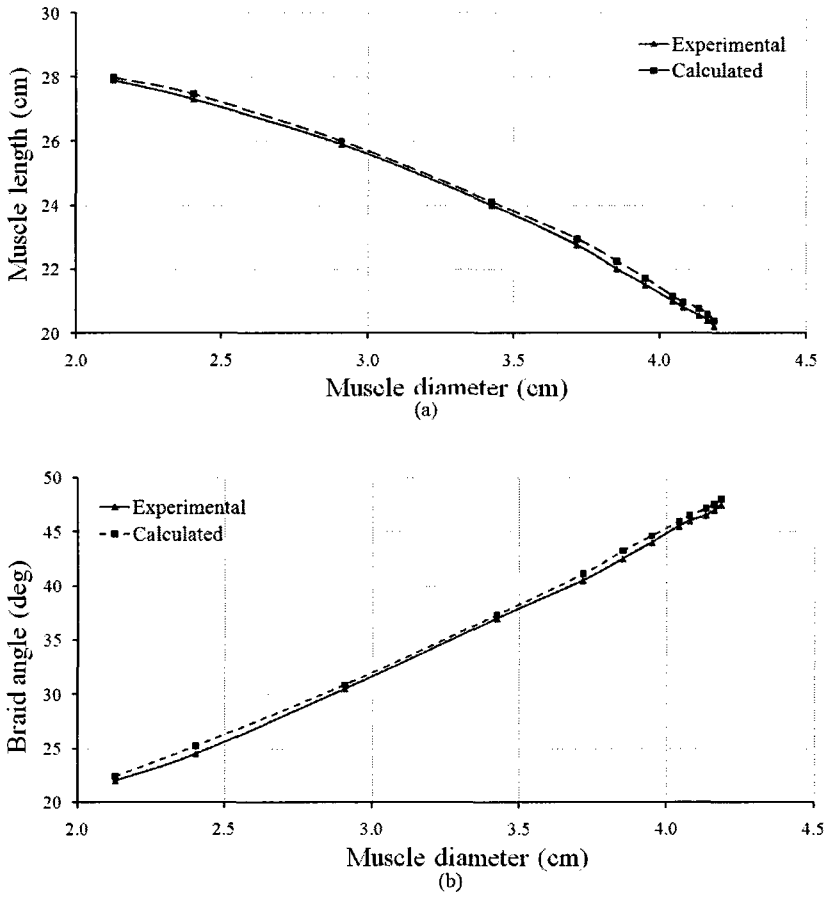

Figure 4-8: Muscle length (a) and braid angle (b) validation results of the n2_D1.9_E1.3 prototype for the middle muscle section B.

Figure 4-8 shows that the calculated middle section length results using Equation (4-2) yield great accuracy. This confirms that the muscle does retain approximately a constant diameter for the muscle middle section. The next step is to validate the geometrical model that is based on the proposed geometrical structure shown in Figure 4-2. Figure 4-9 shows the experimental and the calculated muscle length results using Equation (4-5).

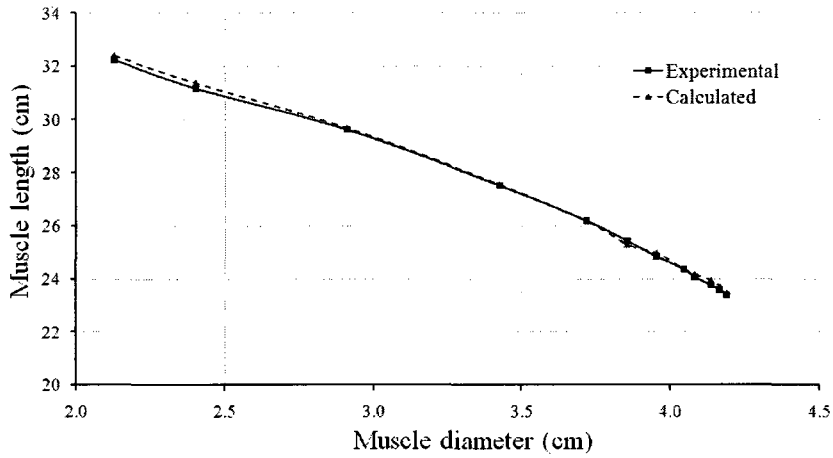

Figure 4-9: Muscle length validation results of the n2_D1.9_E1.3 prototype for the entire muscle (sections A, B and C).

As shown in Figure 4-9, the proposed muscle geometrical structure (Figure 4-2) modeled by its length relationship (Equation (4-5)) yields an effective geometrical model for the entire muscle contraction range. The RMS and NRMS errors for the muscle length are determined to be 0.116 cm and 1.9 %, respectively. The main improvement is at the extremities of the muscle operation range where the muscle irregular forms take place. The new BPM geometrical model improves greatly the muscle motion prediction for short muscle's original lengths (n1 and n2), however, as the muscle length increases beyond the *n2* lengths, the geometrical ends distortion becomes a smaller portion of the overall muscle geometry and thus the cylindrical assumption for the entire muscle becomes more accurate.

The geometrical modeling validation is extended to cover the muscle surface area. Figure 4-10 shows the experimental muscle surface area results with comparison to two calculated models results. The experimental data is determined using digital images of the muscle. Using these

images and the software Getdata Graph Digitizer [45], an array of data is identified which forms the muscle contour. Subsequently, using this array, a numerical integration is applied in MatLab to calculate the muscle surface area for each contraction distance. Figure 4-10 shows the muscle volume results for two models and the experimental data. Model 1 is determined using the relationship given in Table 4-1 and such it is based on the proposed BPM structure shown in Figure 4-2 and model 2 is based on a cylindrical assumption for the muscle and its value is calculated using a standard volume relationship of a cylinder.

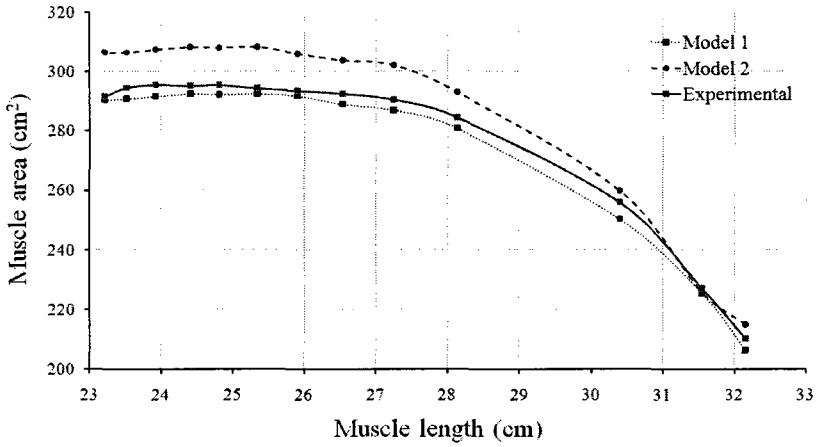

Figure 4-10: Muscle surface area validation results of the n2_D1.9_E1.3 prototype for the entire muscle section A-D.

As expected, Figure 4-10 reaffirms that assuming a cylindrical form for the entire muscle leads to overestimating the muscle surface area. The discrepancy of the muscle surface values increased as the muscle contracts to a larger diameter or shorter length. For model 1, the RMS and NRMS errors for muscle surface area are determined to be 0.12 cm^2 and 3.9 %, respectively. For model 2, the RMS and NRMS errors for muscle surface area are determined to be 10.9 cm^2 and 11.7 %, respectively.

As discussed earlier, the BPM is confined by a braided mesh which possesses unique geometrical properties. The braid jamming states correspond to the braid physical contraction and relaxation limits. Table 4-2 shows the experimental and the calculated jamming angles for muscle maximum contraction and relaxation using Equation (4-10).

Table 4-2: Validation results for the jamming angle at maximum braid contraction and relaxation for the n2_D1.9 and n1_D0.9 prototypes.

Braid	Calculated jamming angles (degrees)		Experimental jamming angles (degrees)	
	Relaxation	Contraction	Relaxation	Contraction
n2_D1.9	12	78	14	76
n1_D0.9	13.5	76.5	15	75

Table 4-2 shows that the braids n2_D1.9 and n1_D0.9 have similar calculated jamming angles. Both braids are composed of similar fibre diameters and have similar ratio of number of fibres over the fibre length per *n*. The calculated jamming angles values using Equation (4-10) show a slight discrepancy with respect to the experimental values. This is primary due to two factors: the braid fibres in the physical jamming state are unable to lay parallel and touching each other, and that the fibres are not flat as assumed and that their weave undulations was not taken into account in the theory.

4.5 Muscle Geometry Properties

The muscle is designed for a range of operating modes. It is important to confirm that the derived geometrical model is valid for these ranges. This is achieved by demonstrating that the muscle possesses constant geometrical properties when an external load or a supply pressure is modified. Figure 4-11 shows the relation of muscle length versus muscle diameter as the hanged static mass increased from 2.3 Kg to 9.1 Kg.

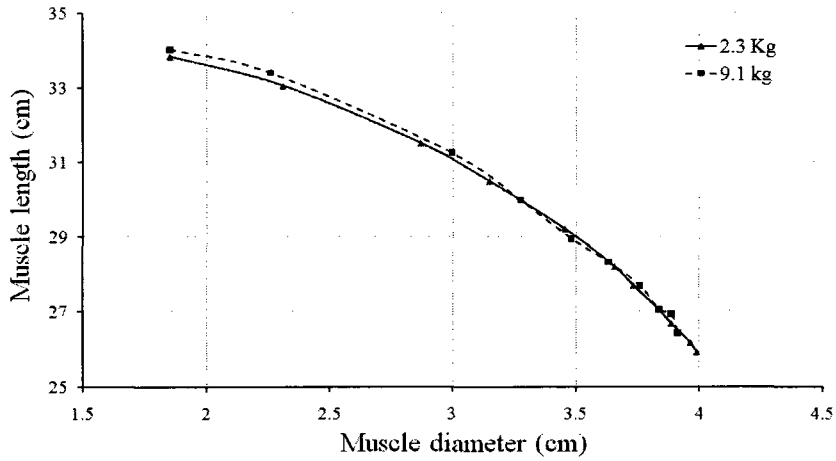

Figure 4-11: Muscle length validation results of the n2_D1.9_E1.3 prototype for two hanged mass of 2.3 Kg and 9.1 Kg.

In a later chapter, it will be also shown that the muscle stress causes limited fibre deformation. Thus, the design maximum supply pressure range (250 kPa) results in a very low fibre tensile strain (approx. 0.3 %). Therefore, the muscle geometry properties are assumed constant and the proposed model is valid for the designed operating range.

Chapter 5

BPM Static Modeling

The BPM static model is necessary for muscle design and control. Static models of BPMs reported in the research literature predict fairly accurately the muscle force carrying capacity. These models, however, rely on experimentally determined parameters that are only valid for the specific muscle configuration under consideration. This chapter presents a fully analytical BPM static model that does not depend on experimentally determined parameters. The proposed approach is based on Newtonian mechanics which considers the mechanical and the geometrical properties of the muscle. Distinctively, this approach includes the muscle end fixture diameter effect. Results from the developed model are compared to experimental ones obtained from prototype BPMs.

5.1 BPM Material Properties and Testing

In order to develop a comprehensive BPM model that is suitable for different configurations and sizes, it is necessary to accurately determine the mechanical properties of the BPM constitutive materials so as to include them in the model. Since the BPMs used in this work were designed and built in-house, such an investigation was possible. In this section, the muscle bladder and braided mesh mechanical properties are modeled analytically with input parameters obtained from materials testing. These models are later incorporated in the overall BPM static model.

5.1.1 Muscle Bladder Properties

The BPM bladder is a butyl rubber (polyisobutylene) tube whose main role is to act as a seal for the compressed gas in the BPM. However, as it is inflated its elastic properties offer an almost conservative resistive force to the muscle expansion. Therefore, the bladder's mechanical properties must be taken into consideration when developing the BPM model. These properties were determined through tensile tests on rectangular bladder material strips. The strips are taken from the hoop and longitudinal directions of the bladder. The dimensions of the test strips are 3.3 cm in length, 2.5 cm in width and 0.1 cm in thickness. The stress-strain test results in both directions of the bladder are similar as shown in Figure 5-1.

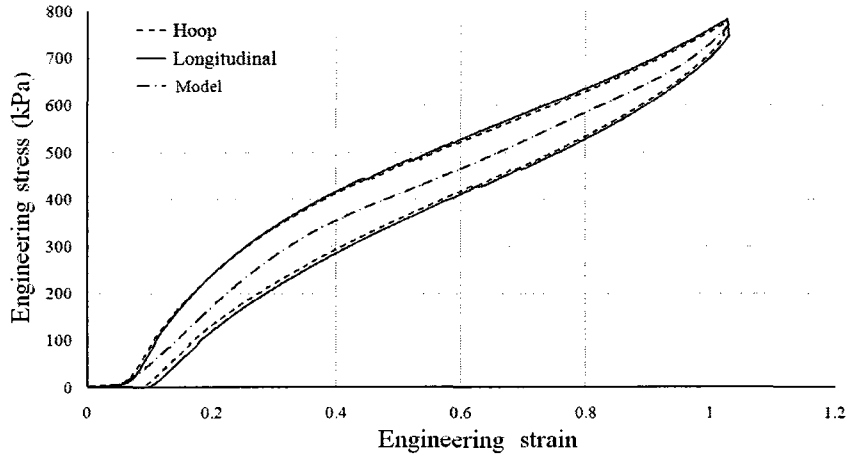

Figure 5-1: Experimental tensile test and model results for the bladder material.

The area under the hoop curve in Figure 5-1 represents the energy stored, and the area enclosed by this curve represents the energy lost internally in the material. The figure shows that the stored and lost energies in samples taken from the hoop direction are approximatively 0.26 J and 0.073 J, respectively. Since these energies are proportional to the sample volume, then a typical BPM prototype of 2 cm diameter and 33 cm long would have approximatively 6.6 J and 1.8 J, of stored and lost energies, respectively when being inflated to a diameter of approximately 4 cm. This is the case when this prototype is subjected to a supply pressure of 207 kPa. Based on Table A-4, these energy values represent approximately 8.3 % and 2.3 % of the total stored and lost BPM energies, respectively for such a prototype. Given these results, the hysteresis in the bladder material, represented by the area enclosed by the curve in Figure 5-1, is neglected in this work. However, the bladder mechanical behaviour in both directions are considered in the force analysis model. Based on the results of Figure 5-1, the bladder material stress-strain relationship is approximated as follows:

$$\sigma_b = 17331\varepsilon^6 - 58131\varepsilon^5 + 75592\varepsilon^4 - 46824\varepsilon^3 + 13175\varepsilon^2 - 408\varepsilon - 3.5 \qquad (5\text{-}1)$$

where σ_b is the tensile stress in kPa. Equation (5-1) represents the model curve in Figure 5-1.

5.1.2 Braided mesh Properties

The braided mesh functions as a restraint to the bladder and defines the geometrical properties of the BPM. The prototype braid is made of four PET monofilament of 0.254 mm diameter grouped together to form a flat band approximately 0.96 mm wide. PET is a semi-crystalline thermoplastic polymer with excellent wear resistance, low coefficient of friction, high Young modulus, and very low water absorption. A tensile test result for the PET filament used is shown in Figure 5-2. The results show that PET fibre has a high elastic modulus (~3GPa) to resists fibre elongation. For the maximum design pressure of 250 kPa for the prototype the expected tensile strain is less than 0.003. Therefore, for a typical BPM prototype of 35 cm yarn length (*i.e.* L_y), a 0.11 cm length elongation would occurs due to the elasticity of fibre's material. This elongation represents approximately 1.2 % of the 9.2 cm muscle contraction distance achieve by this prototype (Table A-1). Consequently, fibre elongation is considered negligible and is not accounted for in the development of the BPM.

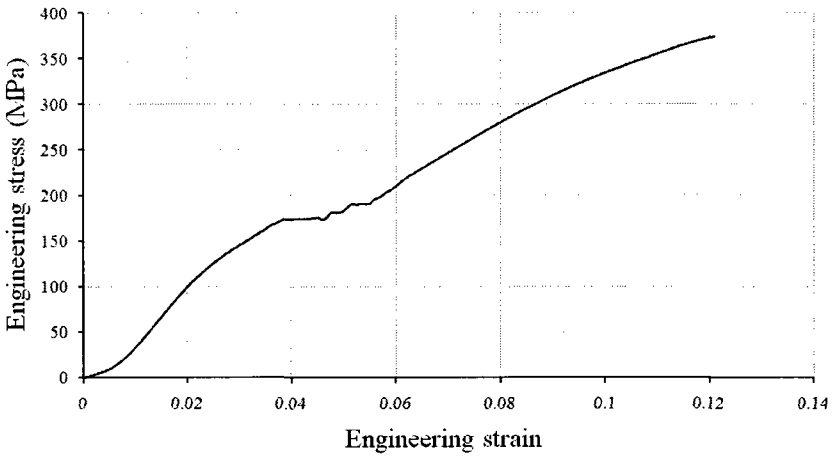

Figure 5-2: Experimental tensile test results for a PET fibre.

The coefficient of friction for the PET material ranges between 0.2 and 0.3 [48]. The value of the coefficient of friction can be affected by the sliding speed, temperature and relative humidity.

5.2 BPM Stress Analysis Based on Force Analysis

The primary model of a BPM is one that maps the relationship between the muscle pressure P and the resulting muscle force F. A small number of researchers included factors in their BPM models to account for the non-cylindrical shape of the muscle end zones. The shape of the end zones depends on the diameter of the muscle and that of the end fixture. This model includes the effect of the end fixture size.

The BPM static model is obtained by considering the equilibrium of all the internal and applied forces shown in the half-section view in Figure 5-3. The muscle surface forces due to the muscle pressure must be transferred to an equivalent longitudinal force (net muscle force) F along the muscle contraction axis. Thin-walled pressure vessel analysis is adopted for the purpose of deriving the stresses on the muscle internal walls. The use of Thin-walled pressure theory is validated by confirming that the ratio of the muscle diameter to muscle membrane thickness is larger than 10, P represents a gage pressure, muscle material is assumed isotropic and

homogeneous, stress distributions throughout the muscle membrane thickness do not vary and the compressed fluid inside the muscle has negligible weight. Subsequently, the muscle stresses are transformed into the resultant tension within the braid fibres and then to muscle ends. This method results in the relationship of the net muscle force F as a function of the muscle pressure P.

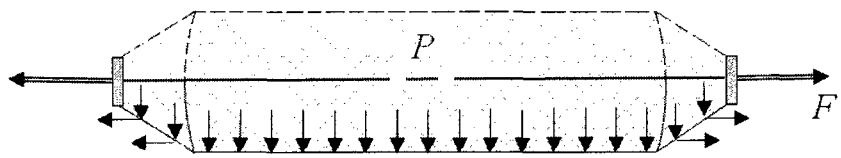

Figure 5-3: Proposed BPM structure with applied surface forces, muscle pressure P and muscle force F.

The muscle pressure results in a longitudinal stress σ_L, a hoop stress σ_H, and a radial stress σ_r in the muscle wall. The radial stress is ignored due to the assumption of a thin-walled pressure vessel. The relationship between the longitudinal and hoop stresses and the muscle pressure of the bladder can be derived by examining its free body diagram. The muscle is divided into three geometrical shapes, namely, a cylindrical section that represents the center part of the muscle and two truncated cones that represent the ends.

5.2.1 BPM Hoop Stress

Figure 5-4 shows a schematic diagram of a half of a cylindrical section of length dx of the muscle with the acting stresses indicated.

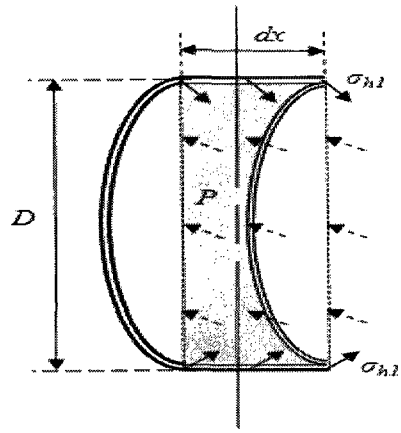

Figure 5-4: Schematic diagram for the stresses applied on a BPM cylindrical section *dx*.

In this figure, the dotted arrows represent the forces applied by the muscle pressure P on the projected area of the cylinder and the solid arrows represent the forces within the muscle wall. Static equilibrium of the forces indicated in Figure 5-4 results in the following relationship:

$$\sum F_h = 0$$

$$2[\sigma_{h1} A_f] + 2[\sigma_{bh1} A_{bh1}] - P A_{pc} = 0$$

$$\sigma_{h1} = \frac{P(D - 2t_f - 2t_b) - 2\sigma_{bh1} t_b}{2t_f} \tag{5-2}$$

where F_h are the forces in the hoop direction, σ_{hl} is the hoop stress, D is the muscle diameter, t_f is the braid thickness, t_b is the muscle wall thickness, σ_{bhl} is the stress in the bladder, A_f is the fibre cross sectional area, A_{bh} is the bladder cross-sectional area and A_{pc} is the projected area of the BPM cylinder section.

The approximate geometry of the end segments is shown in Figure 5-5.

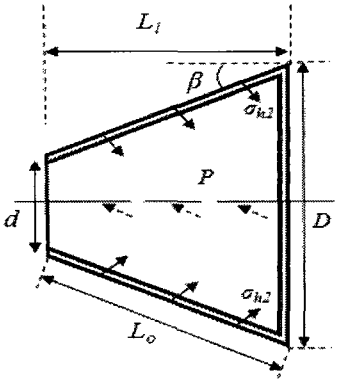

Figure 5-5: Illustration of the partial cone that represents the muscle ends for the proposed BPM structure.

In this figure, the dotted arrows represent the forces applied by the muscle pressure P on the projected area of the partial cone and the solid arrows represent the forces within the muscle wall. With reference to the Figure 5-5, the end segment average hoop stress σ_{h2} is given by:

$$\sum F_h = 0$$

$$2[\sigma_{h2}A_f] + 2[\sigma_{bh2}A_{bh2}] - PA_{pc2} = 0$$

$$\sigma_{h2} = \frac{P(D + d - 4t_b - 4t_f)\cos\beta - 4\sigma_{bh2}t_b}{4t_f} \tag{5-3}$$

where d is the end fixture diameter, A_{pc2} is the projected area of the cone, σ_{bh2} is the average stress in the bladder, A_{bh2} is the bladder cross-sectional area and β is the BPM cone angle or the braid inclination angle at muscle ends.

5.2.2 BPM Longitudinal Stress

The longitudinal stress can be determined by considering a free body diagram of the partial cone (Figure 5-6).

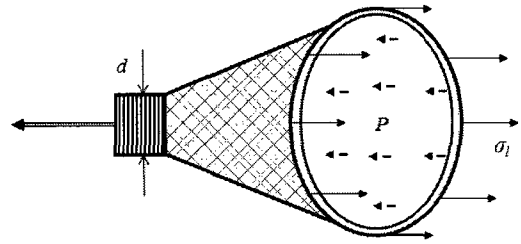

Figure 5-6: Illustration of the applied loading on the muscle partial cone section.

In this figure, the dotted arrows represent the forces applied by the muscle pressure P on the projected area of the cone and the solid arrows represent the forces within the muscle wall. With reference to Figure 5-6, the expression for the longitudinal stress is given approximately by:

$$\sum F_l = 0$$

$$\sigma_l A_f + \sigma_{bl} A_{bl} - P A_{pc} = 0$$

$$\sigma_l = \frac{P\left(\frac{D}{2} - t_f - t_b\right)^2 - \sigma_{bl} D t_b}{D t_f} \tag{5-4}$$

where F_l is the force in the longitudinal direction, σ_{bl} is the stress in the bladder in the longitudinal direction, A_{bl} is the bladder cross-sectional area in the longitudinal direction and σ_l is the longitudinal stress.

5.3 BPM Fibre Tension Analysis

The muscle wall stresses which act on the braid fibres produce a tensile force in the fibres. The tension in these fibres acts on the end caps to produce the muscle force. A schematic diagram of the forces on an element of the muscle wall is shown in Figure 5-7.

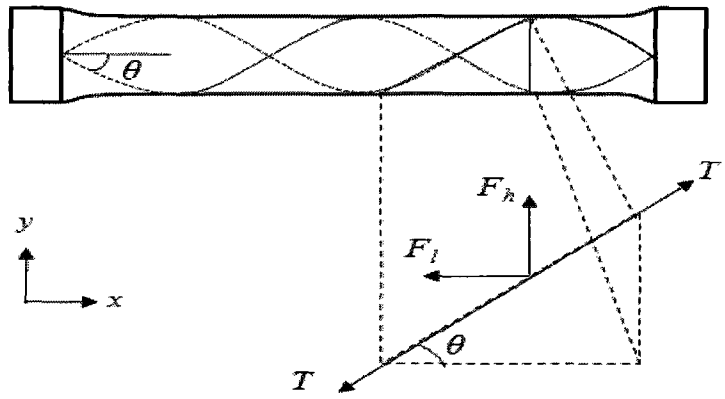

Figure 5-7: Fibre's tension, longitudinal and hoop forces acting on BPM.

A balance of the forces acting in the longitudinal and hoop directions on the element results in the following:

$$\sum F_y = 0$$

$$F_h = nNT_h sin\theta \tag{5-5}$$

$$\sum F_x = 0$$

$$F_l = NT_l cos\theta \tag{5-6}$$

where T_h and T_l are the tension in the braid fibres due to the hoop stress and the longitudinal stress, respectively, F_h and F_l are the hoop force and the longitudinal force resulting from stresses applied by the pressure, respectively, N is the number of fibres (four fibres per flat band), n is the number of fibre revolutions per braid length, and θ is the fibre braid angle. Since stress is force per unit area:

$$\sigma_h = \frac{F_h}{A_h} \tag{5-7}$$

$$\sigma_l = \frac{F_l}{A_l} \tag{5-8}$$

where A_h and A_l are the areas of the hoop force F_h and the longitudinal force F_l on which the forces are applied, respectively. Solving Equations (5-7), (5-5), (5-3) and (5-2) gives:

$$T_{h1} = \left[\frac{P(D - 2t_b - 2t_f) - 2\sigma_{bh1}t_b}{2nN\sin\theta}\right]L_1 \tag{5-9}$$

$$T_{h2} = \left[\frac{P(D + d - 4t_b - 4t_f)\cos\beta - 4\sigma_{bh2}t_b}{4nN\sin\theta_a}\right]L_o \tag{5-10}$$

where T_{h1} and T_{h2} reflect the tension in the braid fibres due to the hoop stresses in the cylindrical and two cone frustum sections, respectively. For the cone frustum sections, the hoop stress σ_{h2} is assumed to be transformed to a tension based on an average braid angle θ_a which represents the mean value between the muscle end braid angle θ_e and the cylindrical section braid angle θ.

The total fibre tension T_h resulting in the muscle hoop direction is hence given by:

$$T_h = T_{h1} + 2T_{h2} \tag{5-11}$$

Solving Equations (5-8), (5-6) and (5-4) for T_l results in:

$$T_l = \frac{\left[P\left(\frac{D}{2} - t_f - t_b\right)^2 - \sigma_{bl}Dt_b\right]}{ND\cos\theta}\frac{L}{n}\tan\theta \tag{5-12}$$

The net difference between the fibre tension resulting from the muscle hoop stresses and the muscle longitudinal stresses drives the muscle motion. This net fibre tension $\overrightarrow{T_f}$ is given by:

$$\overrightarrow{T_f} = \overrightarrow{T_h} - \overrightarrow{T_l} \tag{5-13}$$

If the net fibre tension is null, the muscle is at equilibrium and this state corresponds to the maximum muscle contraction position. This state will be derived for a simplified muscle model using the netting analysis in Section 5.6.

The braid fibres are locked by mechanical straps to the muscle end fixtures. The tension in these fibres is transmitted to the end caps at a spatial angle whose components are the muscle end braid angle θ_e and the cone angle β as shown in Figure 5-8.

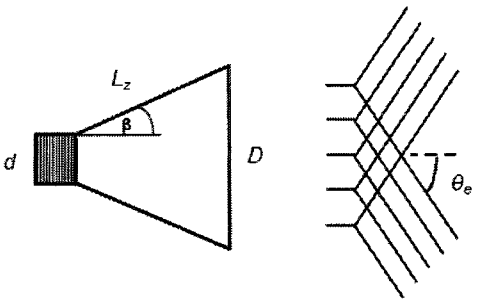

Figure 5-8: Illustration of braid fibre orientation at muscle end.

The projection of the fibre onto the muscle contraction axis is the product of the cosines of the two angles as follows:

$$projection = cos\beta * cos\theta_e \tag{5-14}$$

Therefore, the force produced by the muscle F_m is given by:

$$F_m = NT_f cos\beta * cos\theta_e \tag{5-15}$$

5.4 BPM Static Model

The BPM static model is obtained by balancing the longitudinal forces on the system as follows:

$$\sum F_x = 0$$

$$F - NT_f \cos\theta_e \cos\beta + f_{fs} = 0 \tag{5-16}$$

or

$$F = NT_f \cos\theta_e \cos\beta - f_{fs} \tag{5-17}$$

where F is the net muscle force, the second term in the expression is the force due to the tension in the braid fibres, and f_{fr} is the frictional force in the muscle.

5.5 BPM Friction Model

It is assumed that there is no relative motion (sliding) occurring between the braid and the bladder, and that all the frictional losses are due to the fibre to fibre contact and motion as the braid angle changes. The fibre to fibre contact surface is assumed to be a flat parallelogram element as shown in Figure 5-9. The area of this element is a function of the braid angle.

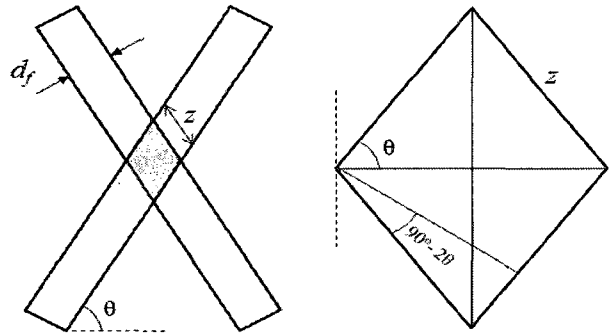

Figure 5-9: Illustrations of (a) two crossing fibres at a braid angle θ (b) parallelogram geometry for the contact surface between two fibres at a braid angle θ.

The parallelogram side z is given by:

$$z = \frac{d_f}{cos(2\theta - 90)} \tag{5-18}$$

where d_f is the fibre width or diameter. The total friction area is equal to the sum of all parallelogram areas in the braid. The number of parallelograms q is calculated based on the assumption that each fibre crosses all other fibres from the other braiding direction twice within one fibre revolution (n = 1) around the braid circumference (Figure 5-10). The fibres cross each other at the end of the braid; however, only one complete helix is considered in the following relationship:

$$q = 2 * n\left(\frac{N}{2}\right)^2 + \frac{N}{2} \tag{5-19}$$

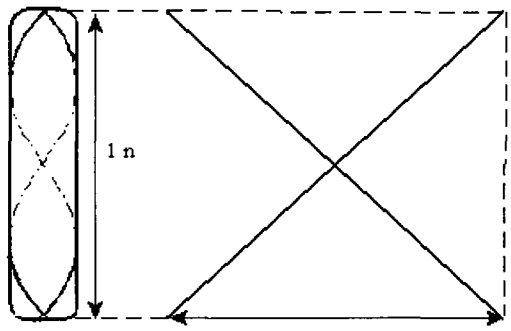

Figure 5-10: Illustration of the fibres crossing for one revolution ($n = 1$).

The total fibre to fibre contact area in the braid A_{ff} is given by:

$$A_{ff} = d_f * z * q \tag{5-20}$$

While Equation (5-20) is valid for a flat contact surface between two crossing fibres, the actual contact area for the muscle is not flat, and can be better approximated by a contact element between two crossing cylinders. Davis and Caldwell [18] developed an analytical model based on Hertz surface theory for two spheres in contact. This model does not reflect the real form of the braid fibres and does not take into consideration the effect of the braid angle change when the BPM contracts or expands. With reference to Figure 5-11, using Hertz theory [49] for two crossing cylinders, an analytical expression for the width contact b is derived next.

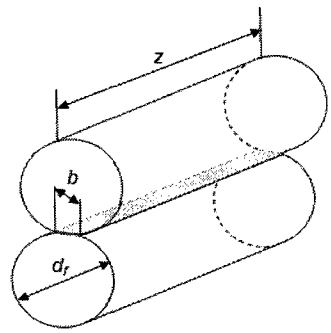

Figure 5-11: The width length contact b between two crossing fibres.

The value of b in Figure 5-11 is given by:

$$b = 1.6\sqrt{pK_D C_E} \tag{5-21}$$

$$p = \frac{F_{rad}}{z} \tag{5-22}$$

$$K_D = \frac{d_f}{2} \tag{5-23}$$

$$C_E = 2 * \frac{1 - v^2}{E} \tag{5-24}$$

where p is the force acting per length of the cylinder, F_{rad} is the force acting on the contact surface, v is fibre material Poisson's ratio, and E is the fibre Young's modulus. The relationship for muscle fibre to fibre contact surface A_{ff} is hence given by:

$$A_{ff} = b * z * q \tag{5-25}$$

The fibre to fibre contact surface relationship (5-25) is compared to Davis and Caldwell model for the n2_D1.9 prototype in Figure 5-12.

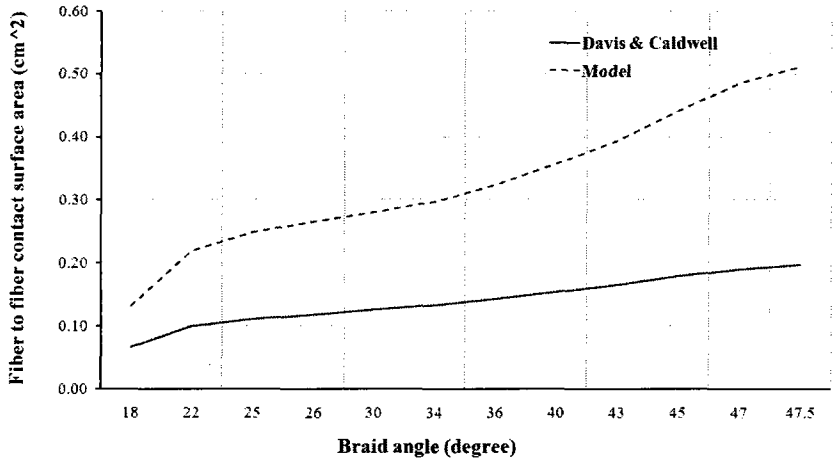

Figure 5-12: fibre-fibre contact surface results for n2_D1.9.

The discrepancy in these results was expected since Davis and Caldwell does not considered the braid angle and the actual shape of the fibre as part of the modeling development. The friction is a tangential force acting between two surfaces in contact. Researchers have yet to derive an accurate compact model to determine its magnitude; however, models as Coulomb and Viscous friction models can be used to predict this. For the BPM mechanism, the friction phenomenon is

complex. This is due to the undulations of the cross fibre weave and the PET properties. In [16], Chou and Hannaford estimated the friction force to be a constant value applied in opposite direction of the muscle motion. In this work the frictional force is assumed to be the result of braid fibre to fibre contact only. Furthermore, the undulations due to the cross fibre weave are ignored, and cross fibres are assumed to simply lie on top of each other. For polymeric materials (*e.g.* PET), the sliding speed, temperature and relative humidity affect the frictional force, however, in this work, the static and dynamic friction coefficients are assumed to be constant. The complete expression for this frictional force f_{fr} is given by:

$$f_{fr} = \begin{cases} -P_2 A_{ff} \mu_d & v < 0 \\ \sum F_x + P A_{ff} \mu_d & \sum F_x \leq 0, v = 0 \\ P_2 A_{ff} \mu_s & \sum F_x > 0, v = 0 \\ P_2 A_{ff} \mu_d & v > 0 \end{cases} \tag{5-26}$$

where μ_s and μ_d are the static and dynamic coefficients of friction, respectively. For the static case, the friction force expression reduces to:

$$f_{fs} = P A_{ff} \mu_s \tag{5-27}$$

5.6 Maximum BPM Contraction Distance

In theory the braid can foreshorten until the jamming state where the angle between the intertwining fibres cannot increase any further. When the braid is part of the muscle, the minimum length that can be achieved is much less than that of the jamming state. The BPM maximum contraction distance corresponds to the length that the muscle reaches regardless of any increase of muscle pressure. Based on experimental results (Table A-1), the muscle contracts an average of 30 % of its original length where the braid angle corresponds to 48°. Assuming the BPM to be cylindrical, and ignoring the contributions of the bladder, the minimum theoretical braid angle that the BPM can achieve is obtained using netting analysis [50]. In the absence of the bladder and the cylindrical assumption, the hoop and longitudinal stresses relationships are:

$$\sigma_L = \frac{pD}{4t} \tag{5-28}$$

$$\sigma_H = \frac{pD}{2t} \tag{5-29}$$

Applying the force analysis shown in Figure 5-7, these relationships yield:

$$\frac{NnT_h \sin\theta}{Lt_f} = \frac{PD}{2t} \tag{5-30}$$

$$\frac{NnT_l \cos\theta}{Lt_f \tan\theta} = \frac{PD}{4t} \tag{5-31}$$

For the maximum contraction, the net tension in fibre is null and therefore the tensions T_h and T_l are equivalent. Dividing Equation (5-30) by Equation (5-31) yields:

$$tan^2\theta = 2$$

The above relationship results in a braid angle of 54.7° for the maximum contraction distance of the BPM when all losses are ignored.

5.7 BPM Stiffness

As stated in the literature survey, some researchers (*e.g.* Chou and Hannaford [16]) simplified the muscle model by assuming that the BPM behaves as an air spring. In such a case, the muscle stiffness is required and so far this has been experimentally determined by others. In this work, an analytical muscle stiffness model was developed based on the static model. The muscle stiffness K can be expressed as a function of the muscle force variation dF over the muscle length elongation dL as follows:

$$K = \frac{dF}{dL} \tag{5-32}$$

Assuming that the muscle retains a cylindrical shape and the muscle wall thickness, the muscle friction and the muscle bladder are ignored, Equations (5-9) and (5-12) yield to:

$$T_h = \frac{PD}{2nN\sin\theta}L \tag{5-33}$$

$$T_l = \frac{PD}{4N\cos\theta}\frac{L}{n}\tan\theta \tag{5-34}$$

The hoop tension (Equation (5-10)) resulting from the conical parts is null since the muscle is assumed cylindrical shape and thus the new hoop tension T_h (Equation (5-9)) covers the entire muscle length. Substituting Equations (5-33) and (5-34) and in Equation (5-16) yield to:

$$F = \left(\frac{PD}{2n\sin\theta}L - \frac{PD}{4n\cos\theta}L\tan\theta\right)cos\,\theta \tag{5-35}$$

where β is assumed to be 0 degrees due to the cylindrical assumption. Equation (5-35) is manipulated as follows:

$$F = \frac{PD}{2n\tan\theta}L - \frac{PD}{4nN}L\tan\theta \tag{5-36}$$

Using Equation (5-3) and the braid geometry given in Figure 4-3, Equation (5-38) yields to:

$$F = \frac{PL^2}{2\pi n^2} - \frac{P\left(L_y^2 - L^2\right)}{4\pi n^2} \tag{5-37}$$

or

$$F = -P\left[\frac{L_y^2 - 3L^2}{4\pi n^2}\right] \tag{5-38}$$

Using Equations (5-38) and (5-32) yields to:

$$\frac{dF}{dL} = \frac{dP}{dL}\left[-\frac{L_y^2 - 3L^2}{4\pi n^2}\right] + \frac{3PL}{2\pi n^2} \tag{5-39}$$

Assuming an ideal gas, the muscle pressure P is expressed as follows:

$$P = \frac{MRT}{V} \tag{5-40}$$

where M is the mass of the gas, T is the temperature of the gas, V is the muscle volume, and R is the universal gas constant. Equation (5-40) is linearized by taking its partial derivative, expanding the derivatives using Taylor's series, and neglecting all higher order terms:

$$\frac{m}{M} = \frac{p}{P} + \frac{v}{V} - \frac{t}{T} \tag{5-41}$$

With reference to Equation (5-41), the upper-case symbols denote state variables while the lower-case symbols denote the variations. Assuming a polytropic process (*i.e.* thermodynamic process that obeys the relation PV^{ng} = constant), this will cast (5-41) as follows:

$$\frac{p}{P} = n_g \frac{m}{M} - n_g \frac{v}{V} \tag{5-42}$$

where the value of n_g varies between 1 for an isothermal process to 1.4 for an adiabatic process. For the stiffness test, the air mass inside the muscle is conserved. Therefore, Equation (5-42) yields to:

$$p = -Pn_g \frac{v}{V} \tag{5-43}$$

Or

$$\frac{dp}{dL} = -n_g \frac{P}{V}\left(\frac{L_y^2 - 3L^2}{4\pi n^2}\right) \tag{5-44}$$

This gives to the muscle stiffness model as follows:

$$\frac{dF}{dL} = n_g \frac{P}{V}\left(\frac{L_y^2 - 3L^2}{4\pi n^2}\right)^2 + P\frac{3L}{2\pi n^2} \tag{5-45}$$

The accuracy of the stiffness model Equation (5-45) is shown in Figure 5-13 for the n2_D1.9 prototype. Based on Figure 5-13, the model solution starts to deviate from the experimental results when the muscle length elongation reaches approximately 5 cm. This discrepancy between the model and the experimental results could be a result of many factors. The BPM frictional force was ignored, the muscle shape was assumed cylindrical, an ideal gas equation with an adiabatic process was adopted, and the bladder mechanical properties are neglected.

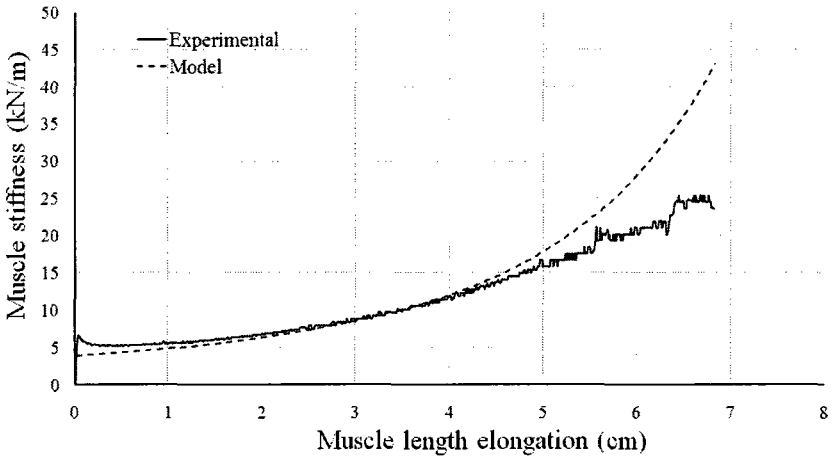

Figure 5-13: Muscle stiffness model validation results for n2_D1.9 prototype

5.8 Experimental Validation for Static BPM Model

For the static model validation and analysis, isometric contraction tests for nine prototype BPMs similar to those shown in Figure 3-4 are performed. The BPM isometric contraction test was done by first restraining the BPM prototype at a fixed length in an Instron tensile testing machine, inflating the muscle and recording muscle force values as a function of the muscle pressure (*i.e.* from 0 to 207 kPa). Table A-5, Table A-6, Figure 5-14 and Figure 5-15 show the experimental muscle force values, the accuracy of the proposed model Equation (5-17) and that of Chou and Hannaford Equation (2-14) with respect to experimental values for the nine muscle prototypes at different contracted lengths. These accuracies are determined using the RMS error and the NRMS error for the muscle force.

Whereas there are developed static models other than Equation (2-14), they cannot be compared since they rely on experimentally determined parameters valid only for the specific muscle configuration under consideration. The model Equation (5-17) results are computed based on a single measured parameter (*i.e.* L). All other muscle parameters are calculated using the derived relationships in this thesis. This model Equation (5-17) is purposely derived to predict the muscle force based on a feasible measured parameter that is the muscle contracted length.

The results in Table A-5 and Table A-6 reveal a number of characteristics of the BPM in relation to the muscle design parameters. As discussed in the following sections.

Contracted muscle length:

In these experiments, the muscle was held and inflated at the contracted length indicated by Lxxx. In all tests, the recorded muscle force decreases as the muscle length shortens. This is also true for the proposed model Equation (5-17) since the net fibre tension Equation (5-13) decreases in value as the braid angle increases or when the muscle length shortens.

Table A-5 and Table A-6 show that accuracy of the proposed model decreases as the muscle length shortens. This result can be attributed to the validity of the assumptions as the muscle contracts. In this work, the muscle end distortions are modeled by two frustum cones; however, this becomes less accurate as the muscle reaches large end distortions at near maximum contraction. Moreover, the standard coefficient of friction for the braid material and the fibre to fibre friction area model decrease in accuracy as the muscle shortens and the braid fibres undulations increase due to the cross weave of the fibres. The increase in undulation and the flattening of the fibres increases the fibre to fibre contact area which has not been accounted for in the fibre to fibre contact assumption.

End fixture diameter:

As the muscle is inflated, the muscle average diameter increases while the muscle end diameters remain unchanged. Thus, for smaller end fixtures, a greater distortion will result at the muscle ends. These experimental results show that a smaller end fixture for the same muscle diameter tends to decrease the maximum achievable muscle force. This can be explained theoretically by referring to Equation (5-17) and by noting that an increase in the cone angle β diminishes the second term which generates the muscle force.

Table A-5 and Table A-6 also show that the proposed model accuracy decreases for small end fixture diameter prototypes (e.g. E1.3). This is attributed to the increase in muscle end distortion as the end fixtures decrease in size.

Original braid length:

Table A-5 and Table A-6 show muscle isometric contraction test results for nine prototypes that are of different original braid lengths. All prototypes with similar original braid diameter have reached approximately similar maximum muscle forces when the muscle pressure reached 207 kPa. This result indicates that the muscle force is largely independent of the original braid length. The muscle force is rather a function of the muscle diameter D and pressure P.

Whereas it should have been expected that the relationship between n and the muscle contraction would be linear and corresponds to a braid angle of 54.7°, the results show that as n increases the maximum contraction per revolution diminishes. This discrepancy between theory and experiment can be attributed to neglecting the losses when deriving the maximum contraction length in Section 5.6. As n increases, so do the muscle length and the frictional force. This in turn causes an increase in the limiting braid angle that can be achieved.

Theoretically, the accuracy of the proposed model Equation (5-17) should be consistent for prototypes that are built with analogous original braid diameter and end fixture diameter. The frustum cone geometry that models the end muscle for such muscle prototypes is assumed invariant irrespective of the prototype original braid length. However, Table A-5 and Table A-6 show that the accuracy of the model for different prototype length is inconsistent. This is attributed primarily to the unmodeled effect of braid fiber undulation highlighted previously.

Original braid diameter:

The results in Table A-5 and Table A-6 show that the original braid diameter considerably affects the muscle force. As an example, the prototype with an original braid diameter of 1.9 cm reached a muscle force that is approximately 6 times greater than that for the prototype having an original braid diameter of 0.9 cm. In term of model accuracy both original braid diameter prototypes have achieved similar accuracies, provided that the end fixture size is relatively close to the original braid diameter.

The accuracies of the proposed model Equation (5-17) and that of Chou and Hannaford Equation (2-14) are plotted graphically in Figure 5-14 and Figure 5-15. As can be seen in Table A-5, Table A-6 and Figure 5-14, the proposed model has better accuracy than that of Chou and Hannaford

for all tested prototypes. Figure 5-16 and Figure 5-17 show the muscle isometric contraction test results for the lowest and highest differences of the NRMS values for the two models, respectively. The proposed modeling approach which is based on Newtonian mechanics took into consideration all muscle mechanical and geometrical properties and thus succeeded in developing a reliable and higher accuracy analytical model.

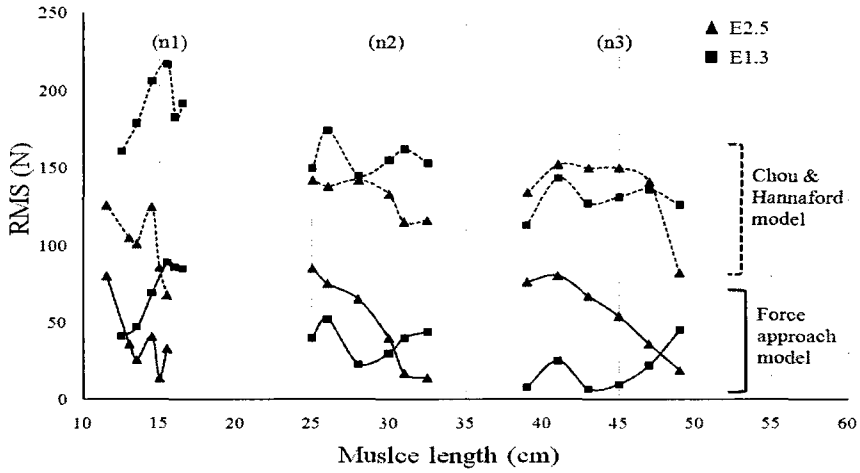

Figure 5-14: BPM static model NRMS results for the D1.9 prototypes as combination of fibre revolutions per muscle length (n1, n2, n3) and end fixture diameter (1.3 cm, 2.5 cm) as a function of muscle length.

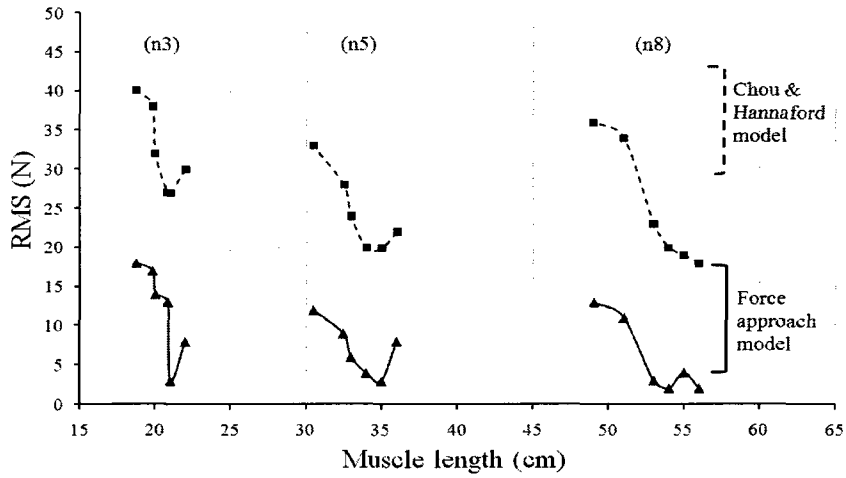

Figure 5-15: BPM static model NRMS results for the D0.9_E1.3 prototypes as combination of fibre revolutions per muscle length (n1, n2, n3) as a function of muscle length.

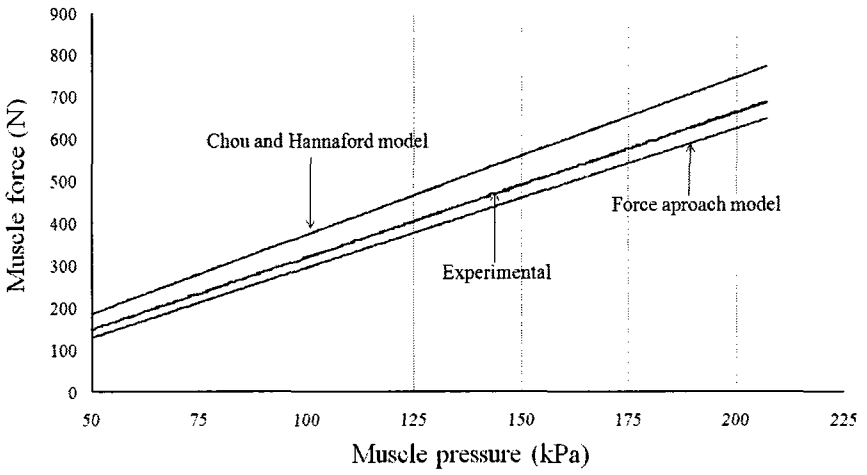

Figure 5-16: BPM static model validation results for the n1_D1.9_E2.5 prototype at a fixed length of 15.5 cm. The force approach model and Chou and Hannaford model achieved the lowest NRMS values of 5 % and 10 %, respectively.

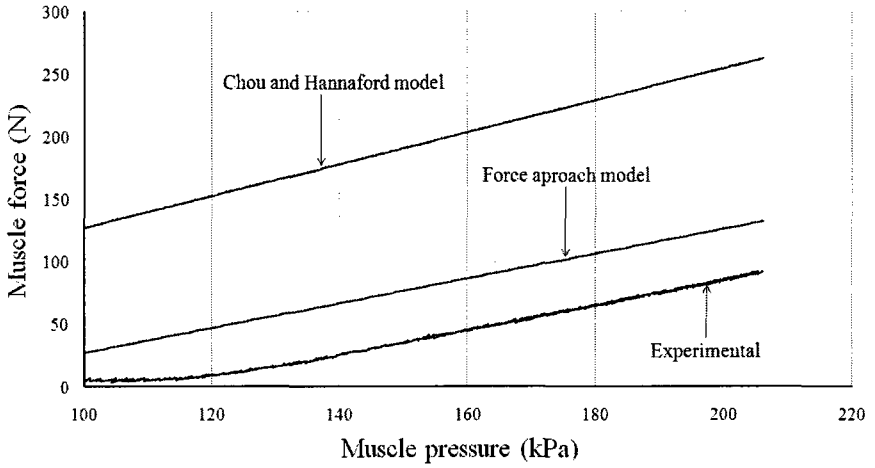

Figure 5-17: BPM static model validation results for the n1_D1.9_E1.3 prototype at a fixed length of 12.5 cm. The force approach model and Chou and Hannaford model achieved the highest NRMS values of 44 % and 175 %, respectively.

Chapter 6

BPM DESIGN

The BPM is a promising form of linear actuator. However, no comprehensive design procedure has been developed or reported in the open literature. In previous chapters, the BPM has been experimentally analyzed and analytical models to predict the muscle geometry, muscle stiffness and muscle force have been developed. This chapter presents a comprehensive and reasoned design process for selecting the appropriate BPM parameter and configuration for a given practical application. Specifically, this chapter presents experimental results for key BPM parameters, BPM analytical models and design steps for two cases, namely, muscle concentric contraction and isometric/eccentric cases. Numerical values are illustrated for the steps in the proposed design process.

Biological muscle action is classified as either isometric, eccentric, or concentric contraction. Isometric contraction involves muscle force generation against an external load with no or minimal movement. Eccentric contraction is similar in nature to the isometric one; however here the muscle is subjected to an increase in load, and any change in muscle length is governed by its stiffness. These two modes of contraction are very similar and thus will be treated in this work as a single case for design. Concentric contraction involves the generation of force, but differs from the previous two modes as significant movement (contraction/elongation) of the muscle occur. This mode will be treated as a second case for design, but is discussed firstly.

6.1 Design Process for Concentric Contraction Applications

When a BPM is to be used in an application requiring a concentric contraction, the critical design parameters are the range of muscle contraction distance and the muscle force. The range of muscle contraction distance depends on the muscle original braid diameter and the difference between the muscle lengths at the two braid jam angles. From a geometrical perspective, the braid jamming angles are 12° and 78° (*i.e.* for the selected type of braid in this study irrespective their length). The theoretical jam angles when muscle forces are considered are 13.5 ° for the fully stretched muscle and 54.7 ° when the muscle is not loaded and contracted fully. At this contracted state, as indicated in Section 5.6, the hoop and longitudinal forces balance. Values of 15° and 48° were found experimentally for the prototypes. Therefore, in order to operate in a mid-range beyond which the muscle is of no practical use since the muscle produces an insignificant force, the minimum and maximum braid angles are have been chosen as 20° and 40°. The muscle force is primarily a function of the original braid diameter and the muscle pressure.

In order to facilitate the design process for the concentric contraction case, a composite design chart is presented in Figure 6-1. This approach was first used by Fahim [51] for another design application. This figure shows two quadrants with different horizontal axis (*i.e.* contraction distance and muscle force) but with a common vertical axis, the original braid diameter of the muscle. The right quadrant of Figure 6-1 illustrates the muscle force as a function of the original

braid diameter and for the indicated pressure on each curve (*i.e.* 80 - 280 kPa). Moreover, for these curves, the muscle force was calculated using Equation (5-16) for a braid angle of 30°. This braid angle value was selected since it is at a midrange for the muscle force value. The left quadrant of Figure 6-1 shows the muscle contraction distance as function of the original braid diameter for multiple integer values of the number of helix turns n (*i.e.* 1 to 6). Moreover, for these curves, the muscle contraction distance was calculated using Equation (4-5) for a braid range of 20° to 40°.

For the concentric design case, if the two critical parameters (*i.e.* contraction distance and muscle force) are known, two vertical lines can be at these values vertically from the ordinates of each quadrant of Figure 6-1. A concentric design example where the required muscle contraction distance and muscle force are 7 cm and 225 N respectively is shown on Figure 6-1. The vertical lines that are intersecting the 7 cm and 225 N values will also intersect one or multiple curves for the values of n and the muscle pressure, respectively. Consequently, any horizontal line represents a possible BPM design solution. Upon selecting the number of n (*i.e.* $n = 3$) and the muscle pressure curve (*i.e.* P = 200 kPa), the vertical lines are connected with a horizontal line which will identify the required original braid diameter (*i.e.* $D_o = 1.42$). This design process results in the specification of the original braid diameter D, the number of helix turns n and the muscle operating pressure P for the required muscle force at a braid angle of 30° and the required muscle contraction distance between 20° and 40°.

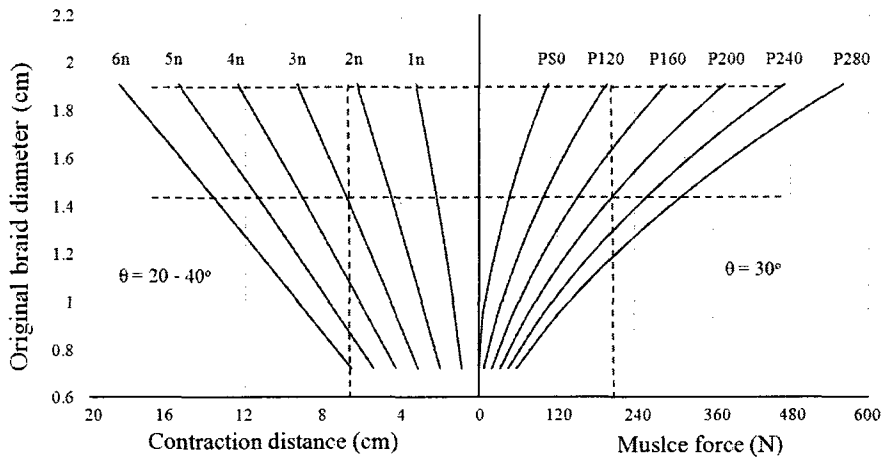

Figure 6-1: Muscle concentric contraction design chart.

The previous design step defined the muscle parameters for the required force at a nominal braid angle of 30°. The next step investigates the performance of the muscle as its length changes. Two cases for original braid diameters of 1.44 cm and 1.91 cm are shown in Figure 6-2 and Figure 6-3, respectively to demonstrate the effect of different design choices.

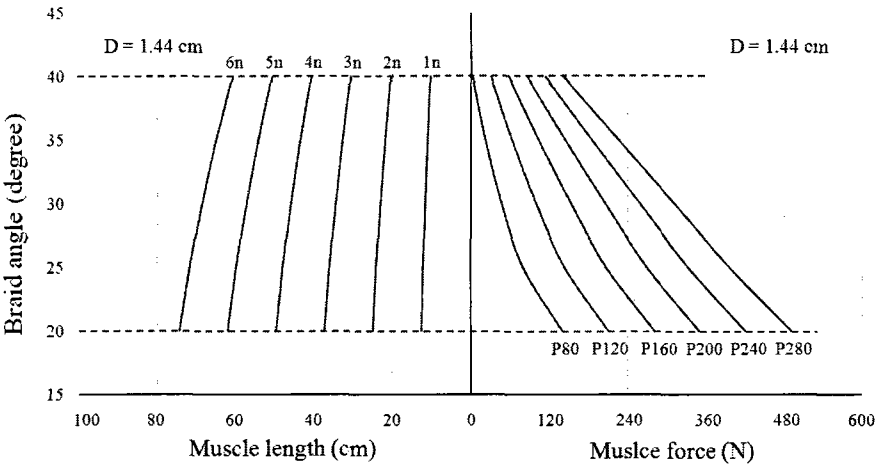

Figure 6-2: Muscle force and length as a function of the braid angle for multiple integer values of *n* and pressure. The original braid diameter is 1.44 cm.

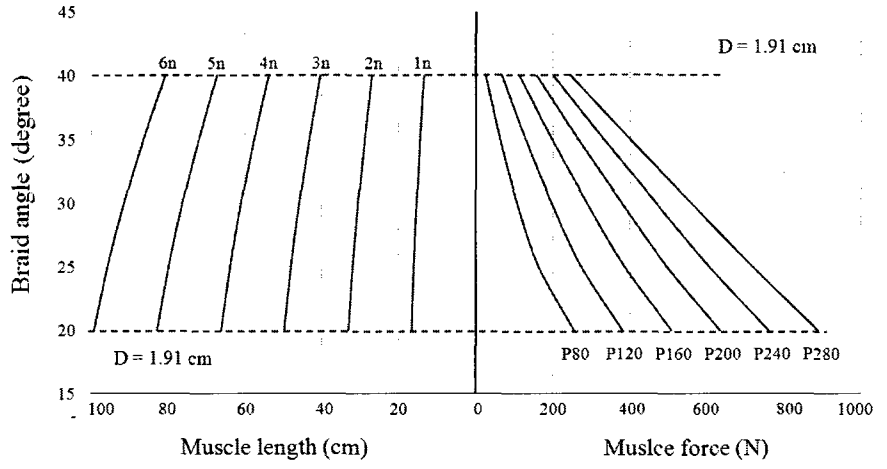

Figure 6-3: Muscle force and length as a function of the braid angle for multiple integer values of *n* and pressure. The original braid diameter is 1.91 cm.

With reference to the first quadrant of Figure 6-2, for the choice of a muscle original diameter of 1.44 cm and an operating pressure of 200 KPa, the muscle force varies between 125 N and 360

N. The second quadrant of the figure shows that for the number of helix turns $n = 3$ selected in the previous step the muscle contracts from 38 cm to 30 cm. However, if the choice was made to select an original muscle diameter of 1.91 cm, then with reference to Figure 6-3, the range of muscle force is between 280 N and 680 N and the muscle length varies between 40 cm and 50 cm. The designer would have to select the case that would best fit the intended use.

The previous design charts ignores the effect of the muscle end fixture diameter. However, muscle experiments have shown that the muscle end fixture size does affect the muscle force. To show this and to help designers predict accurately the muscle force, Figure 6-4 shows the muscle force as the end fixture diameter is varied with respect to the muscle diameter at a braid angle of 40° degrees. A braid angle of 40° is chosen since the effect of the end fixture is largest at that angle. With reference to the figure, the muscle force diminishes from 200 N to 160 N as the ratio of diameters is increased from 2 to 3.5. This reduction of force has to be taken into account during the design process.

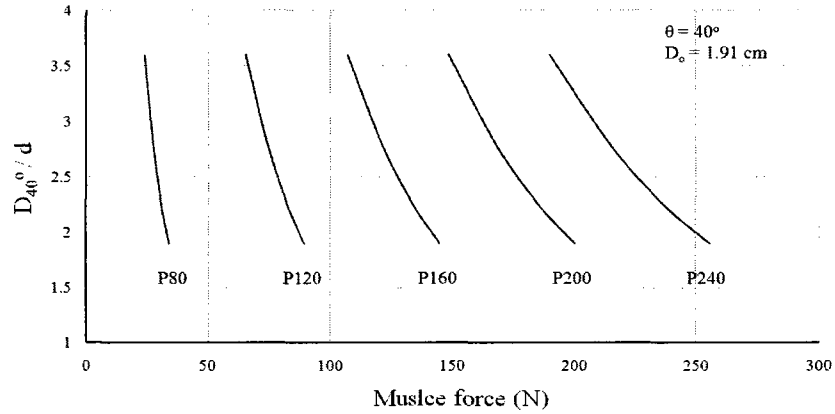

Figure 6-4: Muscle force as a function of the $D_{40}{}^{o}$ /d ratio for multiple integer values of muscle pressure. The original braid diameter and braid angle is 191 and 40 degrees, respectively.

6.2 Design Process for Isometric/Eccentric Contraction Applications

Muscle force and stiffness are the main parameters to be considered for the case of BPM design for isometric/eccentric contraction applications. For this case, the muscle operates in a passive mode where the muscle gas mass is maintained constant and the applied force changes with respect to the muscle force. Figure 6-5 shows two quadrants with different horizontal axis (*i.e.* muscle stiffness and muscle force) but for a common vertical axis, the muscle length. The right quadrant gives the muscle force as a function of the muscle length for a range of muscle original diameters (i.e. 0.72 – 1.91 cm). For these curves, the muscle force was calculated using Equation (5-16) and assuming that the muscle prototypes have $n = 2$, an initial muscle pressure of 125 kPa, and a braid angle of 35°. Similarly, the left quadrant of Figure 6-5 shows the muscle stiffness as a function of the muscle length for a range of muscle original diameter (i.e. 0.72 – 1.91 cm). For these curves, the muscle stiffness was calculated using Equation (5-45) (assuming same muscle initial condition as stated earlier). For such an application, the muscle range of motion corresponds to braid angles between 25° and 35°. This is because for the isometric/eccentric contraction the muscle is intended to operate in the middle of its operating limits.

For the isometric/eccentric design process case, if the two critical parameters (*i.e.* muscle stiffness and muscle force) are known, two vertical lines can be plotted at these values from the ordinates of each quadrant of Figure 6-5. An isometric/eccentric design example where the required muscle stiffness and muscle force are 17 kN/m and 425 N respectively is shown on Figure 6-5. The vertical lines that are intersecting the 17 kN/m and 425 N values will also intersect one or multiple curves for the values of the original diameter. Consequently, any horizontal line represents a possible BPM design solution. Upon selecting the value of the original diameter number (*i.e.* $D_o = 1.68$), the vertical lines are connected with a horizontal line which will identify the required muscle length (*i.e.* $L = 28$ cm). This design process results in the specification of the original braid diameter and the muscle length for the required muscle stiffness and muscle force.

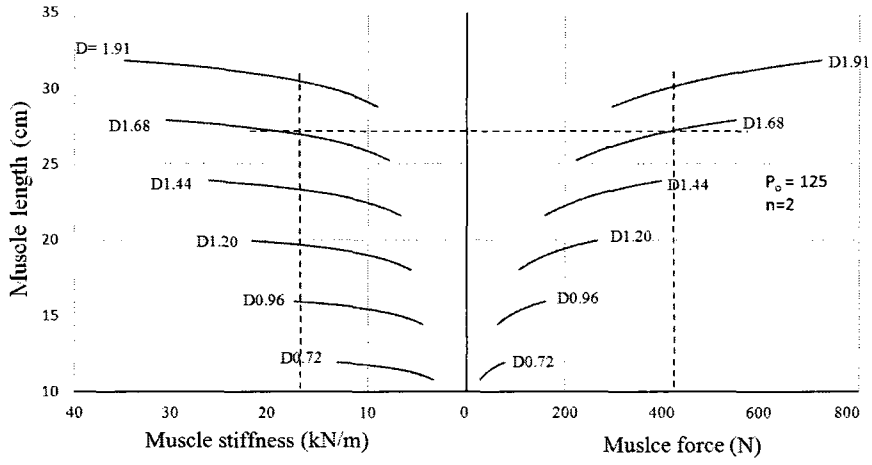

Figure 6-5: Muscle isometric/eccentric contraction design chart for n = 2.

Figure 6-5 shows that the muscle stiffness is sensitive to the original braid length since this affects greatly the relationship between the muscle volume and pressure with respect to the muscle length. The muscle pressure is not considered as a parameter in this design process since an initial pressure of 125 kPa is assumed. As the muscle is loaded the volume of the muscle decreases and its internal pressure increases. This initial muscle pressure is selected such that the muscle pressure at the braid angle of 25° does not exceed the muscle design pressure of 250 kPa.

Chapter 7

BPM DYNAMIC MODELING

The development of the Braided Pneumatic Muscle dynamic model is an important step for analyzing system characteristics, such as stability, transient response and steady state response. A dynamic model is also required for the design of a BPM controller. To date, most muscle dynamic properties are determined experimentally, and no analytical models that can predict the muscle's dynamic behaviour are found in the literature. Most analytical models are developed for the muscle force in static cases. This could be attributed to the highly challenging task of deriving such a dynamic model given the number of system elements that need to be modeled and the system's highly non-linear properties. This chapter reports on a fully analytical Newtonian-based BPM dynamic model. Results from the proposed model are compared to experimental values conducted on prototype BPM's.

7.1 Dynamic Model

The BPM dynamic model is a relationship that permits the designer to examine the muscle motion as a function of time. Several methods exist to derive such a model, however, in this chapter; a Newtonian based approach is selected. This method uses the muscle force model derived in Chapter 5. A dynamic testing setup was built in laboratory and shown schematically in Figure 7-1. This setup was designed for muscle concentric contraction tests where the mass load is constant throughout the contraction (Figure 3-2). The muscle parameters are measured and recorded by sensors and a data acquisition system, respectively.

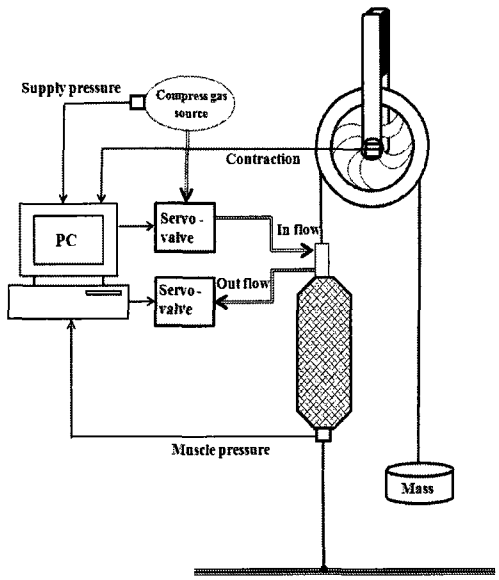

Figure 7-1: BPM dynamic testing setup.

Based on this setup, the muscle dynamic model is represented in the Laplace domain as follows:

$$\sum F_x = ms^2x \tag{7-1}$$

where F_x are the forces acting along the muscle contraction axis, m is the mass of the load and x is the muscle contraction distance. Substituting for the force components in Equation (7-1) yields:

$$NT_f \cos\theta_e \cos\beta - mg - f_{fd} = ms^2x \tag{7-2}$$

where the first term in this equation represents the force F_m produced by the muscle (5-17), the second term is the load of the mass and the third term is the dynamic friction f_{fd} resulting from the fibre to fibre contact. Solving for the muscle contraction distance yields:

$$x = \iint \left[\frac{1}{m}(F_m - mg - f_{fd})\right] dt \tag{7-3}$$

7.2 Pressure Modeling

Assuming that the muscle operating fluid is an ideal gas, the muscle pressure P_2 can be expressed as follows:

$$P_2 = \frac{M_2 R T_2}{V_2} \tag{7-4}$$

where M_2 is the mass of the muscle gas, T_2 is the temperature of the muscle gas, V_2 is the volume of muscle gas, and R is the universal constant of the muscle gas. In this case, the volume of muscle gas is determined by the proposed muscle structure (Figure 4-2) as follows:

$$V_2 = \frac{2}{3}\pi L_L \left[\left(\frac{D}{2}\right)^2 + \left(\frac{d}{2}\right)^2 + \frac{dD}{4}\right] + \pi\frac{D^2}{4}(L - 2L_L) \tag{7-5}$$

The muscle pressure is a non-linear parameter with respect to the muscle contraction distance. The muscle pressure can be linearized by introducing a small variation to each state variable around an operating point [1].

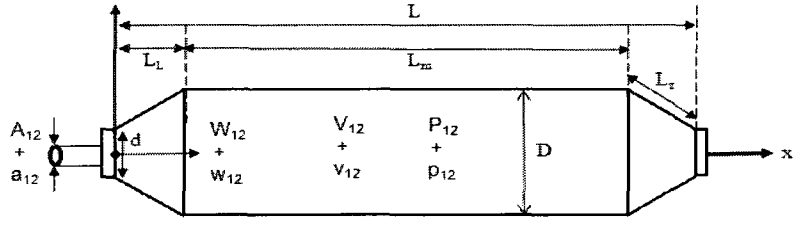

Figure 7-2: BPM structure and BPM's state elements.

In Figure 7-2, the upper-case symbols denote state variables whereas the lower-case symbols denote the variations. Taking the partial derivative of Equation (7-4), expanding the derivatives using Taylor's series, and neglecting all higher order terms, give:

$$\frac{m_2}{M_2} = \frac{p_2}{P_2} + \frac{v_2}{V_2} - \frac{t_2}{T_2} \tag{7-6}$$

Assuming a polytropic process, the muscle gas temperature is related to the muscle pressure as follows:

$$\frac{t}{T} = \frac{n_g - 1}{n_g} \frac{p}{P} \tag{7-7}$$

where the value of n_g varies between 1 for an isothermal process to 1.4 for an adiabatic process. This will cast Equation (7-6) as follows:

$$\frac{p_2}{P_2} = n_g \frac{m_2}{M_2} - n_g \frac{v_2}{V_2} \tag{7-8}$$

Dividing the variations in the parameters of Equation (7-8) by time, mapping the derivatives in Laplace domain, and rearranging gives:

$$\frac{M_2}{nP_2} sp_2 = sm_2 - \frac{M_2}{V_2} sv_2 \tag{7-9}$$

where s is the Laplace operator that denotes d/dt. The term sm_2 represents the change in mass of the muscle gas with respect to time which is also equivalent to the net mass flow rate of the muscle. In this case, we have an input and output flow and such, this relationship is given by:

$$\mathrm{sm_2} = \mathrm{W_{12}} - \mathrm{W_{23}} \tag{7-10}$$

where W_{12} is the input flow to the muscle, W_{23} is the output flow from the muscle, the index 1 denotes the supply state, the index 2 denotes the muscle state and the index 3 denotes the atmospheric state. Assuming a steady flow rate through the orifice cross section A_{12} and A_{23}, the flows W_{12} and W_{23} are given by:

$$W_{12} = \frac{KP_1A_{12}N_{12}}{\sqrt{T_1}} \quad ; \quad W_{23} = \frac{KP_2A_{23}N_{23}}{\sqrt{T_2}} \tag{7-11}$$

where T_1 and P_1 are the supply gas temperature and pressure, respectively, and K is a factor that depends on the universal gas constant R and γ. N_{12} and N_{23} are functions of the ratio of specific heats and pressure ratio across the orifice. For a detailed derivation of Equations (7-9) and (7-11), please refer to Appendix B, Section B-1.

Substituting Equation (7-10) in Equation (7-9) yields:

$$\frac{M_2}{nP_2}sp_2 = \left(\frac{KP_1A_{12}N_{12}}{\sqrt{T_1}} - \frac{KP_2A_{23}N_{23}}{\sqrt{T_2}}\right) - \frac{M_2}{V_2}sv_2 \tag{7-12}$$

Using the ideal gas equation (7-4), and rearranging the above equation yields:

$$p_2 = \int \left[\left(\frac{KP_1A_{12}N_{12}}{\sqrt{T_1}} - \frac{KP_2A_{23}N_{23}}{\sqrt{T_2}} - \frac{P_2}{RT_2}sv_2\right)\frac{nRT_2}{V_2}\right]dt \tag{7-13}$$

7.3 Valve Modeling

For operating the muscle, two proportionally controlled electro-mechanical valves (Figure 7-3) are used to control the input flow to the muscle and output flow from the muscle.

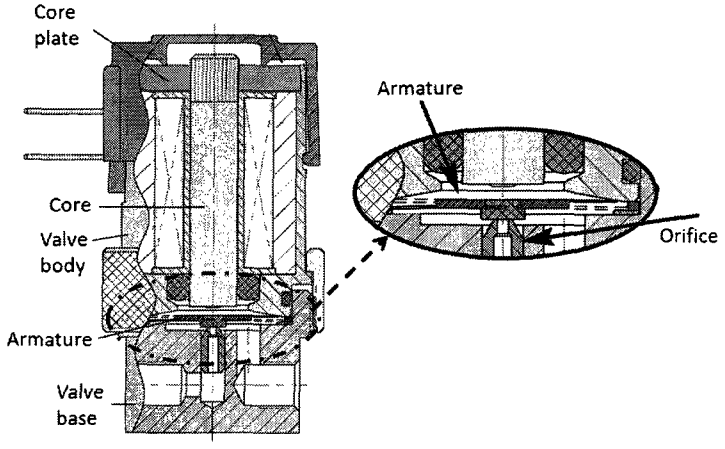

Figure 7-3: Sectional view of the EVP proportional valve by Instrument Laboratory [52]

In Figure 7-3, the moving part is the armature. As electrical current is applied to the valve's core, a magnetic force is generated that pulls on the armature. The armature will only travel if the magnetic force is greater than the force of the flat spring on the armature. For model simulation, this valve must be analytically identified. Proper valve modeling involves identifying the effective area of the valve, the derivative of the effective area of the valve with respect to the armature position, the required actuation force by the core and the derivative of this actuation force with respect to the armature position. These analytical relationships can only be achieved by dismantling the valve and completing an extensive experimental testing. This is unfeasible for this work, and thus in this case, the valve is modeled as an orifice whose effective area A_{12} and hence the flow is a function of the controller input u (electrical current).

The EPV valve series can be linearly modeled since its mechanical design offers limited hysteresis in the flow response and thus allowing for its hysteresis to be neglected (Figure 7-4).

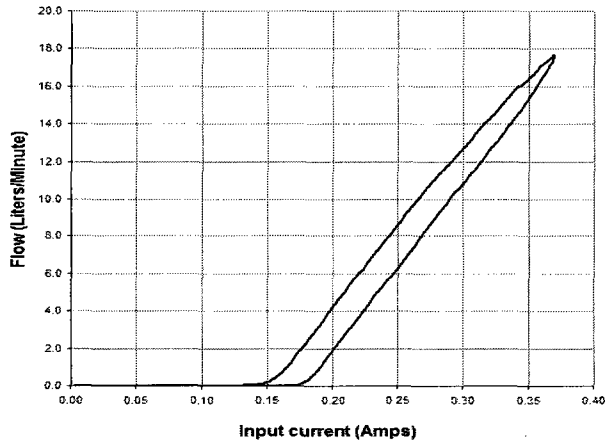

Figure 7-4: Valve gas flow vs. input current for the EC-P-05-4025 Instrument Laboratory [52]. The supply gas pressure is 344.7 kPa and the gas temperature is 23°C.

Using the experimental results in Figure 7-4, the flow rate W_{12} for the valve at a supply pressure of 344.7 kPa is approximated by a linear relationship as follows:

$$W_{12} = 0.07289 * u - 0.01056 \ \ m^3/min \tag{7-14}$$

where u is the input current in amps. Equation (7-14) cannot be used directly in the BPM modeling since in this study, different value of supply pressures were applied to the system. However, Using Equations (7-11) and (7-14), the valve opening area relationship as a function of the input current can be derived as follows:

$$A_{12} = 1.80 \times 10^{-6} * u - 2.61 \times 10^{-7} \quad m^2 \tag{7-15}$$

Equation (7-15) is derived based on a supply pressure of 344.7 kPa, however, this is greater than the average muscle operating pressure and thus it may alternate the valve properties. Therefore, the valve was calibrated in the laboratory for a range in supply pressure of approximately 30 kPa to 280 kPa (Figure 7-5).

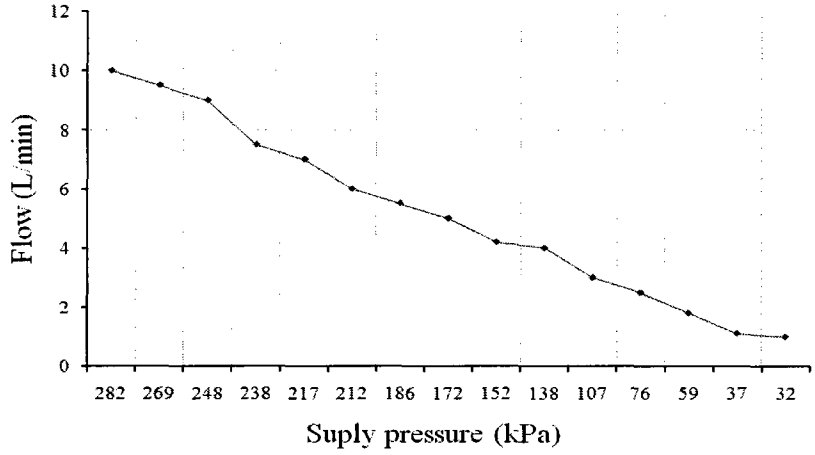

Figure 7-5: Valve gas flow vs. supply pressure for a fully open valve where the input current is approximately 0.35 Amp.

Based on the experimental results in Figure 7-5 and Equation (7-11), a valve effective area has been calculated for each supply pressure test (Table A-7). Figure 7-4 and Figure 7-5 show the flow rate through the valve as a function of the input current and the supply pressure. In both cases, the valve back pressure was atmospheric. This is never the case for the input flow W_{12} to the muscle, since its back pressure is the actual muscle pressure which is rarely atmospheric. Thus, the valve back pressure effect on the valve is not considered in these results and relationships.

To further characterize the valve behaviour including its back pressure, a physical setup was designed such to record the required time for a fully open valve to inflate a specific tank volume to a specific pressure and then to deflated back to atmospheric pressure . In this test, the supply pressure and the tank pressure were measured using a pressure transducer while being recorded as a function of time using a data acquisition system. This test was repeated for eight tank volumes of 2.1 L, 1.85, 1.6 L, 1.35 L, 1.1 L, 0.85 L, 0.6 L and 0.35 L as well as for two supply pressures of 207 kPa and 138 kPa. These experimental results are shown in Figure 7-6 and Figure 7-7.

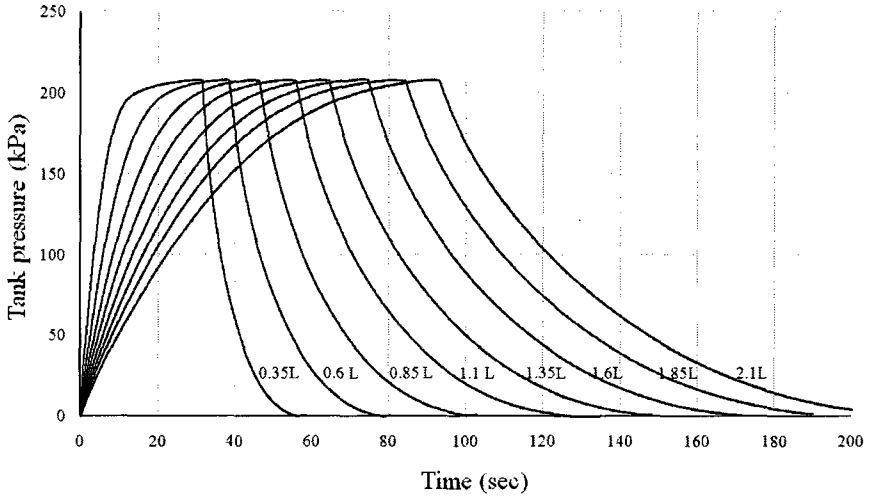

Figure 7-6: Tank pressure vs. time for eight distinct tank volumes. In this test, the supply pressure and the input current to the valve are 207 kPa and 0.35 Amp, respectively.

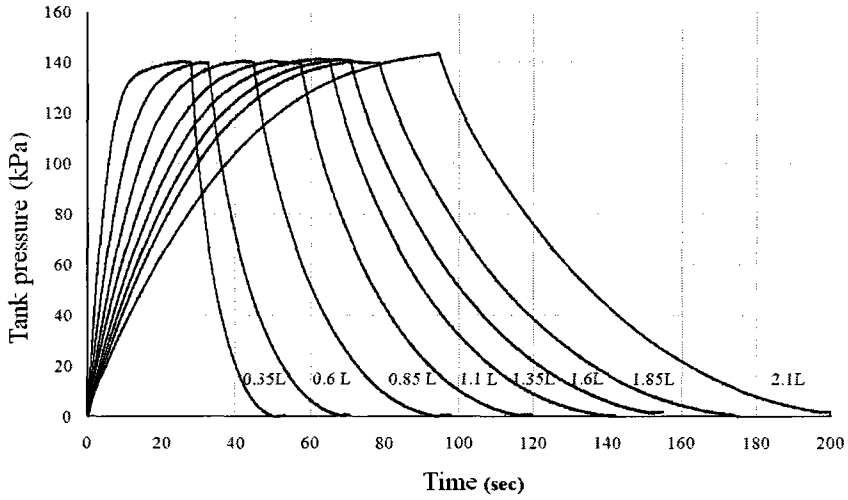

Figure 7-7: Tank pressure vs. time for eight distinct tank volumes. In this test, the supply pressure and the input current to the valve are 138 kPa and 0.35 Amp, respectively.

Using the experimental results in Figure 7-6 and Figure 7-7, a parametric model for the valve has been developed (Appendix D, Figure D-1). This has resulted in an effective area of the valve of 0.002580 cm^2 when the input current of the valve is 0.35 Amp. This is approximately 32 % reduction in the effective area of the valve when compared to Equation (7-15). Finally, to validate the valve characterization in this study, a model was developed to simulate the pressure vs. time behaviour for a constant tank volume inflation and deflation as experimentally done in Figure 7-6 and Figure 7-7. Assuming an ideal gas and a polytropic process, the tank pressure P_t relationship was derived similarly to Equation (7-9); however, with a constant volume as follows:

$$\frac{M_t}{nP_t} sp_t = sm_t \tag{7-16}$$

where M_t is the mass of the tank gas and sm_t is the change in mass of the tank gas with respect to time which is also equivalent to the net flow rate to the tank W_t. this flow rate relationship is given by:

$$W_t = W_{12} - W_{23} = \frac{KP_1A_{12}N_{12}}{\sqrt{T_1}} - \frac{KP_2A_{23}N_{23}}{\sqrt{T_2}} \tag{7-17}$$

In this equation, the index 1 denotes the supply state, the index 2 denotes the tank state and the index 3 denotes the atmospheric state. Substituting Equation (7-17) in Equation (7-16) and rearranging yield:

$$p_t = \int \left[\left(\frac{KP_1A_{12}N_{12}}{\sqrt{T_1}} - \frac{KP_2A_{23}N_{23}}{\sqrt{T_2}} \right) * \frac{nP_t}{M_t} \right] dt \tag{7-18}$$

Using the ideal gas equation (7-4), the above equation yields:

$$p_t = \int \left[\left(\frac{KP_1A_{12}N_{12}}{\sqrt{T_1}} - \frac{KP_2A_{23}N_{23}}{\sqrt{T_2}} \right) * \frac{nRT_2}{V_2} \right] dt \tag{7-19}$$

where M_t is the mass of the tank gas, T_t is the temperature of the tank gas and V_t is the volume of tank gas. The temperature T_t is determined using the polytropic process relationship given by Equation (7-7). A diagram and a MATLAB Simulink program for this model are shown in Figure 7-8 and Figure A, respectively.

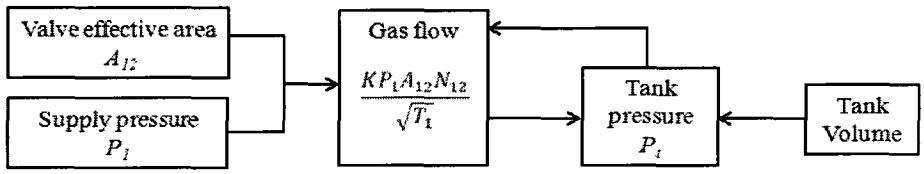

Figure 7-8: Model diagram for the valve with a constant tank volume

The proposed model for the valve and a constant volume given by Equation (7-19) has been successfully validated by predicting the experimental results of the tank pressure vs. time for eight distinct volumes and two supply pressures. Therefore, this model which includes the valve characterization will be used later on for developing the BPM dynamic model. For a supply pressure of 208 kPa, the model results and the experimental results for a tank volume of 2.1 L (largest volume) and 0.35 L (smallest volume) are shown in Figure 7-9 and Figure 7-10, respectively. Also, Figure 7-11 shows the model validation for a tank volume of 0.35 L and a supply pressure of 138 kPa. Based on the model validation results for the 16 tests, it was shown that the model and the experimental results are in a good agreement. Therefore, this model will be used to predict the muscle pressure in the dynamic model.

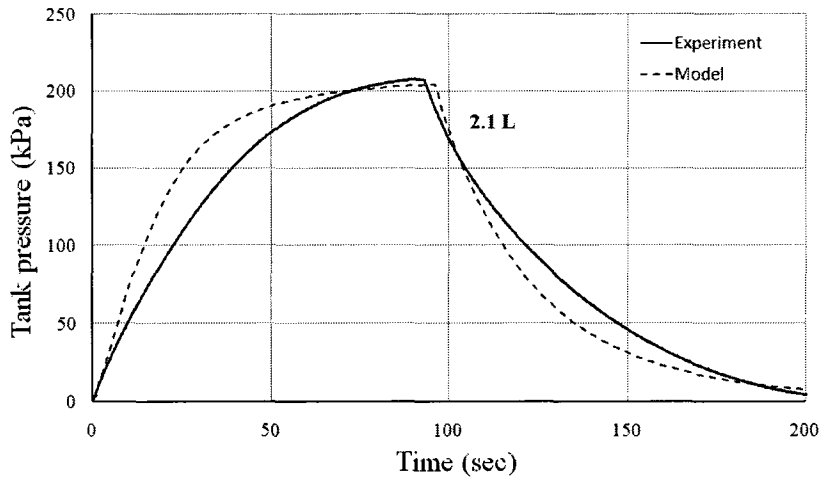

Figure 7-9: Valve and constant volume model validation results for a tank volume of 2.1 L and a supply pressure of 207 kPa.

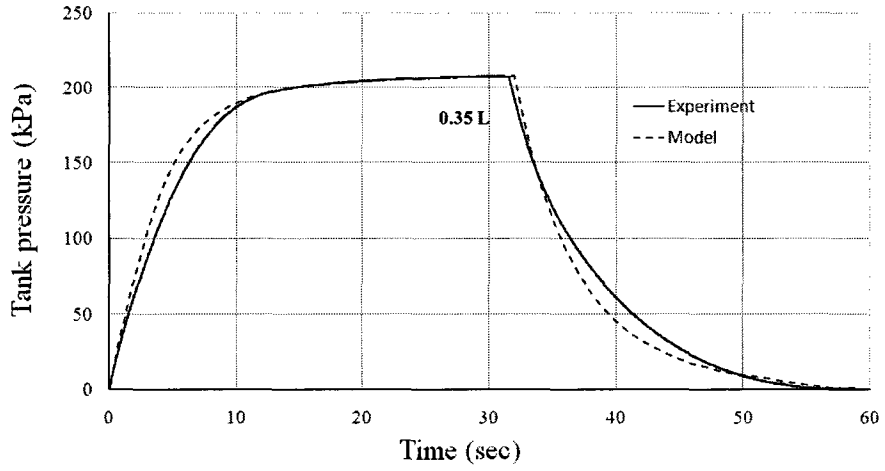

Figure 7-10: Valve and constant volume model validation results for a tank volume of 0.35 L and a supply pressure of 207 kPa.

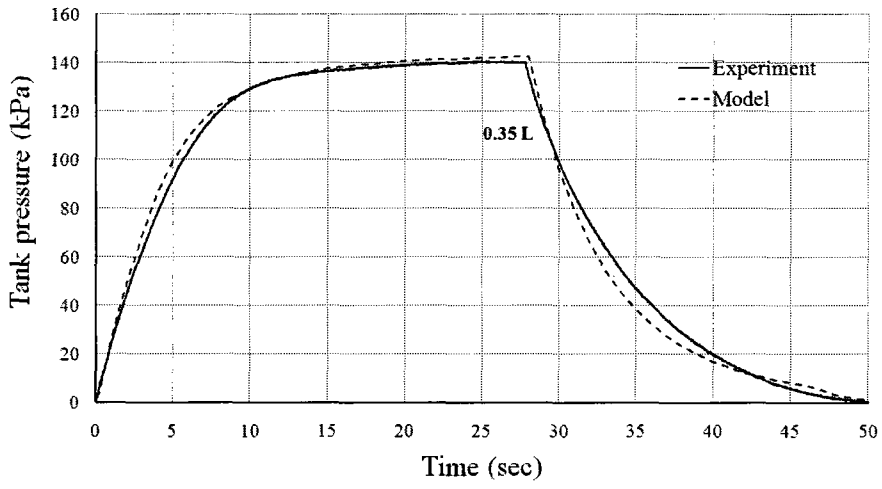

Figure 7-11: Valve and constant volume model validation results for a tank volume of 0.35 L and a supply pressure of 138 kPa.

7.4 Dynamic Friction Modeling

In this work the frictional force is assumed to be the result of braid fibre-fibre contact only. Furthermore, the undulations due to the cross fibre weave are ignored, and cross fibres are assumed to simply lie on top of each other. The complete muscle frictional force expression was given in Equation (5-26). Such a form, however, is highly nonlinear and includes a discontinuity at the transition from the static friction regime to the dynamic one. Such discontinuities are difficult to deal with in numerical simulation. Consequently, for the dynamic case, Equation (5-26) is replaced by:

$$f_{frd} = PA_{ff}\mu_{dL} \tag{7-20}$$

$$\mu_{dL} = \mu_d Tanh(K_f v) \tag{7-21}$$

where f_{frd} is the dynamic frictional force, μ_{dL} is the new dynamic friction coefficient, k_f is a constant that defines how close Equation (7-20) approximates the Coulomb friction (Figure 7-12) and v is the BPM contraction velocity [53].

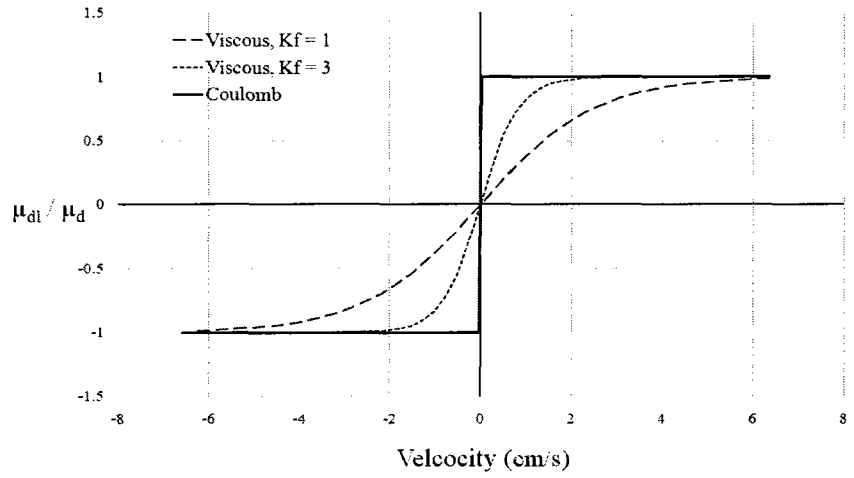

Figure 7-12: Coulomb and viscous friction coefficient as a function of muscle contraction velocity

7.5 BPM Dynamic Model Simulation

To simulate the BPM dynamic model, a block diagram approach is used in this study. Figure 7-13 shows the inter-relationships between the muscle analytical equations and the parameters used for the BPM model simulation. This figure is a simplified presentation of the MATLAB/Simulink model used (Appendix D, Figure D-2). This model is comprehensive and the simulation takes into account the exact values of all the parameters corresponding to experiments with the exception of three values, namely, the exact nature of the polytropic process of inflating and deflating the muscle, the exact model for the frictional losses, and the dynamics of a pneumatic valve and the air flow through it.

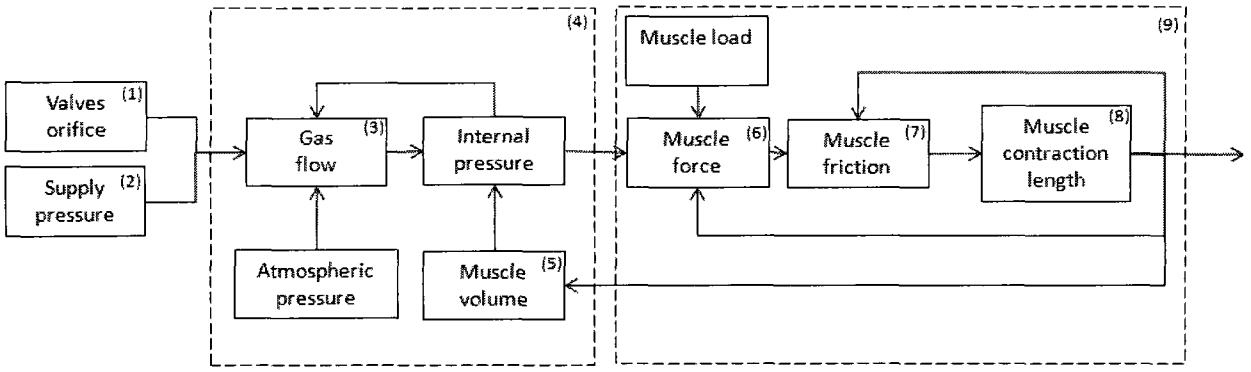

Figure 7-13: BPM dynamic model block diagram.

With reference to Figure 7-13, the valves orifice effective areas (# 1 and #2) were determined from the experimentally validated model in Section 6.3. Next, the muscle state pressure (#4) is determined using Equation (7-13) which is a function of the muscle net flow (#3) Equation (7-10), the ideal gas Equation (7-4), and the actual muscle volume (#5) Equation (7-5) as follows:

$$p_2 = \int \left[\left(\frac{KP_1A_{12}N_{12}}{\sqrt{T_1}} - \frac{KP_2A_{23}N_{23}}{\sqrt{T_2}} - \frac{P_2}{RT_2} sv_2 \right) \frac{nRT_2}{V_2} \right] dt$$

Next, the muscle force F_m (#6) is determined by Equation (5-15) which is a function of the muscle pressure and the muscle contraction distance as follows:

$$F_m = NT_f cos\beta * cos\theta_e$$

The muscle contraction distance (#8) is determined using Equation (7-3) which is a function of the net muscle force, hanging load and the muscle dynamic friction as follows:

$$x = \iint \left[\frac{1}{m} (F_m - mg - f_{fd}) \right] dt$$

The muscle dynamic friction (#7) is determined using Equation (7-20) which is a function the muscle pressure and the fibre to fibre contact area as follows:

$$f_{frd} = PA_{ff}\mu_{dL}$$

This muscle dynamic model is for a system analogous to a mechanical system that consists of a force element F_e, variable stiffness spring constant K, variable friction force F_{fr}, and an inertia term. This will cast Equation (7-2) as follows:

$$s^2x = \frac{1}{m}[Kx - mg - F_{frd}] \tag{7-22}$$

where

$$\mathrm{K} = \frac{NT_f \cos\theta_e \cos\beta}{\mathrm{x}}$$

Such a system is schematically shown in Figure 7-14.

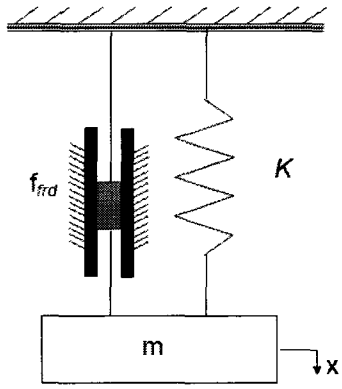

Figure 7-14: Muscle dynamic model shown as a mechanical network.

7.6 Dynamic Model Validation

Comparisons of the experimental and theoretical simulation results for three muscle configurations are shown in the following figures. The three muscles have an original braid diameter of 1.9 cm and an end muscle diameter of 1.3 cm. The short muscle configuration has one fibre revolution (n = 1) in an original braid length of 17 cm, the average muscle configuration has two fibre revolutions (n = 2) in an original braid length of 34 cm while the long configuration has three fibre revolutions (n = 3) in an original braid length of 51 cm long.

Figure 7-15 and Figure 7-16 compare the experimental muscle contraction distance and the muscle pressure curves of the one fibre revolution (n = 1) muscle with the theoretical ones for the isentropic case for the three different friction assumptions portrayed in Figure 7-12. Figure 7-15 and Figure 7-16 show that most model curves reached a similar steady state response with an accuracy of approximately 2 % error in the muscle contraction distance when compared to the experimental results. All three theoretical curves and the experimental results for the muscle contraction distance (Figure 7-15) exhibit similar behaviour (*i.e.* a damped response) but to varying degrees. This is attributed to the high muscle force magnitude as the muscle pressure increases. Distinctively, the muscle contraction distance for the model with Coulomb friction experienced a steady state error that is approximately 5 % of the muscle contraction distance. This could be attributed to Coulomb friction force magnitude being greater than to the others for the tested contraction speed range. In all three cases, the model curves experience a discrepancy in transient response. All model curves have a faster output response than the experimental results in the muscle contraction and the expansion phase. For the muscle contraction distance model results, this can be primarily due to ignoring the undulation in crossing fibres as they weave over and under each other. This effect may cause an underestimation of the damping in the system, consequently leading to a fast transient system response as shown in Figure 7-15. With respect to the muscle pressure model results (Figure 7-16), all three model curves are essentially identical but are all not exactly matching the experimental results. Many factors can contribute to this discrepancy in transient response. This includes the accuracy of the valve characterization, the accuracy of the linearized muscle pressure model for large volume change and the exact nature of the polytropic process.

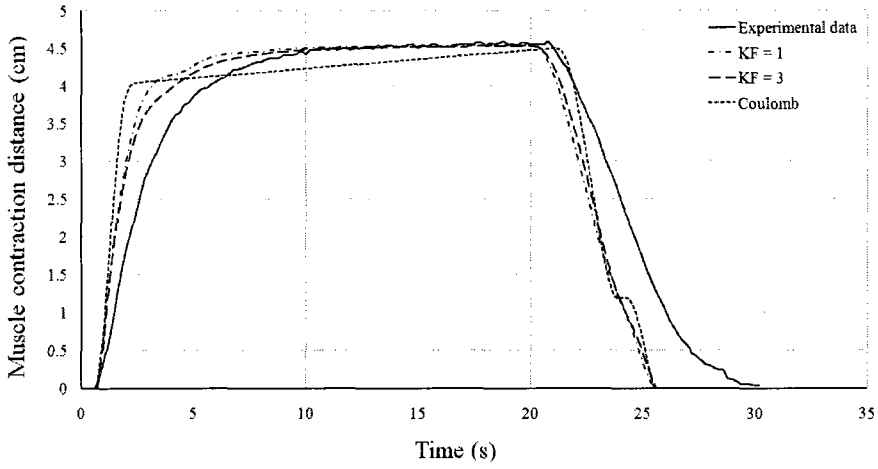

Figure 7-15: Muscle contraction distance validation results for n1_D1.9 prototype when the friction is modeled as viscous and coulomb types.

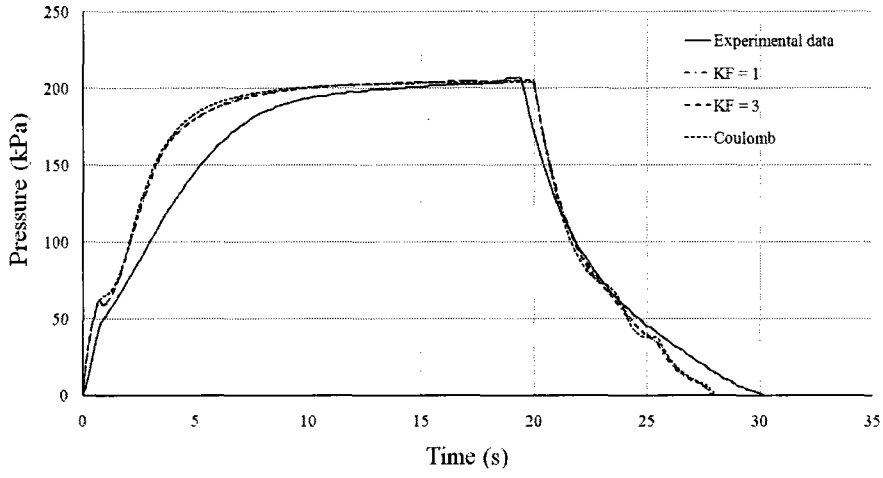

Figure 7-16: Muscle pressure validation results for n1_D1.9 prototype when the friction is modeled as viscous and coulomb types.

A comparison between the experimental muscle contraction distance and the muscle pressure for the case of n = 3, the theoretical model with three different polytropic processes (n_g =1.4, 1.3, and 1) are shown in Figure 7-17 and Figure 7-18. The K_f = 3 friction model is used for these plots. These figures show that the polytropic index n_g has a marked effect on the transient and steady state responses of the model on this volume of muscle. For n_g = 1.4 and 1.3, the model curves are comparable to each others; however, for n_g = 1, the model value diverge from the other values and never reaches the supply pressure value at steady state.

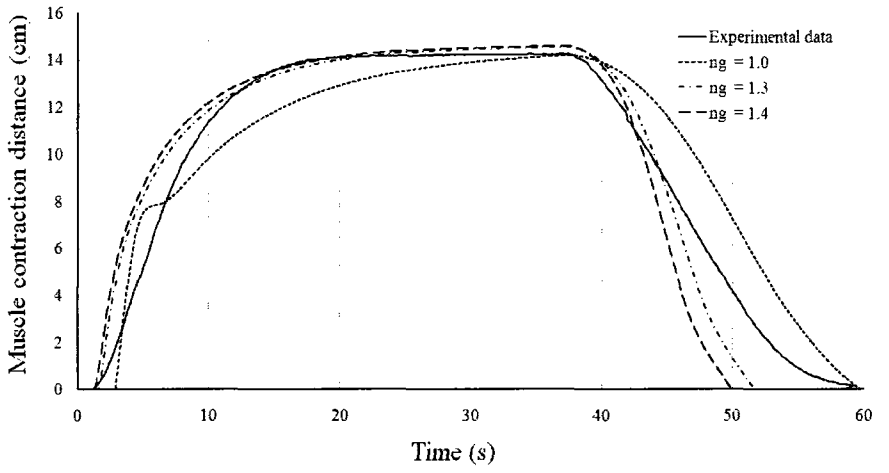

Figure 7-17: Muscle contraction distance validation results for n3_D1.9 prototype for three different polytropic process coefficients; isentropic (n_g =1.4), polytropic with n_g=1.3, and isothermal (n_g=1). In this test, the friction is modeled as viscous with K_f = 1.

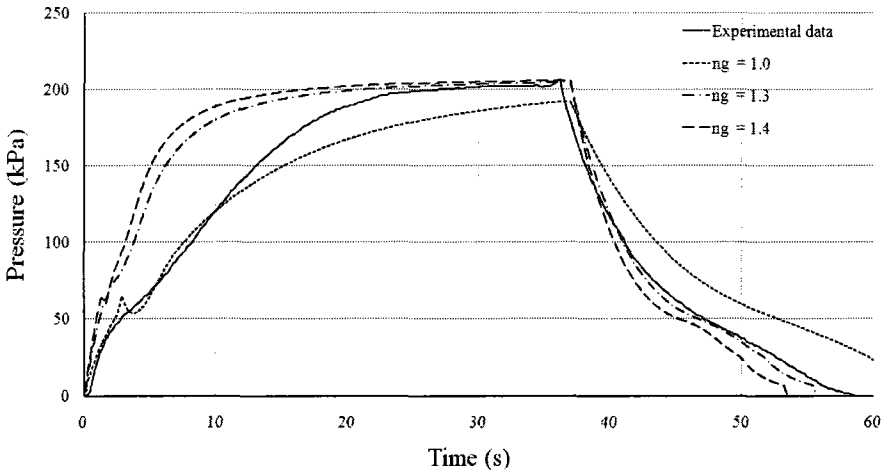

Figure 7-18: Muscle pressure validation results for n3_D1.9 prototype for three different polytropic process coefficients; isentropic (n_g =1.4), polytropic with n_g=1.3, and isothermal (n_g=1).

Finally, the BPM dynamic model is tested and validated for the two fibre revolutions (n = 2) muscle for the isentropic case n_g =1.3 and the friction model k_f = 3. The theoretical model curve agrees approximately within 2 % of the experimental steady state results. The model discrepancy

in the transient response phase (Figure 7-19 and Figure 7-20) is attributed to the same the factors that was elaborated on for n = 1.

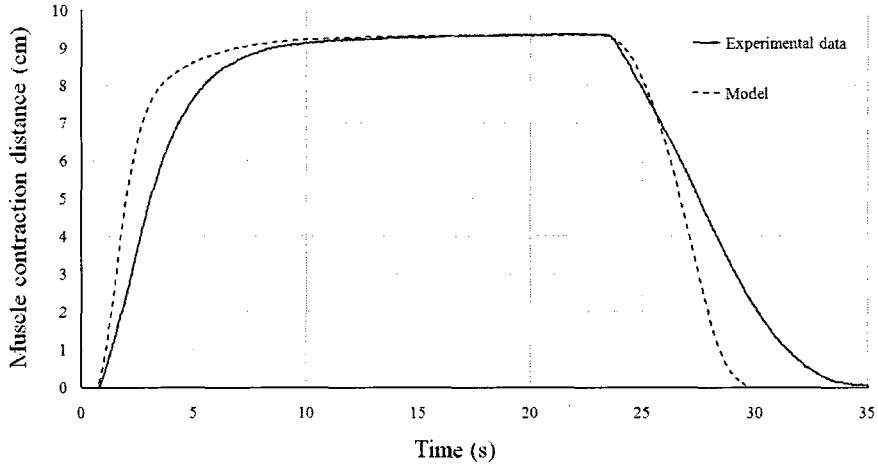

Figure 7-19: Muscle contraction distance validation results for n2_D1.9 prototype when the friction is modeled as viscous and coulomb types.

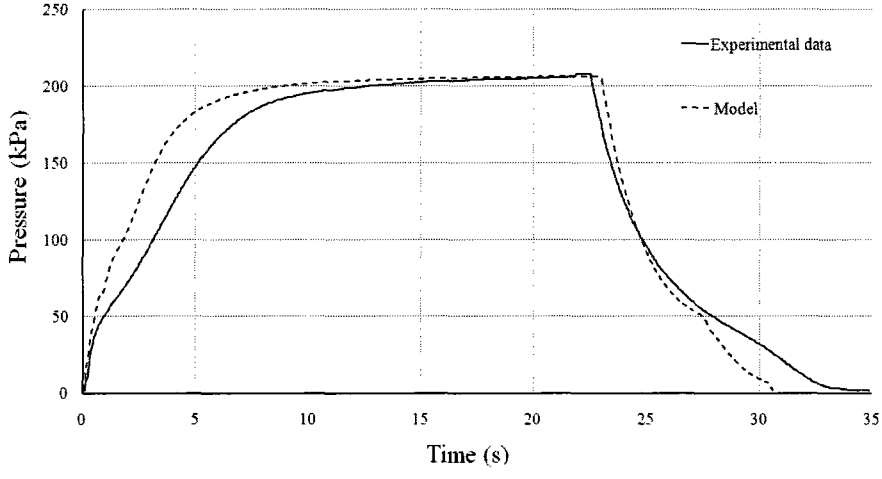

Figure 7-20: Muscle pressure validation results for n2_D1.9 prototype when the friction is modeled as viscous and coulomb types.

Chapter 8

BPM System Identification

The analytical model derived in Chapter 6 can predict accurately the BPM steady state response, however, its accuracy for predicting the BPM dynamic behaviour, or more specifically, the BPM transient response is limited. The model can be enhanced by improving the muscle modeling elements; however, this can be unfeasible for this work (e.g. valve modeling). Therefore, an alternative modeling approach which relies on system identification techniques based on observable system input and output parameters is used. In this chapter, linear and non-linear system identification techniques are introduced and later implemented in developing a model or an emulator that successfully predicts the BPM dynamic behaviour. Many linear and non-linear system identification models exist, however, since the BPM is a non-linear dynamic system with few observable parameters, the general stochastic model of Auto Regressive with Exogenous Input, the Neural Network Auto Regressive with Exogenous Input and the Neural Network Output Error are implemented. For these models, two algorithms were used to obtain the optimized model parameters (Gradient Descent and Conjugate Gradient algorithm).

8.1 System Model

System Identification (SI) is used to develop a model that is capable of simulating the behaviour of a system given a finite number of observable system parameters. In this chapter, a BPM dynamic model is obtained given the collected data from the BPM dynamic experiments. For this task, a four step process is used (Figure 8-1), namely, the system model selection, the experimental setup, the parameter estimation, and the model validation. This process was developed based on concepts presented in [54].

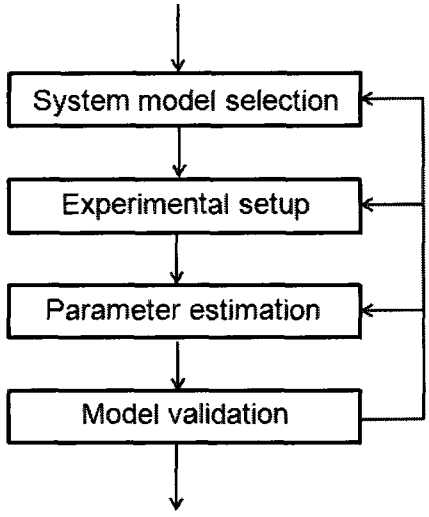

Figure 8-1: System Identification procedure.

The selection of the system model is an important initial step. This was based on the BPM experimental evaluation (Chapter 3) and the understanding of the system model. The performance of the system model is difficult to predict, however, it was important to ensure that the model is compatible with the BPM system. The experimental setups were designed and built to collect the selected inputs and outputs variables for the system model. The selected variables were based on their feasibility for measurement and subsequent control. Ideally, all observable BPM input and output should be used, however, such a scenario may overwhelm the system model by increasing the complexity of the optimization problem. The observable inputs are the supply pressure, the muscle pressure, the valve opening orifice area, and the hanging mass. The

observable output was the muscle contraction distance. The experimental setups were designed to cover the full range of muscle operation under various excitation signals (*e.g.* supply pressures). The parameter estimation step determines the optimum values for the for the system model parameters. Many methods exist; however, few are capable of solving an optimization problem for a dynamic model involving non-linearities. Moreover, depending on the selected system model in step 1, the number of optimization algorithms may be limited. Finally, the developed system model is tested for the design criteria. The validation criterion is the BPM system model output accuracy. The validation data set used for testing was obtained from second set of experiments.

8.2 Linear System Model

Linear models are the first choice regardless of the linearity of the BPM system. Over the past several decades, linear models theory has been well studied and analyzed (*e.g.* [54], [55], [56], [57], [58] and [59]). Using time series models, the BPM output *y(k)* which includes the deterministic and the stochastic parts can be modeled as a general linear model structure as follows:

$$y(k) = \frac{B(q)}{A(q)}u(k) + \frac{C(q)}{D(q)}v(k) \tag{8-1}$$

where *u(k)* is the muscle input, v(k) is a zero-mean white noise, *B(q)*, *A(q)*, *C(q)* and *D(q)* are polynomials. If the muscle input is not observable, Equation (8-1) yields a stochastic output. Some of the general stochastic model structures are the Auto Regressive (AR), the Moving Average (MA) and the Auto Regressive Moving Average (ARMA). These models assume that the disturbance drives the BPM system, however, this operating case is not considered in this work. The muscle system model is more meaningful and accurate if the muscle input *u(k)* is observable and accounted for. The most common model structures with an exogenous input are namely, the Auto Regressive with Exogenous Input (ARX), the Auto Regressive Moving Average with Exogenous Input (ARMAX) and the Output Error (OE) model. Mathematically, these models are expressed as follows:

$$ARX: \quad y(k) = \frac{B(q)}{A(q)}u(k) + \frac{1}{A(q)}v(k) \tag{8-2}$$

$$ARMAX: \quad y(k) = \frac{B(q)}{A(q)}u(k) + \frac{C(q)}{D(q)}v(k) \tag{8-3}$$

$$OE: \quad y(k) = \frac{B(q)}{F(q)}u(k) + v(k) \tag{8-4}$$

The ARX model is the most common linear system model. This is due to its simple implementation and the common usage of the linear Least Squares (LS) algorithm for obtaining the model parameters. The disadvantage of the ARX model is that it includes the disturbance as part of the BPM system dynamics. This causes problems if the disturbance is not a zero-mean white noise. The OE model is another common model. For this model, the BPM disturbance is used as an output disturbance of the system. Similarly to ARMAX model, the OE model is non-linear and, therefore, non-linear optimization techniques must be used [59] .

8.3 Nonlinear System Identification

Unlike linear systems, the non-linear system theories are less studied and analyzed. For this research, Neural Network (NN) based methods were selected to emulate the BPM dynamic behaviour (NN and its implementation process are introduced in Appendix C). Other non-linear SI methods exist such as classical polynomial based and fuzzy based models. Throughout the years, the NN method has been successfully used by many researchers to identify models [60] [61]. It has been shown to be a very powerful tool for mapping system inputs to its outputs [62]. This makes the NN a strong candidate for the BPM static model, however, for the dynamic model, the NN performance is hard to predict. Its success depends on numerous factors, but mainly on the selected system model. For this research, two types of NN were implemented and analyzed, namely, the Feed Forward Multiple Layer Perceptron (MLP) and the Recurrent Neural Network (RNN). The MLP and the RNN are known as the static and the dynamic NN methods, respectively. This is further elaborated on in Appendix C.

For the MLP, the Neural Network Auto Regressive with Exogenous Input model (NNARX) was selected for the BPM system model (Figure 8-2). This system model can emulate a multiple input multiple output system as the BPM. Moreover, the NNARX is capable of learning the BPM dynamic behaviour since its output is a function of previous system inputs and outputs. The NNARX model can be defined as a function of the observable past inputs *u(k)* and outputs *y(k)* as follows:

$$y(k) = f[u(k), u(k-1), \ldots, u(k-m), y(k-1) \ldots y(k-m)] \tag{8-5}$$

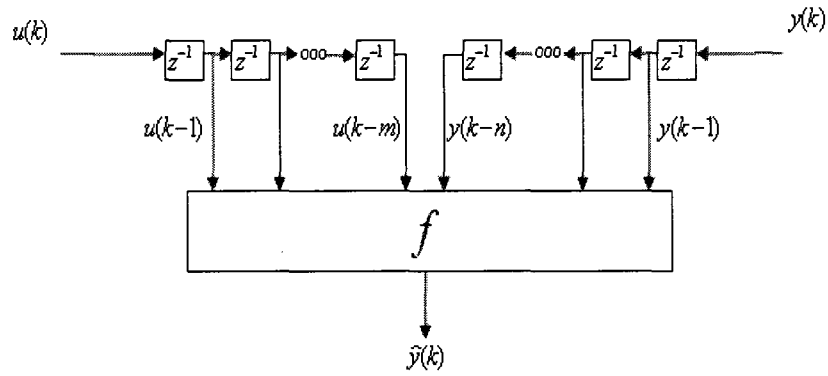

Figure 8-2: NNARX model structure [57].

With reference to Figure 8-2, z^{-1} is a single time delay and $\hat{y}(k)$ is the NN method predicted output. The NNARX model is an MLP Network with a finite number of tapped inputs and outputs. The number of the tapped inputs and outputs represents the SI model order. This model is considered a closed loop control system since the error *e(k)* is fed back to the network (Figure 8-3). Such a criterion allows the network to learn as the system is operating. The NNARX network is less desirable to use for a dynamic system since it requires a high number of tapped delays where this tend to increase the convergence time of the NN method solution.

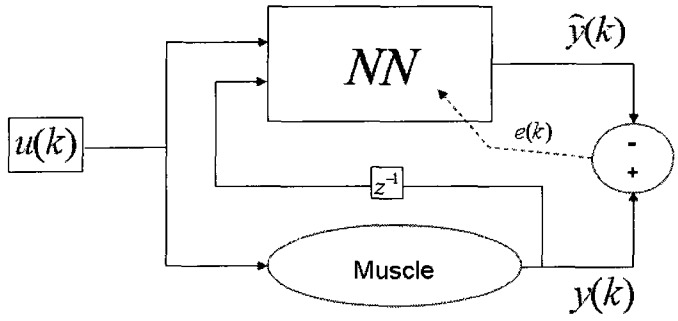

Figure 8-3: NNARX model structure.

For the RNN, the Neural Network Output Error model (NNOE) is selected. The output of this model depends on all past NN output values and thus makes the network dynamically driven. This property allows the NNOE to learn the BPM dynamic behaviours. The NNOE is also a closed loop control system [54].

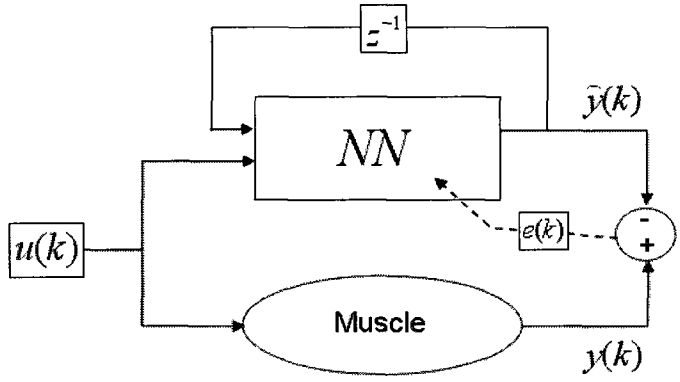

Figure 8-4: NNOE system identification model running online with the BPM.

8.4 Optimization Algorithms

For the linear system model case, the Least Squares (LS) algorithm was used to obtain the model parameters. The LS algorithm solution is given as follows:

$$\hat{\theta} = \left[\frac{1}{N}\sum_{1}^{k}\phi\phi^{T}\right]^{-1}\left[\frac{1}{N}\sum\phi y\right] \tag{8-6}$$

where $\hat{\theta}$ is the solution parameters vector, ϕ is the regression vector and y is the output vector. For a detailed derivation of LS algorithm, please refer to Appendix B, Section B-2.

For the non-linear system model case, the Back-propagation algorithm was used; this approach uses the Gradient Descent technique with error Back-propagation to optimize the network. The Gradient Descent technique assures that the network weight values converge in the negative direction of the cost function gradient. The error of the network is determined for the output layer j, and consequently fed back to the network for weight adjustment. The weight modification relationship w_{kj} for this algorithm is:

$$\Delta w_{kj}(n) = \lambda\delta_j y_k + \eta\Delta w_{kj}(n-1) \tag{8-7}$$

where λ is the learning rate constant, η is the momentum constant. For an output layer j, the error term δ is:

$$\delta_j = (t_j - y_j)y_j(1-y_j) \tag{8-8}$$

For a hidden layer j, the error term δ corresponds to:

$$\delta_j = \left(\sum\delta_i w_{ji}\right)y_j(1-y_j) \tag{8-9}$$

The error term for the hidden layer requires the error term of the output layer and therefore the weight modification starts from the output layers and propagates backward. The algorithm progresses interactively through a number of epochs. For detail derivation of the Back-propagation algorithm, please refer to Appendix C, section C-4.

As previously mentioned, the Back-propagation algorithm modifies the network weights using the Gradient Descent technique. In most cases, the Gradient Descent does not lead to the fastest NN solution. The speed of this process is important if the SI process is implemented online. To improve the NN convergence time, a powerful algorithm, namely, the Conjugate Gradient algorithm of Fletcher – Reeves [63] is implemented. This algorithm initializes the optimizations process by evaluating the gradient of the cost function to obtain the first search direction but then

redirects the search along conjugate direction. Thereof achieving consecutive conjugate direction steps assures a quadratic convergence, in other words, this method is capable of determining a function solution within a finite number of iterations. The search direction S_i for the Fletcher - Reeves algorithm is given by:

$$S_i = -\nabla f_i + \frac{|\nabla f_i|^2}{|\nabla f_{i-1}|^2} S_{i-1} \tag{8-10}$$

where ∇f_i is the gradient function. The network weights w converge as follows:

$$\Delta w_{kj} = \lambda S_i \tag{8-11}$$

where S_i is given by:

$$S_i = -\left(\frac{\partial E}{\partial w_{kj}}\right)_i + \frac{\left|\left(\frac{\partial E}{\partial w_{kj}}\right)_i\right|^2}{\left|\left(\frac{\partial E}{\partial w_{kj}}\right)_{i-1}\right|^2} S_{i-1} \tag{8-12}$$

where E is the network error function. The partial derivative of the error function with respect to the network weight is determined for the output layer and hidden layer using the Back-propagation technique. Substituting the Fletcher - Reeves direction S_i into Equation (8-11) yields to:

$$\Delta w_{kj} = \lambda\left(-\nabla f_i + \frac{|\nabla f_i|^2}{|\nabla f_{i-1}|^2} S_{i-1}\right) \tag{8-13}$$

where

$$\nabla f_i = \left(\frac{\partial E}{\partial w_{kj}}\right)_i$$

And the second term in the bracket is known as the momentum term η. The Conjugate Gradient Method is similar to the Steepest Descent algorithm except that this method converges to the optimum solution using an adjustable training rate λ and a momentum term η that is dependent on previous search directions. The weight modification relationship for this algorithm is:

$$w_{kj}(n+1) = w_{kj}(n) + \lambda_i S_i \tag{8-14}$$

where λ_i is the optimum step length. This step value is determined using any single variable minimization method (*e.g.* quadratic interpolation method [63]). For detail derivation of the Conjugate Gradient method, please refer to Appendix C, Section C-4.

8.5 Experimental Testing and Validation

The experimental testing and validation section is composed of two parts, namely, the linear model and the Neural Network models. In both cases, results from the developed models are compared to experimental ones obtained from prototype BPMs.

8.5.1 Linear Model

The BPM is ideally represented by a multiple inputs and multiple outputs system; however, the linear models analyzed earlier are only feasible for a single input and single output system. This implies that some of the muscle parameters must be assumed constant, namely, the hanging mass, the supply pressure and the valve area opening. The chosen BPM input and output are the muscle pressure and the muscle contraction distance, respectively.

The ARX model given in Equation (8-2) was first implemented to predict the BPM dynamic behaviour. For a system of order *n*, the ARX model is given as follows:

$$y(k) = \underbrace{a_1 y(k-n) + a_2 y(k-n-1) + \cdots + a_n y(k-1)}_{\text{Autoregressive}} + \underbrace{b_1 u(k-n) + b_2 u(k-n-1) + \cdots + b_n u(k-1)}_{\text{Exogenous}} + \underbrace{d_1 v(k-n) + \cdots}_{\text{Noise}}$$

Figure 8-5: Expanded analytical form of ARX model with n order.

Assuming that the BPM is a second order system and that the system noise *v* is uncorrelated, the ARX model simplifies to:

$$y(k) = a_1 y(k-2) + a_2 y(k-1) + + b_1 u(k-2) + b_2 u(k-1) \quad (8\text{-}15)$$

Using the collected experimental data and the LS algorithm solution (Appendix B, Section B-2), a MATLAB program was written to obtain the solution parameters for identifying the BPM model (Appendix D, Section D-2). The validation results for the ARX model are shown in Figure 8-6.

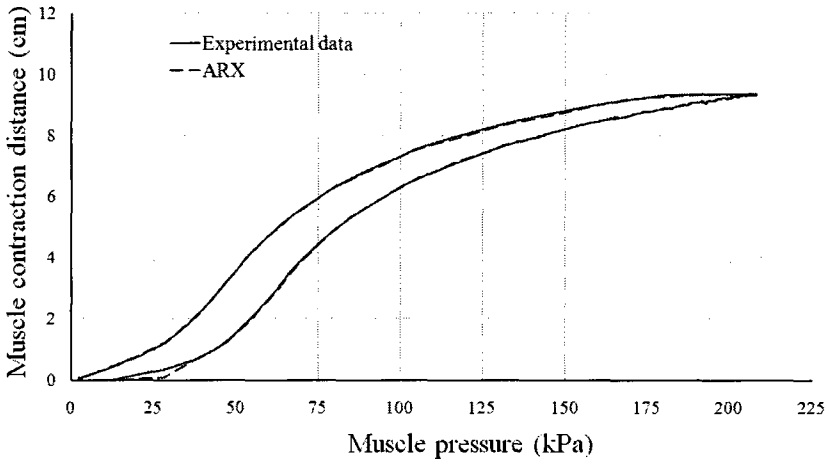

Figure 8-6: ARX model and LS algorithm validation results for n2_D1.9 prototype.

Figure 8-6 shows that the ARX model with the LS algorithm can reasonably emulate the muscle system. The developed ARX model is given as follows:

$$y(k) = 1.8716y(k-1) - 0.8775y(k-2) + 0.1286u(k-1) - 0.1225u(k-2) \quad (8\text{-}16)$$

The Laplace domain transfer function of this model is given by:

$$\frac{Y(s)}{U(s)} = \frac{0.67s + 0.1628}{s^2 + 0.6534s + 0.158} \quad (8\text{-}17)$$

Equation (8-17) is a second order transfer function that relates the muscle pressure (input) to the muscle contraction distance (output).

To test the robustness of the ARX model, the discrete system is converted to the time domain and validated for two pressure inputs of 207 kPa and 137 kPa. The results are shown in Figure 8-7 and Figure 8-8, respectively.

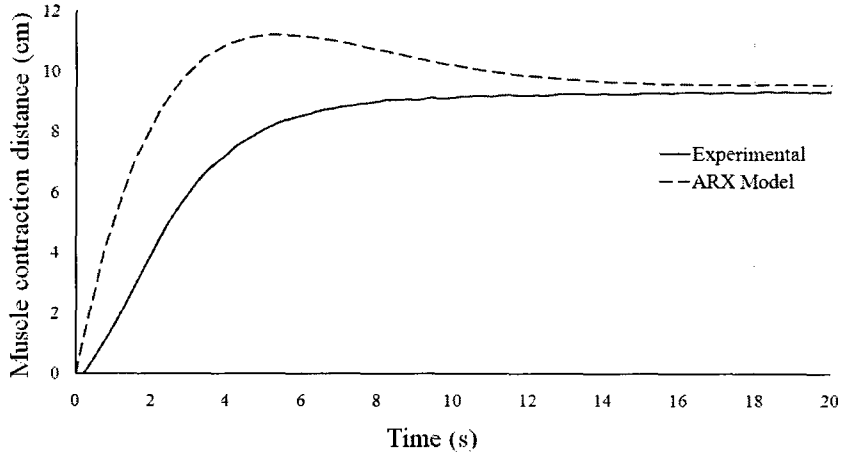

Figure 8-7: ARX model validation results for n2_D1.9 prototype for a pressure step input of 207 kPa.

In Figure 8-7, the ARX model has failed to predict accurately the muscle transient response, however, it has accurately predicted the muscle steady state response. This model predicts the muscle behaviour based on the two previous inputs and outputs data. This limits its capability to identify a non-linear system such as the BPM. In order to test the robustness of the ARX model steady state response, this model was tested for a step pressure input of 138 kPa (Figure 8-8).

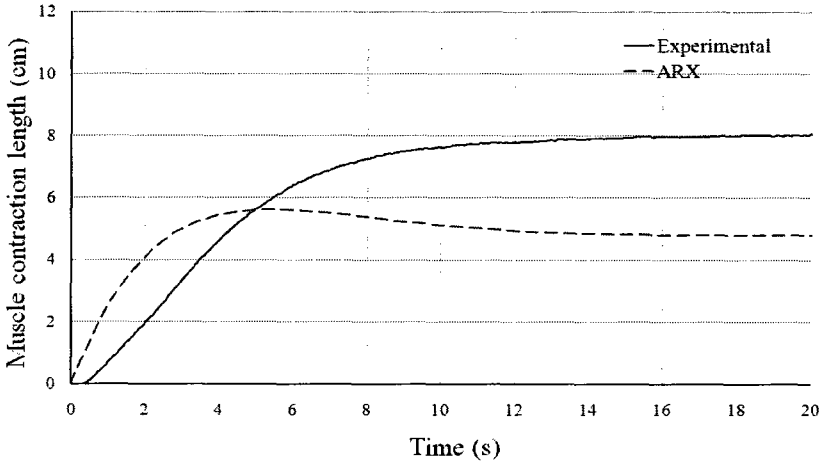

Figure 8-8: ARX model validation results for n2_D1.9 prototype for a pressure step input of 138 kPa.

The results in Figure 8-8 exhibit a large discrepancy between the ARX model and the experimental data. This confirms that the linearization of the BPM system for a single supply pressure (207 kPa) is not suitable as a general model. Piece-wise linearization can be considered such that multiple linear muscle models can effectively predict the muscle dynamic behaviour over a wide range of supply pressure.

8.5.2 Neural Network Models

Unlike the linear models, the NN models do not produce analytical relationships. The proposed NN models are called emulators. Firstly, using the experimental collected data, the NN is trained till its output reaches a desired accuracy. This accuracy is defined by the NN predicted output and the actual BPM output. Once the NN is trained, the converged NN connection weights and threshold are copied to a static NN for testing and validation. The validation is accomplished using a different set of data. The NN is implemented using C++ programming languages. The code is shown in Appendix D, Section D-3. Figure 8-9 shows the validation results for the NNARX model using the Conjugate Gradient algorithm.

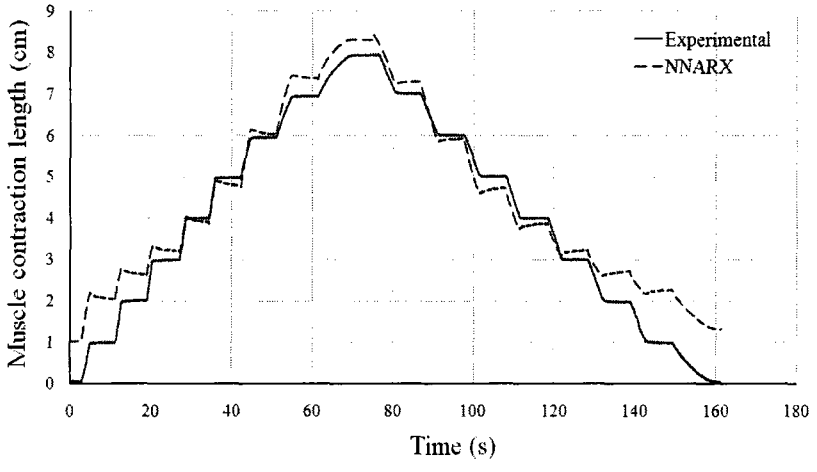

Figure 8-9: NNARX validation results for the muscle prototype n2_D1.9

This network was initially trained till it was able to track the training data set, however, subsequently to the training process; the NNARX has failed to predict the validation data test

(Figure 8-9). The NNARX is known as a pattern recognition tool, thus, the network is incapable of predicting the muscle behaviour for data sets that are different from which it was trained on. Figure 8-10 Figure 8-11 show the NNOE network validation results using the Conjugate Gradient algorithm for small step inputs of 1cm and for a large single muscle contraction of approximately 9.2 cm. The NNOE network was able to predict the validation data set once it was fully trained. As stated earlier, this network possesses an external recurrent property thus allowing the NNOE to learn the muscle dynamic behaviour rather than recognizing data patterns as in the case of the NNARX.

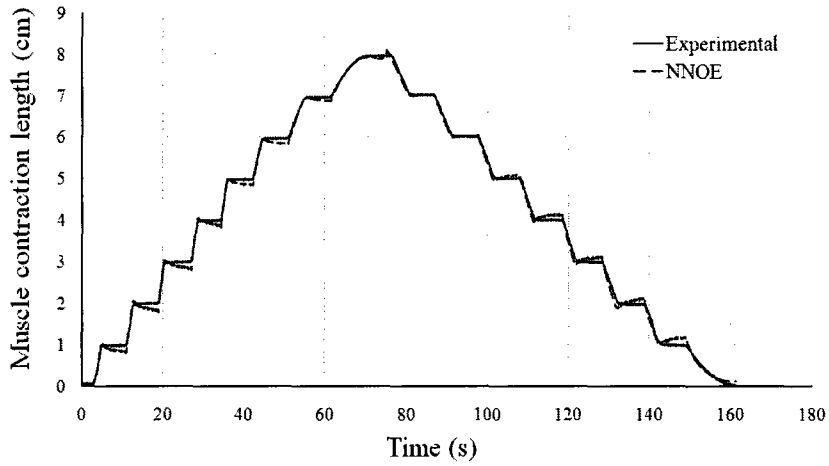

Figure 8-10: NNOE validation results for the muscle prototype n2_D1.9.

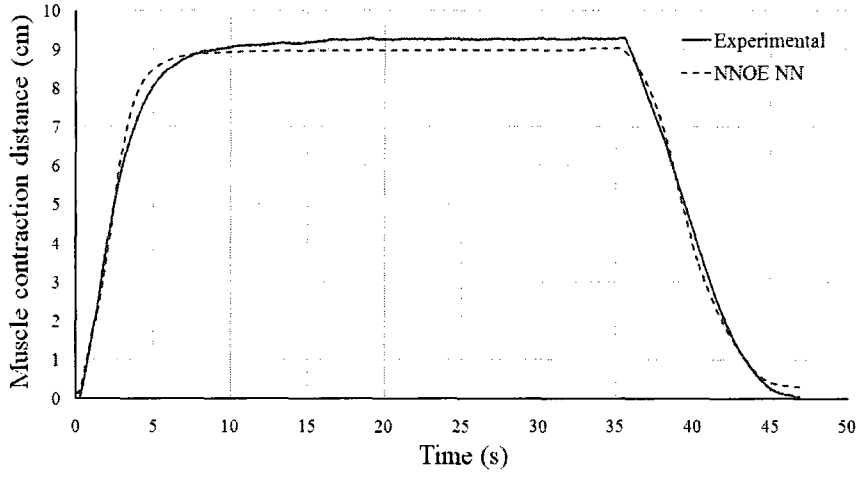

Figure 8-11: NNOE validation results for the muscle prototype n2_D1.9.

Unlike the linear model developed earlier, the NN models are capable of emulating the BPM contraction and relaxation phases for different inputs, namely, the valve orifice area, the supply pressure, the hanging mass and the muscle pressure. The NN structure could be expanded further to include many other muscle parameters such that the muscle geometric properties and thus the NN would have the capability to emulate different muscle sizes and configurations. The designer could use such a tool to predict muscle behaviours without developing and experimentally testing many similar BPM prototypes. Such a NN may also be used as a controller for accurate muscle operation. Both proposed NN algorithms, namely, the Back-propagation and the Conjugate Gradient algorithm are successfully implemented for offline training, however, the Conjugate Gradient algorithm has shown to converge faster to a solution and thus it is a superior candidate for online training.

Chapter 9

BPM CONTROLLER DESIGN

As with any other automated apparatus, the BPM system requires a controller to ensure that the system behaves according to the user's requirements. In this chapter, a Proportional Integral Derivative (PID) controller is mainly implemented to demonstrate the BPM's closed loop behaviour. Based on the Root Locus method, the PID controller is designed and later fine- tuned experimentally. Using MATLAB and a National Instruments data acquisition and control system, the PID controller is implemented for the analytical model as well as the physical setup, respectively.

9.1 BPM Controller Design

The BPM response requirements vary for different types of applications, fast and rigid for robotic systems and relatively slower and compliant for biomechanical systems. In each case, a controller is designed to ensure that the BPM behaviour adequately meets the response requirements. For this work, the user requirements are defined in terms of the system damping ratio and natural frequency (Table 9-1). These specifications are selected based on the operating condition for the BPM design criteria. The selected damping ratio represents a slightly under damped system whereas different settling time response is selected for the muscle contraction and relaxation phases. For a 2 % system settlement tolerance, the settling time t_s is determined as follows:

$$t_s = \frac{4}{\zeta \varpi_n} \tag{9-1}$$

where ζ is the system damping ratio and ϖ_n is the system natural frequency.

Table 9-1: BPM user requirements

User requirements	**Desired system characteristics**
Damping ratio	0.9
Natural frequency	Approximatively 0.6 rad / sec for BPM contraction Approximatively 0.25 rad / sec for BPM relaxation

The BPM controller design process starts by analyzing the BPM open loop characteristics. This includes the system stability, transient and steady state response. The muscle was tested using two pressure inputs of 138 kPa and 207 kPa (Figure 3-21). These results exhibit a damped system characteristic with no response oscillations prior to the system settling. This may also interpret that the BPM system is stable for the subjected inputs. A system is defined as stable if its output is bound when subjected to a disturbance.

In this work, a PID controller is desired. Also, the selected control design approach is based on the Root Locus technique and such the controller design should be based on a linear BPM model. Using the dynamic model presented in Section 6.5 (for n = 2, P_s = 207 kPa, n_g = 1.3 and Kf = 3) and the ARX system identification function in MATLAB, a linear BPM model n2_ARX is computed where the model input and output are the valve opening area and the muscle contraction distance, respectively. The valve opening area was selected as an input parameter since it is feasible to control it and it will affect the muscle pressure. Furthermore, to avoid modeling the muscle hysteresis, two linearized models are developed to predict the muscle contraction and relaxation modes. In such a case, two controllers are required for each mode. The linear BPM model n2_ARX is given by:

For the contraction phase:

$$\frac{Y(s)}{U(s)} = \frac{14998.601}{s^2 + 1.499s + 0.500} \tag{9-2}$$

For the relaxation phase:

$$\frac{Y(s)}{U(s)} = \frac{-7748.590}{s^3 + 2.2000s^2 + 1.5375s + 0.3375]} \tag{9-3}$$

Figure 9-1 and Figure 9-2 show the validation results for the n2_ARX model and analytical model from Section 6.5.

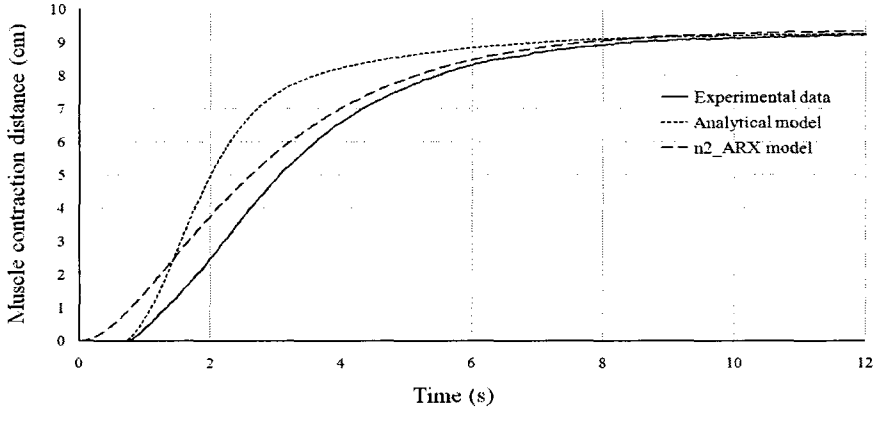

Figure 9-1: Validation results for the ng1.3 and the ARX_ng1.3 models (contraction) for the n2_D1.9 prototype for a valve opening area step input of 0.404 mm^2 (P_s = 207 kPa).

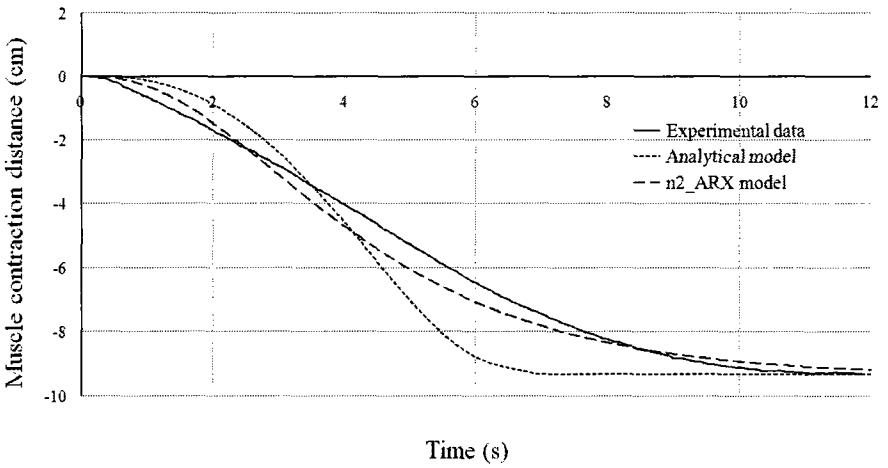

Figure 9-2: Validation results for the ng1.3 and the ARX_ng1.3 models (relaxation) for the n2_D1.9 prototype for a valve opening area step input of 0.404 mm^2 (P_s = 207 kPa).

The validation results for the n2_ARX model shown in Figure 9-1 and Figure 9-2 are in good agreement with the analytical model and the experimental data. The controller will be designed based on the n2_ARX model.

9.2 PID Controller Design

As mentioned above, the muscle is controlled by two linear PID controllers; the transfer function of such controllers $G_c(s)$ is given by:

$$G_c(s) = K_p + K_d s + \frac{K_i}{s} \tag{9-4}$$

where K_p is the proportional constant, K_d is the derivative constant, K_i is the integral constant. Assuming that the system has two dominant closed loop poles and based on the user requirements in Table 8-1, the dominant closed loop poles for the system must be located at:

For the contraction phase:

$$s_{c1} = -0.54 + j0.26 \;\; ; \;\; s_{c2} = -0.54 - j0.26 \tag{9-5}$$

For the relaxation phase:

$$s_{r1} = -0.225 + j0.108 \;\; ; \;\; s_{r2} = -0.225 - j0.108 \tag{9-6}$$

where s_{c1} and s_{c2} are the system dominant closed poles for the contraction phase, s_{r1} and s_{r2} are the system dominant closed poles for the relaxation phase. Based on these poles location, the angle of deficiency is calculated for the contraction and the relaxation phase. Finally, based on these angles of deficiency and the magnitude condition from the root locus design method, the PID controller constants are calculated. This yield to two PID controllers as follows:

For the contraction phase, the designed controller is:

$$G_c(s) = 5.015 \times 10^{-5}s + 7.217 \times 10^{-5} + \frac{2.45 \times 10^{-5}}{s} \tag{9-7}$$

For the relaxation phase, the designed controller is:

$$G_c(s) = 8.911 \times 10^{-6}s + 1.492 \times 10^{-5} + \frac{6.247 \times 10^{-6}}{s} \tag{9-8}$$

The linear PID controllers shown above are only valid for the linear models given by Equations (9-2) and (9-3), however, the time constants serve as initial tuning values for the PID controllers when they are implemented for the non-linear model ng1.3 and for the experimental testing. Appendix D, Figure D-3 shows the MATLAB Simulink block diagram used for testing the PID controllers and the ng1.3 model. For this case, it is designed to have one controller active at a time; otherwise, the controllers' outputs would counteract each other. The pneumatic valve opening areas are considered as the operating range limits for the controllers. The response of this closed loop system for a contraction distance input of 8 cm is shown in Figure 9-3.

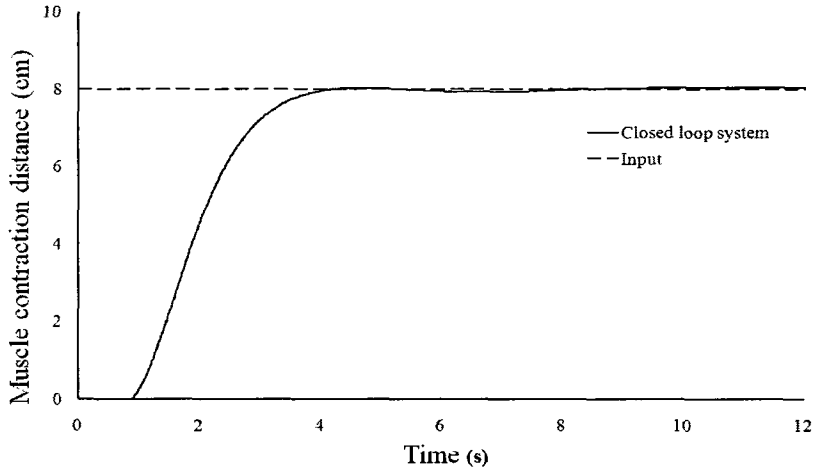

Figure 9-3: Step response results for the closed loop analytical model for the n2_D1.9 prototype (P_s = 207 kPa).

Figure 9-3 confirms that the controller has limited the system oscillation/overshoot and improved the steady state value. In order to show the controller stability and robustness, a disturbance mass of 4.6 Kg is introduced to the system every 15 seconds. The results of this test are shown in Figure 9-4.

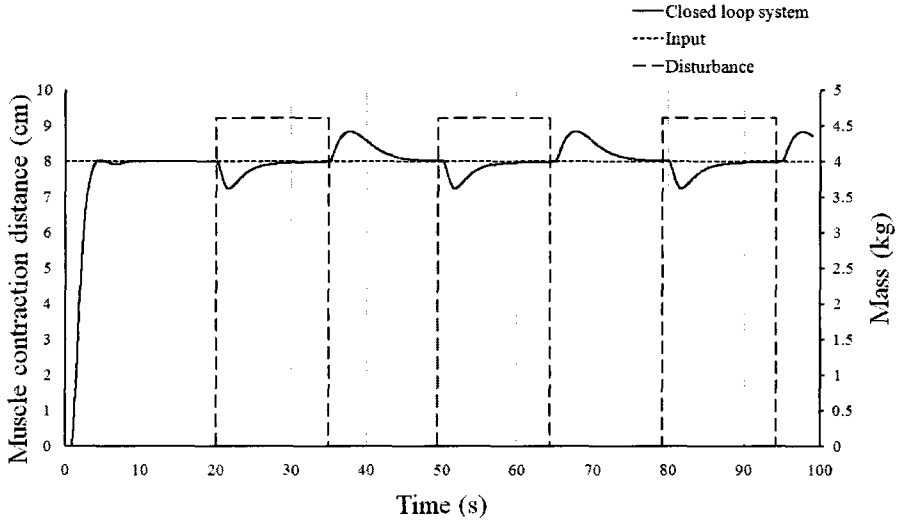

Figure 9-4: Mass disturbance response results for the closed loop model (ng1.3) for the n2_D1.9 prototype (P_s = 207 kPa).

Figure 9-4 shows that the PID controller is capable of counteracting the disturbance by bringing the BPM to the input contraction distance value (8cm). The speed of this process is slow; this is attributed to the PID controllers' limits which reflect the operating range of the pneumatic valves.

9.3 BPM Controller Experimental Testing

In the previous section, two linear controllers are designed to control the inflation and deflation valves based on the BPM linear model (ARX_ng1.3) and the Root Locus design technique. In this section, the PID controllers are implemented for the n2_D1.9 prototype. The schematic of this muscle contraction distance control is shown in Figure 9-5. The implementations of these controllers are achieved by programming a block diagram using LabVIEW software. Also, the same program serves as a data acquisition system for the experiment. The LabVIEW sampling time was 0.01 seconds.

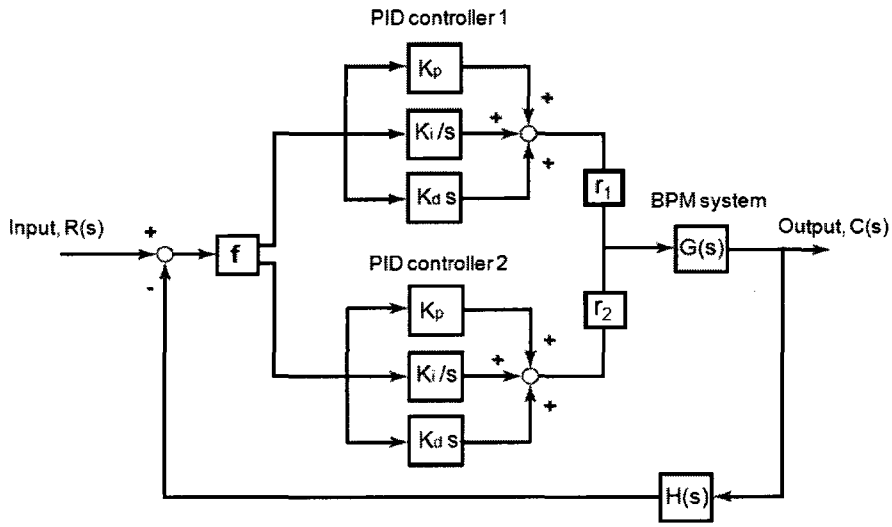

Figure 9-5: BPM closed loop system schematic including two linear PID controllers.

As shown in Figure 9-5, the user specifies the BPM contraction distance input *R(s)* which is then compared to the actual muscle contraction distance. The difference is the error value that is fed back to the appropriate controller through the function *f* depending on whether the muscle

contraction or relaxation is required. The PID controllers determine the appropriate output signal to drive the system. This output signal is constrained by the functions r_1 and r_2 which model the operating range of the pneumatic valves.

The designed and tuned PID controllers are tested for their capabilities to achieve accurate muscle contraction distance control. Figure 9-6 shows the closed loop response of the n2_D1.9 prototype when it is subjected to successive 2 cm step inputs till the muscle reaches near full contraction. The same process is repeated till the muscle returns to its deflated state. Figure 9-6 shows the accuracy of the PID controllers in dealing with the BPM contraction distance. The experimental results show no oscillation or steady state error value for each step input. The muscle response due to step inputs in the contraction phase is different from those in the relaxation one. This behaviour is expected since the controller and the muscle properties for contraction and relaxation modes are different. Furthermore, Figure 9-6 shows that the settling time for the 2 cm step inputs varies from 2 seconds to 8 seconds. Slower settling time are recorded in the contraction mode as the muscle approaches maximum contraction distance and in the relaxation mode as the muscle approach the full deflated state. This is explained by the variance in pressure differential between the muscle and supply source as the BPM contracts. This can also be attributed to the valves operating limits that lead to a limited flow rate and a slower muscle contraction speed.

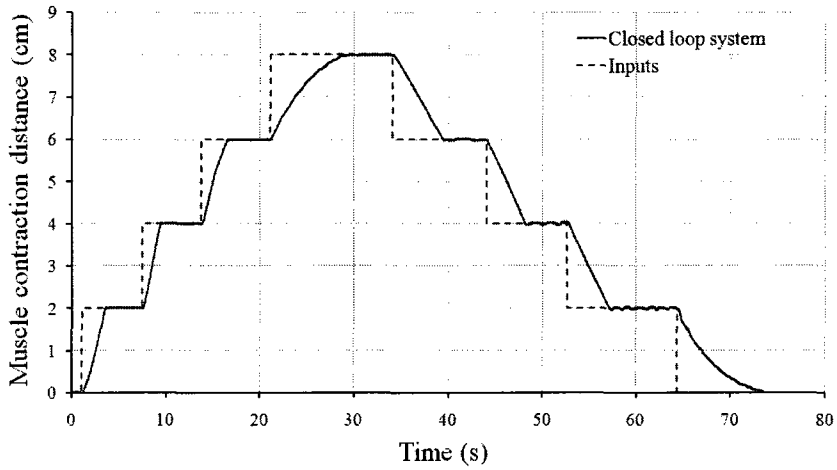

Figure 9-6: Closed-loop system response results for the n2_D1.9 prototype for multiple step inputs of 2 cm at a time.

The robustness of the PID controllers is tested by introducing a disturbing mass on the n2_D1.9 prototype when it is in steady state at a contraction distance of approximately 5 cm. A mass of 4.6 Kg is suddenly added to the suspended load. The closed loop system is given sufficient time to adjust back the muscle contraction distance to 5 cm and then the mass is removed. This cycle is repeated 5 times, the results of this test are shown in Figure 9-7.

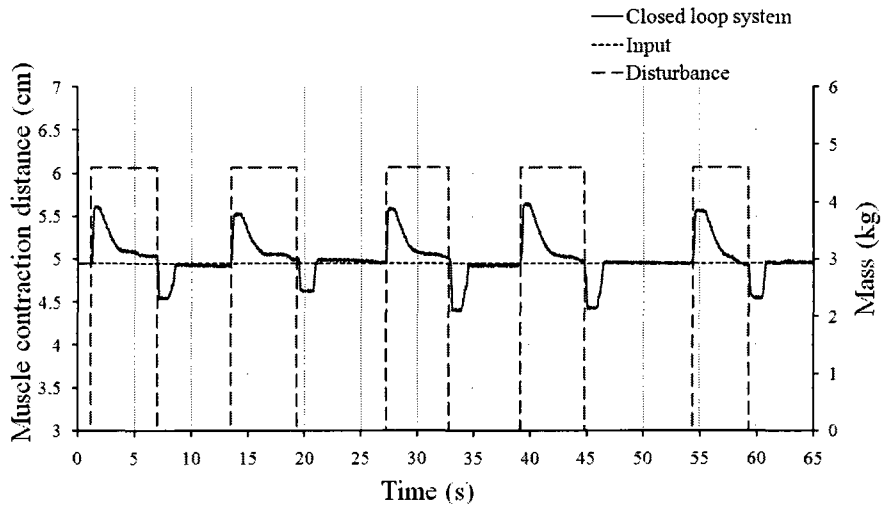

Figure 9-7: Muscle closed-loop system response results for the n2_D1.9_M4.6 prototype for a Mass disturbance of 4.6 kg.

Figure 9-7 shows a variation of muscle contraction distance peak points; this phenomenon is attributed to the manual method used for applying the disturbance (mass).

Chapter 10

CONCLUSIONS AND RECOMMENDATIONS FOR FUTURE WORK

10.1 Conclusions

The objective of the thesis was to develop mechanical models that would allow the user to design or select a BPM that satisfies as set of prescribed requirements. A literature survey was first conducted to identify and analyze previous research achievements. The survey was structured based on BPM's categories such that potential research improvements are identified. In particular, it was noted that the BPM lacks a comprehensive experimental evaluation and accurate mechanical models. This led the research to design and manufacture 25 BPM prototypes distinct by their sizes and configurations. The prototypes are subsequently tested using three setups that provided the required type of muscle contraction, namely, concentric muscle contraction, eccentric muscle contraction, and isometric muscle contraction.

The prototypes testing led to a comprehensive experimental evaluation of the BPM's static and dynamic behaviour. This was trivial for developing accurate BPM models. The muscle force and the muscle contraction distance behaviours are extensively analyzed while varying the prototype configuration and operating mode. Moreover, the testing has identified key BPM's parameters such as the muscle end effect. The end fixture size has been shown to affect the muscle geometry and the muscle force. Acknowledging the BPM non-cylindrical form, a muscle shape is proposed which treats the muscle ends as cone frustums. The developed geometrical model predicted the muscle contraction distance and the muscle surface area with NRMS values of 1.9 % and 3.9 %, respectively. Furthermore, this work presented an analytical BPM jamming model for both end states of the muscle braid. Such a model allows the designer to predict the muscle length end points prior to fabricating the BPM prototype.

A force-based static model was developed and experimentally validated. The model considers the netting analysis of the muscle braid as well as the bladder effects. The friction between the braided fibres as the braid angle changes is modeled using a Hertz contact stress model. The results for the force-based model are compared to that of Chou and Hannaford for several muscle configurations that are experimentally tested. The force-based and Chou and Hannaford models achieved NRMS values range of 3 to 35 % and 8 to 144 %, respectively. For all cases, the proposed force-based model was shown to be more accurate.

A comprehensive graphical design process was proposed for two types of muscle contraction, namely, the muscle concentric contraction and the muscle isometric/eccentric contraction. The advantage of the proposed design process is that it allows the designer the ability to rapidly and easily explore visually multiple design solutions to select the most appropriate muscle parameters for a given application. The design processes are illustrated using numerical values for the two contraction cases.

A Newtonian-based fully analytical dynamic model of the BPM was also developed. The model incorporates an analysis of the pneumatic system and a fibre to fibre friction model. The model results are compared to those from experiments conducted on prototype BPM's. The results presented show that the proposed model predicts accurately the steady state response for the muscle contraction distance and the muscle pressure. However, the transient response of the model was less accurate and this was attributed to the adopted assumptions (*e.g.* friction mechanism between fibres). The main advantage of this analytical model over other empirical or experimentally-based models reported in the literature is that it does not require a characterization of a particular muscle configuration.

Linear and non-linear systems are considered as an alternative solution for predicting the muscle dynamic behaviour. The linear AR system model has failed to predict the muscle dynamic behaviour for different pressure input. However, the NN model (NNOE) was capable of emulating the muscle dynamic behaviour in the contraction and relaxation phases for various inputs. In this process, two algorithms, namely, the Back-propagation and the Conjugate Gradient algorithm are successfully implemented for offline training.

Finally, using a linearized form of the dynamic model and the Root Locus method, a linear PID controller was designed to show the closed loop behaviour of the muscle. The time constants of this controller were used as an initial estimate for the prototype controller implementation. The tuned PID controller has accurately controlled the muscle contraction distance for multiple step inputs. Furthermore, this controller was shown to be stable when the system was subjected to an external disturbance (*i.e.* additional mass).

10.2 Recommendations for Future Work

In this work, the emphasis was mainly on analyzing, modeling and controlling the BPM. Therefore, the muscle was built based on a design that offers flexibility to modify muscle parameters such as the end fixtures size, braid and bladder. However, it is also important to manufacture a reliable and robust muscle that would survive many life cycles. This would require attention to the design of the end muscle fixtures which currently are standard brass couplings and mechanical straps which are suitable for low cycles testing. The end fixture locking mechanism should provide great strength for holding the braid and bladder yet should not damage the braid/bladder for long cycling repetition.

A PID controller was designed to control the BPM motion based on the muscle contraction distance. However, many applications may require additional controls that are based on additional muscle parameters such as the muscle contraction velocity and the muscle force. Analytical models for these two muscle parameters have been derived; however, the experimental setup and the adopted single input signal output model for the muscle control are not feasible for this implementation. Furthermore, the BPM was identified as a non-linear system and the developed BPM dynamic model was non-linear as well. Therefore, non-linear controllers may offer greater muscle control accuracy, specifically for complex muscle motion trajectories.

Advance controllers and more specifically adaptive controllers have been used extensively by researchers to manipulate the BPM. These controllers offered good results when used with poor or non-existing BPM models. However, if these controllers are based on the developed models in this work, greater control results can be expected.

The Neural Network system identification structures have shown to be great emulators for the muscle behaviour. This NN can be expanded to include all BPM parameters such that it can predict the muscle behaviour irrespective of the muscle prototype size or configuration. Such a Neural Network may also be implemented as a controller for the muscle operation. This controller may include muscle contraction distance, muscle contraction velocity, muscle force and other muscle properties as controlled variables.

REFERENCES

[1] B. W. Andersen, *The analysis and design of pneumatic systems*. Huntington: Robert E. Krieger Publishing, 1976.

[2] C. R. Johnson and R. C. Pierce, "Expansible cover," U.S. Patent 2 238 058, April 15, 1941.

[3] H. De Haven, "Tensioning device for producing a linear pull," U.S. Patent 2 483 088, September 27, 1949.

[4] R. H. Gaylord, "Fluid acutated motor system and stroking device," U.S. Patent 2 238 058, July 22, 1958.

[5] V. Nickel and A. Garrett, "Development of useful function in the severely paralysed hand," *The Journal of Bone and Joint Surgery*, vol. 45, no. 5, pp. 933-952, 1963.

[6] G. K. Klute, M. J. Czerniecki, and B. Hannaford, "McKibben artificial muscles: pneumatic actuators with biomechanical intelligence," in *IEE International Conference on Advanced Intelligent Mechatronics*, Atlanta, 1999.

[7] K. Inoue, "Rubbertuators and applications for robots," in *Robotics Research: The 4th International Symposium*, Cambridge, 1988, pp. 57-63.

[8] Shadow Robot Company Ltd. Shadow Robot Comapany. [Online]. www.shadowrobot.com

[9] 20th Century Fox. I Robot movie. [Online]. www.irobotmovie.com

[10] NASA. Robonaut. [Online]. http://robonaut.jsc.nasa.gov/

[11] D. Ferris and R. Palmieri-Smith. Human Neuromechanics Laboratory. [Online]. http://www.kines.umich.edu/research/chmr/hnl.html

[12] D. P. Ferris, G. S. Sawicki, and A. Domingo, "Powered lower limb orthoses for gait rehabilitation," *Journal of Applied Biomechanics*, vol. 11, no. 2, pp. 34-39, 2005.

[13] Festo Inc. Festo. [Online]. www.festo.com

[14] D. G. Caldwell, N. Tsagarakis, G. Medrano-Cerda, J. Schofield, and S. Brown, "Development of a pneumatic muscle actuator driven manipulator rigfor nuclear waste retrieval operations," in *IEEE International Conference Robotics and Automation*, vol. 1, Detroit, 1999, pp. 525-530.

[15] H. F. Schulte, D. F. Adamski, and J. R. Pearson, "Characteristics of the braided fluid actuator," Department of physical medicine and rehabilitation, University of Michigan, Michigan, Technical report, 1961.

[16] C. P. Chou and B. Hannaford, "Measurement and modeling of McKibben pneumatic artificial muscles," in *IEEE Transactions on Robotics and Automation*, vol. 12, Seatle, 1996, pp. 90-102.

[17] D. G. Caldwell, G. A. Medrano-Cerda, and C. J. Bowler, "Investigation of bipedal robots locomotion using pneumatic muscle actuators," in *IEEE International Conference of Robotics and Automation*, vol. 1, New Mexico, 1997, pp. 799-804.

[18] S. Davis and D. G. Caldwell, "Braid effects on contractile range and friction modeling in pneumatic muscle actuators," *International Journal of Robotics Research*, vol. 25, no. 4, pp. 359-369, 2006.

[19] S. Davis, N. Tsagarakis, J. Canderle, and D. Caldwell, "Enhanced modeling and performance in braided pneumatic muscle actuator," *The International Journal of Robotics Research*, vol. 22, no. 13, 2003.

[20] N. Tsagarakis and D. G. Caldwell, "Improved modeling and assessment of pneumatic muscle actuators," in *International Conference on Robotics and Automation*, vol. 4, San Francisco, 2000, pp. 3641-3646.

[21] B. Tondu and P. Lopez, "Modeling and control of McKibben articial muscle robot actuators," *Control systems*, 2000.

[22] B. Tondu and P. Lopez, "Modeling and control of McKibben articial muscle robot actuators," *Control Systems Magazine*, vol. 20, no. 2, pp. 15-38, 2000.

[23] D. B. Reynolds, D. W. Repperger, C. A. Phillips, and G. Bandry, "Modeling the dynamic characteristic of pneumatic muscle," *Annals of Biomedical Engineering*, vol. 31, pp. 310-317, 2003.

[24] S. Thongchai, M. Goldfarb, N. Sarkar, and K. Kawamura, "A frequency modeling method of rubbertuators for control application in an IMA framework," in *American control conference*, Arlington, 2001.

[25] P. B. Petrović, "Modeling and control of an artificial pneumatic muscle, Part one: model building," in *The 10th Conf. on Mechanical Vibrations*, Timisoara, 2002.

[26] D. B. Reynolds, D. W. Repperger, C. A. Phillips, and G. Bandry, "Modeling the dynamic characteristic of pneumatic muscle," vol. 31, pp. 310-317, 2003.

[27] A. Sanchez, V. Mahout, and B. Tondu, "Nonlinear parametric identification of a McKibben artificial pneumatic muscle using flatness property of the system," in *IEEE International Conference on Control Applications*, vol. 1, Trieste, 1998, pp. 70-74.

[28] J. Brydson, *Plactics Materials*. Amsterdam: Butterworth-Heinemann, 1999.

[29] G. K. Klute and B. Hannaford, "Accounting for elastic energy storage in McKibben artificial muscle actuators," *Journal of Dynamic Systems, Measurement, and Control*, vol. 122, no. 2, pp. 386-388, 2000.

[30] K. Osuka, T. Kimura, and T. Ono, "H Control of a certain nonlinear actuator," in *The 29th*

Conference on Decision and Control, vol. 1, Honolulu, 1990, pp. 370-371.

[31] G. Zames, "Feedback and optimal sensitivity: model reference transformation," in *IEEE Transactions on Automatic Control*, vol. 26, 1981, pp. 301-320.

[32] A. Nouri, B. Gauvert, B. Tondu, and P. Lopez, "Generalized variable structure model reference adaptive control of one-link artificial muscle manipulation in two operating modes," in *IEEE International Conference on Systems, Man, and Cybernetics*, vol. 2, Toulouse, 1994, pp. 1944-1950.

[33] D. Caldwell, G. Medrano-Cerda, and M. Goodwin, "Control of pneumatic muscle actuators," *Control System Magazine*, vol. 15, no. 1, pp. 40-48, 1995.

[34] G. Medrano-Cerda, C. Bowler, and D. Caldwell, "Adaptive position control of antagonistic pneumatic muscle actuators," in *IEEE International Conference on Inteligent Robots and Systems*, vol. 1, 1995, p. 378.

[35] D. Cai and H. Yamaura, "A robust controller for manipulator driven by artificial muscle actuator," in *IEEE International Conference on Control Applications*, vol. 1, Dearborn, 1996, pp. 540-545.

[36] T. Kimura, S. Hara, T. Fujita, and t. Kagawa, "Control for pneumatic actuator systems using feedback linearisation with disturbance rejection," in *The American Control Conference*, vol. 1, Seatle, 1995, pp. 825-829.

[37] T. Kagawa, T. Fujita, and T. Yamanaka, "Nonlinear model of artificial muscle," in , vol. 29, 1993, pp. 1241-1243.

[38] P. Carbonell, Z. P. Jiang, and D. W. Repperger, "A fuzzy backstepping controller for a pneumatic muscle actuator system," in *IEEE International Symposium on Inteligent Control*, vol. 1, Mexico, 2001, pp. 353-358.

[39] P. Carbonell, Z. Jiang, and D. Repperger, "Nonlinear control of a pneumatic muscle actuator: backstepping vs. sliding-mode," in *IEEE International Conference on Control Application*, vol. 1, Mexico, 2001, pp. 167-172.

[40] M. Ozkana, K. Inoue, K. Negishi, and T. Yamana, "Defining a neural network controller structure for a rubbertuator robot," *Neural Networks* , vol. 13, no. 4, pp. 533-544, 2000.

[41] H. Miyamoto, M. Kawato, and R. Suziki, "Feedback-error-learning neural network for trajectory control of a robotic manipulator," in *IEEE International Conference on Neural Networks*, vol. 3, 1988, pp. 251-265.

[42] K. J. Åström, C. C. Hang, P. Persson, and W. K. Ho, "Toward intelligent PID control," *Journal of IFAC*, vol. 28, no. 1, pp. 1-9, Jan. 1992.

[43] T. D. C. Thanh and K. K. Ahn, "Control pneumatic artificial muscle manipulator with nonlinear PID controller using neural network," in *International Symposium on Electrical and Electronics Engineering*, Vietnam, 2005.

[44] Techflex Inc. Techflex. [Online]. http://www.techflex.com/splashpage.asp

[45] GetData Graph Digitizer. Digitize graphs and plots - GetData Graph Digitizer - graph digitizing software. [Online]. http://getdata-graph-digitizer.com

[46] S. Davis and D. G. Caldwell, "Braid effects on contractile range and friction modeling in pneumatic muscle actuators," *The International Journal of Robotics Research*, vol. 25, no. 4, pp. 359-369, 2006.

[47] F. K. Ko, C. M. Pastore, and A. A. Head, *Handbook of industrial braiding*. Atkains & Pearce, 1988.

[48] M. P. Data. (2009, Jan.) MatWeb. [Online]. www.matweb.com

[49] J. R. Roark and W. Young, *Formulas for stress and strain*. New York: McGraw-Hill, 1975.

[50] G. Eckold, "Design and Manufacture of Composite Structures," 1994.

[51] A. Fahim, "Design, analysis, and performance evaluation of a polar based contouring system," Ph.D. dissertation, Dept. Mech. Eng., Concordia Univ., Sherbrooke, QC, 1983.

[52] Clippard Minimatic. Clippard Instrument Laboratory Inc. [Online]. http://www.clippard.com/

[53] S. Andersson, A. Soderberg, and S. Bjorklund, "Friction models for sliding dry, boundary and mixed lubricated contacts," *Tribology International*, vol. 40, pp. 580-587, 2007.

[54] O. Nelles, *Nonlinear system identification*. Berlin: Springer, 2001.

[55] G. E. Box and G. M. Jenkins, *Times series analysis, forecasting and control*. Holden-Day, United States: Prentice Hall, 1970.

[56] P. Eykhoff, *System identification*. London: John Wiley and Sons , 1974.

[57] R. Johansson, *System modeling & identification*. Englewood Cliffs: Prentice Hall, 1993.

[58] L. Ljung, *System Identification: Theory for the user*. Englewood Cliffs: Prentice Hall, 1987.

[59] T. Soderstrom and P. Stoica, *System identification*. New York: Prentice Hall, 1989.

[60] K. S. Narendra and K. Parthasarathy, "Identification and control of dynamical systems using Neural Network," in *IEEE Transactions on Neural Networks*, vol. 1, 1990, pp. 4-27.

[61] M. R. G. Meireles, P. E. M. Almeida, and M. G. Simoes, "A comprehensive review for industrial applicability of artificial Neural Network," in *IEEE Transactions on Industrial Electrocis*, vol. 50, 2003, pp. 585-601.

[62] B. Widrow, R. G. Winter, and R. A. Baxter, "Layered neural nets for pattern recognition," in *IEEE Transactions on Acoustics, Speech and Signal Processing*, vol. 36, 1988, pp. 1109-1118.

[63] S. S. Rao, *Optimization Theory and application*. New York: Wiley, 1984.

[64] O. Bretscher, *Linear Algebra With Applications*. Upper Saddle River, United States:

Prentice Hall, 1995.

[65] F. Rosenblatt, "The Perceptron: A probabilistic model for information storage and organization in the brain ," *Psychological Review*, vol. 65, no. 6, p. 386–408, 1958.

[66] J. J. Hopfield, "Neural Networks and physical systems with emergent collective computational abilities," in *National Academy of Sciences of the United States of America*, vol. 79, 1982, pp. 2554-2558.

[67] J. Elman, "Finding structure in time," University of California, San Diego, 1990.

[68] S. Haykin, *Neural Networks a comprehensive foundation*. New Jersey: Prentice Hall, 1999.

[69] J. Sola and J. Sevilla, "Importance of input data normalization for the application of neural networks to complex industrial problems," in *IEEE Transactions on Nuclear Science*, vol. 44, 1997, pp. 1464-1468.

[70] R. Rojas, *Neural Networks - A Systematic Introduction*. New-York: Springer-Verlag, 1996.

[71] H. Demuth and M. Beale, *Neural network toolbox: For use with MATLAB*. United States: The Math Works, 1994.

APPENDIXES

APPENDIX A

BPM EXPERIMENTAL RESULTS

A.1 Muscle Contraction Distance Ratios

Table A-1: Muscle concentric contraction results for BPM prototypes that are distinct in configuration and operating mode.

Muscle code	Deflated BPM length (cm)	Muscle contraction length (cm)	Muscle contraction length ratio (%)
1n_D1.9_E2.5_P138_M2.3_B2.0	15.8	3.73	23.63
1n_D1.9_E2.5_P138_M4.6_B2.0	16	3.61	22.54
1n_D1.9_E2.5_P138_M9.1_B2.0	16.3	3.12	19.17
1n_D1.9_E2.5_P207_M2.3_B2.0	15.8	4.11	26.04
1n_D1.9_E2.5_P207_M4.6_B2.0	16	4.2	26.26
1n_D1.9_E2.5_P207_M9.1_B2.0	16.3	3.86	23.69
1n_D1.9_E2.5_P138_M2.3_B2.0	16.5	3.89	23.55
1n_D1.9_E1.3_P138_M4.6_B2.0	16.6	3.66	22.03
1n_D1.9_E1.3_P138_M9.1_B2.0	16.8	3.02	17.99
1n_D1.9_E1.3_P207_M2.3_B2.0	16.5	4.8	29.09
1n_D1.9_E1.3_P207_M4.6_B2.0	16.6	4.45	26.78
1n_D1.9_E1.3_P207_M9.1_B2.0	16.8	4.01	23.89
2n_D1.9_E1.3_P138_M2.3_B2.0	32.1	8.74	27.22
2n_D1.9_E1.3_P138_M4.6_B2.0	32.3	8.15	25.24
2n_D1.9_E1.3_P138_M9.1_B2.0	33.2	7.11	21.42
2n_D1.9_E1.3_P207_M2.3_B2.0	32.1	9.86	30.7
2n_D1.9_E1.3_P207_M4.6_B2.0	32.3	9.4	29.1
2n_D1.9_E1.3_P207_M9.1_B2.0	33.2	9.19	27.7
2n_D1.9_E1.6_P138_M2.3_B2.0	32.5	8.37	25.76
2n_D1.9_E1.6_P138_M4.6_B2.0	32.6	7.91	24.27
2n_D1.9_E1.6_P138_M9.1_B2.0	32.4	6.99	21.56
2n_D1.9_E1.6_P207_M2.3_B2.0	32.5	9.79	30.12
2n_D1.9_E1.6_P207_M4.6_B2.0	32.6	9.27	28.44
2n_D1.9_E1.6_P207_M9.1_B2.0	32.4	9.17	28.3
2n_D1.9_E2.5_P138_M2.3_B2.0	32.2	8.15	25.32
2n_D1.9_E2.5_P138_M4.6_B2.0	32.3	7.77	24.06
2n_D1.9_E2.5_P138_M9.1_B2.0	32.5	6.83	21.02
2n_D1.9_E2.5_P207_M2.3_B2.0	32.2	9.27	28.79
2n_D1.9_E2.5_P207_M4.6_B2.0	32.3	9.04	28
2n_D1.9_E2.5_P207_M9.1_B2.0	32.5	8.38	25.79
2n_D1.9_E1.3_P138_M2.3_B1.4	32.8	6.54	19.94
2n_D1.9_E1.3_P138_M4.6_B1.4	33	6.36	19.27
2n_D1.9_E1.3_P138_M9.1_B1.4	33.4	5.62	16.83
2n_D1.9_E1.3_P207_M2.3_B1.4	32.8	7.43	22.64
2n_D1.9_E1.3_P207_M4.6_B1.4	33	7.47	22.64
2n_D1.9_E1.3_P207_M9.1_B1.4	33.4	7.23	21.66
2n_D1.9_E1.3_P276_M2.3_B1.4	32.8	9.09	27.7
2n_D1.9_E1.3_P276_M4.6_B1.4	33	9.07	27.48
2n_D1.9_E1.3_P276_M9.1_B1.4	33.4	8.78	26.27

Table A-2: Muscle concentric contraction results for BPM prototypes that are distinct in size, configuration and operating condition.

Muscle code	Deflated BPM length (cm)	Muscle contraction length (cm)	Muscle contraction length ratio (%)
3n_D1.9_E1.3_P138_M2.3_B2.0	48.5	12.92	26.65
3n_D1.9_E1.3_P138_M4.6_B2.0	48.7	12.54	25.75
3n_D1.9_E1.3_P138_M9.1_B2.0	49	11.38	23.22
3n_D1.9_E1.3_P207_M2.3_B2.0	48.5	14.36	29.62
3n_D1.9_E1.3_P207_M4.6_B2.0	48.7	14.42	29.61
3n_D1.9_E1.3_P207_M9.1_B2.0	49	13.64	27.84
3n_D1.9_E2.5_P138_M2.3_B2.0	48.5	12.54	25.86
3n_D1.9_E2.5_P138_M4.6_B2.0	48.7	11.84	24.32
3n_D1.9_E2.5_P138_M9.1_B2.0	49	10.8	22.04
3n_D1.9_E2.5_P207_M2.3_B2.0	48.5	14.26	29.4
3n_D1.9_E2.5_P207_M4.6_B2.0	48.7	14	28.74
3n_D1.9_E2.5_P207_M9.1_B2.0	49	13.22	26.98
3n_D0.9_E1.3_P138_M2.3_B2.0	21.5	3.04	14.14
3n_D0.9_E1.3_P138_M4.6_B2.0	22.5	1.89	8.4
3n_D0.9_E1.3_P138_M9.1_B2.0	23	0.53	2.29
3n_D0.9_E1.3_P207_M2.3_B2.0	21.5	3.85	17.89
3n_D0.9_E1.3_P207_M4.6_B2.0	22.5	3.32	14.74
3n_D0.9_E1.3_P207_M9.1_B2.0	23	1.41	6.12
4n_D0.9_E1.3_P138_M2.3_B2.0	28.5	4.43	15.55
4n_D0.9_E1.3_P138_M4.6_B2.0	29.5	3.06	10.37
4n_D0.9_E1.3_P138_M9.1_B2.0	30.8	0.85	2.77
4n_D0.9_E1.3_P207_M2.3_B2.0	28.5	4.84	16.97
4n_D0.9_E1.3_P207_M4.6_B2.0	29.5	4.62	15.65
4n_D0.9_E1.3_P207_M9.1_B2.0	30.8	2.6	8.45
4n_D0.9_E1.6_P138_M2.3_B2.0	28	3.4	12.16
4n_D0.9_E1.6_P138_M4.6_B2.0	28.8	2.44	8.46
4n_D0.9_E1.6_P138_M9.1_B2.0	30.8	0.9	2.92
4n_D0.9_E1.6_P207_M2.3_B2.0	28	5.37	19.19
4n_D0.9_E1.6_P207_M4.6_B2.0	28.8	4.56	15.83
4n_D0.9_E1.6_P207_M9.1_B2.0	30.8	2.37	7.71
5n_D0.9_E1.3_P138_M2.3_B2.0	35.4	5.46	15.43
5n_D0.9_E1.3_P138_M4.6_B2.0	36	3.88	10.79
5n_D0.9_E1.3_P138_M9.1_B2.0	39	1.29	3.3
5n_D0.9_E1.3_P207_M2.3_B2.0	35.4	6.34	17.92
5n_D0.9_E1.3_P207_M4.6_B2.0	36	5.51	15.3
5n_D0.9_E1.3_P207_M9.1_B2.0	39	3.89	9.98

A.2 System Energy Experimental Results

Table A-3: Muscle energy results for the n2_D1.9 prototype under different operating conditions.

BPM prototypes	Input energy (j)	Conserved energy (j)	Potential energy (j)	Lost energy (%)
2n_D1.9_P69_M2.3	28.5	15.9	0.9	41.1
2n_D1.9_P69_M4.6	25.0	14.6	0.9	38.0
2n_D1.9_P69_M6.8	23.2	14.0	1.6	32.4
2n_D1.9_P69_M9.1	19.6	13.0	1.7	24.9
2n_D1.9_P138_M2.3	57.0	39.4	1.7	27.9
2n_D1.9_P138_M4.6	55.3	38.1	3.1	25.4
2n_D1.9_P138_M6.8	53.5	36.8	4.2	23.2
2n_D1.9_P138_M9.1	51.7	36.6	5.3	19.0
2n_D1.9_P207_M2.3	80.2	58.4	1.8	24.9
2n_D1.9_P207_M4.6	80.2	59.5	3.6	21.4
2n_D1.9_P207_M6.8	76.6	59.6	5.3	15.3
2n_D1.9_P207_M9.1	78.4	59.1	7.0	15.7

Table A-4: *Muscle efficiency results for the n2_D1.9 prototype under different operating modes.*

BPM prototypes	η_1 (%)	η_2 (%)	Input energy (j)
2n_D1.9_P69_M2.3	58.9	3.2	28.5
2n_D1.9_P69_M4.6	62.0	3.6	25.0
2n_D1.9_P69_M6.8	67.6	7.0	23.2
2n_D1.9_P69_M9.1	75.1	8.7	19.6
2n_D1.9_P138_M2.3	72.1	2.9	57.0
2n_D1.9_P138_M4.6	74.6	5.6	55.3
2n_D1.9_P138_M6.8	76.8	7.9	53.5
2n_D1.9_P138_M9.1	81.0	10.2	51.7
2n_D1.9_P207_M2.3	75.1	2.2	80.2
2n_D1.9_P207_M4.6	78.6	4.4	80.2
2n_D1.9_P207_M6.8	84.7	7.0	76.6
2n_D1.9_P207_M9.1	84.3	8.9	78.4

Table A-5: BPM Static model accuracy results

Prototypes	Chou & Hannaford model		Force approach model		Max. muscle force
	RMS (N)	NRMS (%)	RMS (N)	NRMS (%)	(N)
1n_D1.9_E2.5_P207_L15.5	56.3	8	32.7	5	688
1n_D1.9_E2.5_P207_L15.0	86.4	15	22.3	4	572
1n_D1.9_E2.5_P207_L14.5	135	35	16.1	4	382
1n_D1.9_E2.5_P207_L13.5	101	33	27.9	9	303
1n_D1.9_E2.5_P207_L13.0	104.7	44	26.6	11	235
1n_D1.9_E2.5_P207_L11.9	112.7	48	36.1	15	84
2n_D1.9_E2.5_P207_L32.5	115.5	17	31.9	5	693
2n_D1.9_E2.5_P207_L31.0	114.6	20	14.2	3	561
2n_D1.9_E2.5_P207_L30.0	132.9	28	24.4	5	467
2n_D1.9_E2.5_P207_L28.0	142.3	45	29.8	9	316
2n_D1.9_E2.5_P207_L26.0	138.3	76	34.6	19	181
2n_D1.9_E2.5_P207_L25.0	125.3	101	39.3	32	124
3n_D1.9_E2.5_P207_L49.0	82.2	12	20.6	3	711
3n_D1.9_E2.5_P207_L47.0	140.6	25	37.6	7	552
3n_D1.9_E2.5_P207_L45.0	149.9	34	34.8	8	445
3n_D1.9_E2.5_P207_L43.0	150.1	43	36.4	10	347
3n_D1.9_E2.5_P207_L41.0	144.2	57	39.8	16	252
3n_D1.9_E2.5_P207_L39.0	133.5	133	54.5	33	122
1n_D1.9_E1.3_P207_L16.5	191.6	34	76.3	14	562
1n_D1.9_E1.3_P207_L16.0	173.6	42	56.3	14	483
1n_D1.9_E1.3_P207_L15.5	201.2	49	38.5	9	414
1n_D1.9_E1.3_P207_L14.5	168.5	57	29.7	10	295
1n_D1.9_E1.3_P207_L13.5	155.5	81	32.3	17	191
1n_D1.9_E1.3_P207_L12.5	133.4	144	32.5	35	92
2n_D1.9_E1.3_P207_L32.5	153.4	24	36.9	6	638
2n_D1.9_E1.3_P207_L31.0	153.9	31	20.8	4	494
2n_D1.9_E1.3_P207_L30.0	141.9	33	20.2	5	431
2n_D1.9_E1.3_P207_L28.0	128.8	48	21.2	7	304
2n_D1.9_E1.3_P207_L2.60	174.2	113	34.7	22	154
2n_D1.9_E1.3_P207_L25.0	147.1	144	27.8	27	102
3n_D1.9_E1.3_P207_L49.0	126.3	19	34.2	5	648
3n_D1.9_E1.3_P207_L47.0	122.2	22	23.46	4	545
3n_D1.9_E1.3_P207_L45.0	122.3	27	12.13	3	454
3n_D1.9_E1.3_P207_L43.0	116.9	32	20.1	5	368
3n_D1.9_E1.3_P207_L41.0	123.6	46	23.3	9	267
3n_D1.9_E1.3_P207_L39.0	101	49	19.5	9	207

Table A-6: BPM Static model accuracy results

Prototypes	Chou & Hannaford model		Force approach model		Max. muscle force
	RMS (N)	NRMS (%)	RMS (N)	NRMS (%)	(N)
8n_D0.9_E1.3_P207_L56.0	14.7	13	6.7	6	113
8n_D0.9_E1.3_P207_L55.0	16.5	16	3.2	3	106
8n_D0.9_E1.3_P207_L54.0	18.7	19	3.2	3	96
8n_D0.9_E1.3_P207_L53.0	20.1	23	6.2	7	87
8n_D0.9_E1.3_P207_L51.0	29.6	48	9.1	15	62
8n_D0.9_E1.3_P207_L49.0	31.3	77	13.7	34	41
5n_D0.9_E1.3_P207_L36.0	21.5	17	20.1	16	124
5n_D0.9_E1.3_P207_L35.0	20.2	18	4.8	4	112
5n_D0.9_E1.3_P207_L34.0	20.1	20	3.4	3	100
5n_D0.9_E1.3_P207_L33.0	24.3	29	4.5	5	83
5n_D0.9_E1.3_P207_L32.5	28.1	38	6.8	9	73
5n_D0.9_E1.3_P207_L30.5	32.7	77	11.7	27	43
3n_D0.9_E1.3_P207_L22.0	30.2	25	26.9	22	120
3n_D0.9_E1.3_P207_L31.0	23.5	23	6.2	6	102
3n_D0.9_E1.3_P207_L20.5	27.1	30	12.9	14	91
3n_D0.9_E1.3_P207_L20.0	29.5	39	11.9	16	76
3n_D0.9_E1.3_P207_L19.5	33.2	53	13.5	21	63
3n_D0.9_E1.3_P207_L18.7	28.12	63	15.1	34	44

Table A-7: Valve calibration experimental results

P1 kPa	P2 kPa	N12	Flow (L/min)	Effective Area cm ^2
282.5	0	1	10	0.00314
268.7	0	1	9.5	0.00314
248.0	0	1	9	0.00322
237.7	0	1	7.5	0.00280
217.0	0	1	7	0.00286
211.5	0	1	6	0.00252
186.0	0	1	5.5	0.00262
172.3	0	1	5	0.00258
151.6	0	1	4.2	0.00246
137.8	0	1	4	0.00258
106.8	0	1	3	0.00249
75.8	0	1	2.5	0.00293
59.3	0	1	1.8	0.00270
36.5	0	1	1.1	0.00267
32.4	0	1	1	0.00274

Appendix B

BPM Analytical Models Derivation

B-1 Muscle Pressure and Flow Linearization

The muscle pressure was identified as nonlinear with respect to the muscle contraction distance. Using the pneumatic theory explained by Andersen [1], the muscle pressure can be linearized by introducing a small variation to each state variable around an operating point. With reference to Figure B-1, the upper-case symbols denote state variables whereas the lower-case symbols denote the variations. The indices 1 and 2 denote the state of the supply and the muscle, respectively.

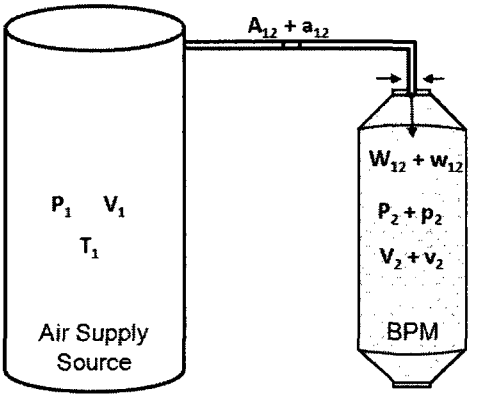

Figure B-1: BPM proposed structure, inlet orifice and model states variables

Assuming a steady flow of ideal gas through the cross orifice section A_{12}, the inflow rate for the muscle W_{12} is given by:

$$W_{12} = \rho_2 A_{12} u_2 \tag{B- 1}$$

where ρ_2 and μ_2 are the density and the speed of the fluid, respectively, at the cross section of the orifice. Assuming that the supply pressure P_1 is at local isentropic stagnation state (gas velocity is zero), this yields to:

$$P_1 = \left[1 - \frac{(\gamma - 1)\mu_2^2}{2\gamma g R T_1}\right]^{\frac{-\gamma}{(\gamma-1)}} P_2 \tag{B- 2}$$

where T_1 is the supply gas temperature, γ is the adiabatic index (heat capacity ratio)and R is the universal gas constant. by solving Equation (B-2) for the velocity term μ_2, this yields to the following equation:

$$\mu_2 = \left\{ \frac{2\gamma g R T_1}{\gamma - 1} \left[1 - \left(\frac{P_2}{P_1} \right)^{\frac{n-1}{n}} \right] \right\}^{1/2} \tag{B- 3}$$

Assuming an isentropic process, the density term could be expressed as a function of the supply pressure and temperature, as shown below:

$$\frac{\rho_2}{\rho_1} = \left(\frac{P_2}{P_1} \right)^{\frac{1}{\eta}} \tag{B- 4}$$

$$\frac{T_2}{T_1} = \left(\frac{P_2}{P_1} \right)^{\frac{\gamma-1}{\gamma}} \tag{B- 5}$$

Assuming an ideal gas, the supply pressure relationship is given by:

$$P_1 = \rho_1 R T_1 \tag{B- 6}$$

Solving for the density using Equations (B2-4), (B2-5) and (B2-6) results in equation below:

$$\rho_2 = \frac{P_1}{R T_1} \left(\frac{P_2}{P_1} \right)^{\frac{1}{\gamma}} \tag{B- 7}$$

Substituting the velocity relationship (B- 3) and the density relationship (B- 7) into the flow relationship (B- 1) and solving for the flow W_{12} yield to:

$$W_{12} = \frac{A_{12} P_1}{\sqrt{T_1}} \left\{ \frac{2\gamma g}{(\gamma - 1) R} \left[\left(\frac{P_2}{P_1} \right)^{\frac{2}{\gamma}} - \left(\frac{P_2}{P_1} \right)^{\frac{\gamma+1}{\gamma}} \right] \right\}^{1/2} \tag{B- 8}$$

Equation (B- 8) expresses the muscle in-flow as a function of the ratio of the muscle pressure to the supply pressure. The maximum flow through the orifice is given by the critical flow W_{cr}. This flow is achieved when the gas is at a critical velocity μ_{2c}, given by:

$$\mu_{2c} = \sqrt{\gamma g R T_2} \tag{B- 9}$$

The ratio of the flow W_{12} to W_{cr} is expresses by N_{12} as follows:

$$N_{12} = \frac{W_{12}}{W_{cr}} = \left[\frac{\left(\frac{P_2}{P_1}\right)^{\frac{2}{\gamma}} - \left(\frac{P_2}{P_1}\right)^{\frac{\gamma+1}{\gamma}}}{\frac{\gamma-1}{2}\left(\frac{2}{\gamma+1}\right)^{\frac{\gamma+1}{\gamma-1}}} \right]^{1/2} \tag{B- 10}$$

Substituting Equation (B- 10) in the flow relationship (B- 8) results in the following equation:

$$W_{12} = \frac{K P_1 A_{12} N_{12}}{\sqrt{T_1}} \tag{B- 11}$$

where K is given by:

$$K = \left[\frac{\gamma g}{R} \left(\frac{2}{\gamma+1}\right)^{\frac{\gamma+1}{\gamma-1}} \right]^{1/2} \tag{B- 12}$$

As the fluid flows from the supply source to the muscle through the orifice, the muscle pressure P_2, the muscle volume V_2, as well as the muscle gas temperature T_2 vary accordingly. Assuming an ideal gas, the states of the muscle can be identified using the ideal gas equation. The muscle gas mass M_2 is given as follows:

$$M_2 = \frac{P_2 V_2}{R T_2} \tag{B- 13}$$

As with the muscle pressure, the muscle gas mass can also be linearized by introducing a small variation to each state variable around an operating point. This yields to:

$$M_2 + m_2 = \frac{(P_2 + p_2)(V_2 + v_2)}{R(T_2 + t_2)}$$

$$M_2\left(1+\frac{m_2}{M_2}\right)=P_2V_2\frac{\left(1+\frac{p_2}{P_2}\right)\left(1+\frac{v_2}{V_2}\right)}{RT_2\left(1+\frac{t_2}{T_2}\right)}$$

Eliminating M_2 yields to:

$$\left(1+\frac{m_2}{M_2}\right)=\frac{\left(1+\frac{p_2}{P_2}\right)\left(1+\frac{v_2}{V_2}\right)}{\left(1+\frac{t_2}{T_2}\right)}$$

Developing the above relationship and neglecting all terms that correspond to a power order higher than 1 result in:

$$\frac{m_2}{M_2}=\frac{p_2}{P_2}+\frac{v_2}{V_2}-\frac{t_2}{T_2} \tag{B- 14}$$

Assuming a polytropic process, the temperature can be related to the pressure by n_g. The value of n_g varies between 1 for an isothermal process to 1.4 for an adiabatic process. This relationship is shown below:

$$\frac{t_2}{T_2}=\frac{n_g-1}{n_g}\frac{p_2}{P_2} \tag{B- 15}$$

Substituting Equation (B- 15) in Equation (B- 14) results in the following equation:

$$\frac{p_2}{P_2}=n_g\frac{m_2}{M_2}-n_g\frac{v_2}{V_2} \tag{B- 16}$$

Dividing Equation (B- 16) by time, the equation is as follows:

$$\frac{1}{P_2}\frac{dp_2}{dt}=n\frac{1}{M_2}\frac{dm_2}{dt}-n\frac{1}{V_2}\frac{dv_2}{dt} \tag{B- 17}$$

Mapping the derivatives in Laplace domain, and rearranging Equation (B- 17) yield to:

$$\frac{M_2}{nP_2}sp_2=sm_2-\frac{M_2}{V_2}sv_2 \tag{B- 18}$$

where s the Laplace operator that denotes d/dt, and sm_2 is the change in the mass of gas for the muscle and is equal to the mass flow rate W_{12} as follows:

$$sm_2 = W_{12} \tag{B- 19}$$

Assuming a steady flow rate through the orifice cross section A_{12}, the mass flow rate is given by Equation (B- 11).

B-2 Lease Square Algorithm

The LS algorithm was first described by Carl Friedrich Gauss [**64**]. This algorithm determines the model parameter such that the sum of squared residuals is optimized. This method is derived and demonstrated for a given model as follows:

$$y(k) = a_1 y(k-2) + a_2 y(k-1) + +b_1 u(k-2) + b_2 u(k-1)$$

where $u(k)$ is an input sequence, $y(k)$ is an output sequence, a's and b's are the constant parameters to be identified. A linear regression model is defined as follows:

$$y(k) = \phi^T(k)\theta$$

where $\phi^T(k)$ is a known regression vector and θ is a parameter vector to be identified.

$$\phi^T(k) = [y(k-1)\ \ y(k-2)\ \ u(k-1)\ \ u(k-2)]$$

$$\theta = \begin{bmatrix} a_1 \\ a_2 \\ b_1 \\ b_2 \end{bmatrix}$$

The estimated value of θ is identified as $\hat{\theta}$. The cost function J for an LS algorithm is given as follows:

$$J = \frac{1}{2}\frac{1}{N}\sum_{k=1}^{N}\left(y(k) - \phi^T(k)\hat{\theta}\right)^2$$

The optimum solution for this cost function with respect to $\hat{\theta}$ is determined as follows:

$$\frac{\partial J}{\partial \hat{\theta}} = 0 = \frac{1}{N}\sum_{k=1}^{N}\left(y(k) - \phi^T(k)\hat{\theta}\right)\phi$$

$$\frac{1}{N}\sum_{k=1}^{N}\phi y(k) - \frac{1}{N}\sum_{k=1}^{N}\phi\phi^T(k)\hat{\theta} = 0$$

If the solution parameters for a LS solution is identified as $\hat{\theta}^{LS}$, this yields to:

$$\hat{\theta}^{LS} = \left[\frac{1}{N}\sum_{k=1}^{N}\phi\phi^T\right]^{-1}\left[\frac{1}{N}\sum_{k=1}^{N}\phi y\right]$$

Other cost function that may be used for LS solution is given as follows:

$$J = \frac{1}{N}\sum_{k=1}^{N}\beta(N,t)\left(y(k) - \phi^T(k)\hat{\theta}\right)^2$$

where $\beta(N,t)$ is an additional term that decreases the effect of old data for a system parameter solution. A common relation used for $\beta(N,t)$ is:

$$\beta(N,t) = \lambda^{N-t}$$

where λ is a constant.

APPENDIX C

NEURAL NETWORK

C.1 Neural Network Introduction

The earliest kind of neural network is a Single-Layer Perceptron (SLP) network, which was first developed by Frank Rosenblatt in 1958 [**65**]. It is the simplest type of Feed-Forward Neural Network (FFNN). Distinctively, the FFNN networks transmit its data forward and never in a form of a feed-back. Now a day, Multiple Layer Perceptron (MLP) is one of the most widely used networks in this category. The MLP network is composed of 3 types of layers: (1) an input layer which contains the nodes that admit the data into the network; (2) an output layer that determines the network results; (3) and all other layers that exist in between the input and output layers, which are called the hidden layers. A graphical illustration of such a network is shown in Figure C-1.

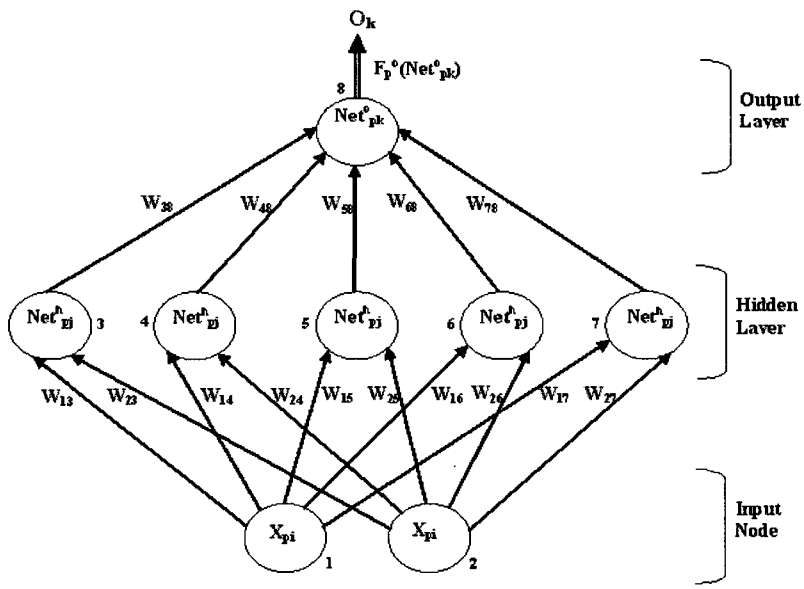

Figure C-1: MLP Neural Network structure

The output of each node of the network is a function of its input value and the chosen activation function. The input value is determined based on the sum of the product of past nodes outputs and their weights, this is given by:

$$X_j = \sum w_{kj} y_k \tag{C1-1}$$

where X_j is the input to node j, w_{kj} is the weight value for the link that connects node k to j and y_k is the output value for node k. The output value of node j is governed by the chosen activation function f.

$$y_j = f(x_j) \tag{C1-2}$$

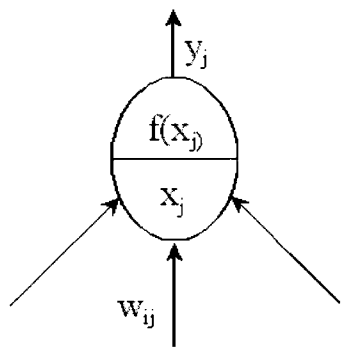

Figure C-2: Illustration of node output y_j as a function of activation function and node inputs

The activation function determines the output value for each node based on the sum of its inputs-weights value product. Selecting the right activation function of the output in a neural network is a critical task. The activation functions are responsible for introducing the non-linearity in the network and thus being able to emulate a non-linear system. In this work, the logistic (sigmoid) and hyperbolic function are used as the activation functions for the neural networks. They are both introduced and analyzed in Section C-2. The activation functions are selected based on the range of input data and algorithm used to solve the NN. Furthermore, depending on the output target values, the activation function may differ in hidden layers and output layers.

The Recurrent Neural Network (RNN) is the second type of NN analyzed, which is implemented in this work. It was first developed in 1982 by John Hopfield [66]; it is distinguished by the feed-back loops within the network. Two types of recurrent networks exist, namely an external and internal recurrent network. The main advantage of using a Recurrent Network is that it permits

the elimination of tapped delays for the network (*e.g.* MLP). Thus, it greatly accelerates the solution process as well as offers a better quality response. Such an advantage is due to the Recurrent Network associative memory property. One of the most common used RNN network was developed by Jeff Elman in 1990 [67]. This Neural Network structure is illustrated in Figure C-3.

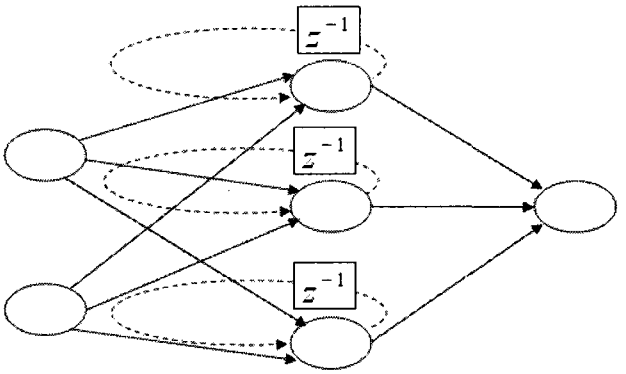

Figure C-3: Elman Neural Network structure [68]

C.2 Activation Functions

As previously discussed, the activation function determines the output value for each node. The logistic (sigmoid, Figure C-4) and the Hyperbolic (Figure C-5) functions are both introduced and their first derivative is derived next. The function's first derivative is required when implementing the NN using the Gradient Descent algorithm.

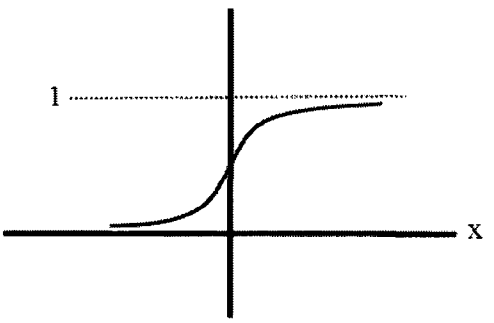

Figure C-4: Sigmoid activation function

The Sigmoid function is given by:

$$f(x) = \frac{1}{1 + e^{-gx}} \tag{C2-1}$$

For g =1,

$$\frac{df(x)}{dx} = \frac{1}{(1 + e^{-x})^2} \frac{d}{dx}(1 + e^{-x})$$

$$\frac{df(x)}{dx} = \left(\frac{1}{1 + e^{-x}}\right)\left(\frac{1}{1 + e^{-x}}\right)(-1)(e^{-x})$$

$$\frac{df(x)}{dx} = \left(\frac{1}{1 + e^{-x}}\right)\left(\frac{-e^{-x}}{1 + e^{-x}}\right)$$

An alternative way in which the sigmoid derivative function can be derived is as shown below:

$$\frac{df(x)}{dx} = f(x)\big(1 - f(x)\big) \tag{C2-2}$$

The Hyperbolic function is given by:

$$f(x) = tanh(x) = \frac{1 - e^{x}}{1 + e^{-x}} \tag{C2-3}$$

$$\frac{df(x)}{dx} = sec\, h^2(x)$$

$$\frac{df(x)}{dx} = 1 - tanh^2(x)$$

Alternatively, the hyperbolic derivative function can also be given as the following:

$$\frac{df(x)}{dx} = \big(1 - f(x)\big)\big(1 + f(x)\big) \tag{C2-4}$$

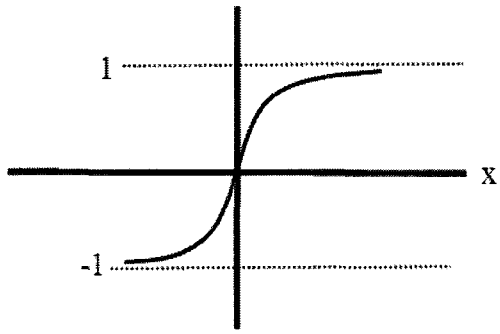

Figure C-5: Hyperbolic activation function

C.3 Neural Network Training

The Neural Network training phase determines the network properties, specifically the network weight and threshold values such that it would validate the BPM model. This procedure comprises of four steps, namely, selecting and executing a training data set, modifying the network weight as well as reiterating the cycle till the system is validated for the required accuracy specification.

Selecting and Executing Data Set

Ideally, the proposed NN structure is implemented online; however in this case, online training is unfeasible given the experimental setups feasibility. Online training is when the NN inputs are fed directly from an operating BPM rather than from previously collected data (offline). The selection of the training data sets is important for the success of the system model. The training data set covers a wide range of BPM operation for different excitation signals such that the Neural Network is able to classify correctly the input information. Furthermore, the data execution phase is as important as selecting the data itself. In this case, the data is randomly selected from the data bank in order to avoid network generalization.

Data normalization is used to obtain acceptable results within an optimized network convergence time [**69**]. Many normalization techniques exist (*e.g.* linear scaling or complex statistical methods that spread out the distribution of data). In this case, a linear scaling is implemented for both input and output data. This method is given as follows:

$$V = V_{min} + \frac{(V_{max} - V_{min})(D - D_{min})}{(D_{max} - D_{min})} \tag{C2-4}$$

where V is the normalized data value, V_{min} is the minimum of normalized data range, V_{max} is the maximum of normalized data range, D is the data value, D_{min} is the minimum value among data points and D_{max} is the maximum value among data points.

Modifying Neural Network Weight

Subsequently after running a data set into the NN, an output error is calculated for each node of the NN. This permits the NN algorithm to modify the network weights value such that the output error of each node is minimized. This process continues until the network weights reach a set of optimum values which would result in an acceptable error variation between the BPM and the network output values. Many optimization algorithms exist for determining the optimum network weight; the Back-propagation, steep descent and Conjugate Gradient are derived and analyzed later.

Network Validation

The network validation is achieved by testing a new data set through the network. The NN output results should be within the required accuracy specification; otherwise, the NN training process is repeated. It is never evident why a Neural Network fails to train. There are many reasons to why this is the case, some of obstacles would be following: (1) the network may be stuck in a local minima, (2) the network is over trained (over fitted), (3) an incomplete data set for NN training, (4) the wrong selection of NN system model, (5) the wrong selection of optimization algorithm and many other roots of cause.

C.4 NN Algorithms

Back-propagation Algorithm

The most common NN algorithm is Back-propagation. It was introduced by Paul Werbos in 1974 and later developed by David Rumelhart in 1986 [**70**]. This approach uses the Gradient Descent technique with error Back-propagation to optimize the network. The Gradient Descent technique assures that the network weight values converge in the negative direction of the cost function gradient. The error function is determined for the output layer and consequently feeds back to the network for weight adjustment. The Mean Square Error (MSE) is the most common function to determine the output layer error, which is given by the following equation:

$$E_k = \frac{1}{2}\sum(t_k - y_k)^2 \tag{C4-1}$$

where t_k and y_k are the expected and measured value for output node k, respectively. The MSE function avoids any cancellation of the negative and positive value for the output node errors. The weights value w_{jk} is modified in the negative gradient direction of the error function with a constant learning rate as follows:

$$\Delta w_{jk} = -\lambda \frac{\partial E_k}{\partial w_{jk}} \tag{C4-2}$$

where λ is the network constant learning rate. Using the chain rule, the partial derivative of the total error with respect to the network weight is decomposed as shown below:

$$\frac{\partial E}{\partial w_{jk}} = \frac{\partial E}{\partial y_k}\frac{\partial y_k}{\partial x_k}\frac{\partial x_k}{\partial w_{jk}} \tag{C4-3}$$

where x_k is the input node k. Next, each element of Equation C4-3 is derived as follows:

$$x_k = w_{jk}y_j \tag{C4-4}$$

$$\frac{\partial x_k}{\partial w_{jk}} = y_j \tag{C4-5}$$

Assuming the activation function to be sigmoid, its derivative is given by Equation (C2-2) as follows:

$$\frac{\partial y_k}{\partial x_k} = y_k(1 - y_k) \tag{C4-6}$$

Based on Equation (C4-1), the error function derivative is a function of output as follows:

$$\frac{\partial E_k}{\partial y_k} = -(t_k - y_k) \tag{C4-7}$$

Substituting Equations C4-5, C4-6 and C4-7 in Equation C4-3 results in:

$$\frac{\partial E}{\partial w_{jk}} = -(t_k - y_k)y_k(1 - y_k)y_j \tag{C4-8}$$

The error term is defined by δ and given by:

$$\delta_k = -\frac{\partial E_k}{\partial y_k}\frac{\partial y_k}{\partial x_k} \tag{C4-9}$$

Therefore,

$$\frac{\partial E}{\partial w_{jk}} = \delta_k y_j \tag{C4-10}$$

The weight connecting the output layer to the hidden layer is updated using:

$$\Delta w_{jk} = -\lambda \delta_k y_j \tag{C4-11}$$

The second step of the network optimization is to modify the weight of the hidden layer nodes. The expected error for the hidden node is not supplied. It is calculated based on the error

propagation method. Using the chain rule, the partial derivative of the output node error i with respect to the hidden node j output is decomposed as follows:

$$\frac{\partial E}{\partial w_{ij}} = \sum \frac{\partial E}{\partial y_j} \frac{\partial y_j}{\partial x_j} \frac{\partial x_j}{\partial w_{ij}} \tag{C4-12}$$

where,

$$\frac{\partial E}{\partial y_j} = \sum \frac{\partial E}{\partial y_k} \frac{\partial y_k}{\partial x_k} \frac{\partial x_k}{\partial y_j} \tag{C4-13}$$

and,

$$\frac{\partial x_k}{\partial y_j} = \frac{\partial (w_{jk} y_j)}{\partial y_j} = w_{jk} \tag{C4-14}$$

Substituting Equations (C4-10) and (C4-14) in Equation (C4-13) yield to:

$$\frac{\partial E}{\partial y_j} = -\sum \delta_k w_{jk} \tag{C4-15}$$

Equation (C4-15) propagates the error to the hidden node j base on error term value δ of the output layer and the weight value that exist between the two nodes. Substitute Equation (C4-15) in Equation (C4-12) yield to:

$$\frac{\partial E}{\partial w_{ij}} = -\sum (\delta_k w_{jk}) y_j (1 - y_j) y_i \tag{C4-16}$$

Or

$$\frac{\partial E}{\partial w_{ij}} = -\delta_j y_i \tag{C4-17}$$

The momentum term is another factor that can be applied to speed up the optimization process. The addition of the momentum term to the Steepest Descent algorithm allows the network to take in consideration past trends in the error rather than only the present gradient value. Such a

feature helps the network to converge faster and most importantly avoid the network to fall in a shallow local minimum. The momentum term has been described as a low pass filter [**71**] since it helps the network to disregard small features in the error. Adding the momentum term to the weight modification relationship result in the following equation:

$$\Delta w_{kj}(n) = \lambda \delta_j y_k + \eta \Delta w_{kj}(n-1) \tag{C4-18}$$

where, λ is learning rate constant, η is the momentum constant. For an output layer j, the error term δ corresponds to:

$$\delta_j = (t_j - y_j) y_j (1 - y_j) \tag{C4-19}$$

For hidden layer j, the error term δ corresponds to:

$$\delta_j = \left(\sum \delta_i w_{ji}\right) y_j (1 - y_j) \tag{C4-20}$$

The error term for the hidden layer requires the error term of the output layer. Therefore the weight modification starts from the outputs layers and propagates backward.

Conjugate Gradient Method

The Conjugate Gradient (Fletcher – Reeves) method is a form of unconstraint algorithm that initializes the optimizations process by evaluating the gradient of the cost function to obtain the first search direction but then redirects the search in its conjugate direction. Achieving consecutive conjugate direction steps assures a quadratic convergence. In other words, this method is capable of determining a function solution within a finite number of iterations. The search direction S_i for the Fletcher – Reeves algorithm [**63**] is given by the following equation:

$$S_i = -\nabla f_i + \frac{|\nabla f_i|^2}{|\nabla f_{i-1}|^2} S_{i-1} \tag{C4-21}$$

where ∇f_i is the gradient function for iteration i. Applying the Fletcher - Reeves method in training a Neural Network leads to converging of the network weights:

$$\Delta w_{kj} = \lambda S_i \tag{C4-22}$$

where S_i is given by:

$$S_i = -\left(\frac{\partial E}{\partial w_{kj}}\right)_i + \frac{\left|\left(\frac{\partial E}{\partial w_{kj}}\right)_i\right|^2}{\left|\left(\frac{\partial E}{\partial w_{kj}}\right)_{i-1}\right|^2} S_{i-1} \tag{C4-23}$$

The partial derivative of the error function with respect to the network weight is determined for the output layer and hidden layer using Back Propagation method discussed earlier. Substituting the Fletcher - Reeves direction into Equation (C4-22) gives:

$$\Delta w_{kj} = \lambda\left(-\nabla f_i + \frac{|\nabla f_i|^2}{|\nabla f_{i-1}|^2} S_{i-1}\right) \tag{C4-24}$$

if the momentum term is defined as follows:

$$\eta = \frac{|\nabla f_i|^2}{|\nabla f_{i-1}|^2} S_{i-1} \tag{C4-25}$$

Equation (C4-24) yields to the following equation:

$$\Delta w_{kj} = -\lambda \nabla f_i + \lambda \eta \tag{C4-26}$$

The Conjugate Gradient Method is similar to the Steepest Descent algorithm except that this method converges to the optimum solution by using an adjustable training rate λ and a momentum term η that is dependent on previous search direction.

APPENDIX D

BLOCK DIAGRAMS AND PROGRAMS

D.1 MATLAB Simulink Block Diagrams

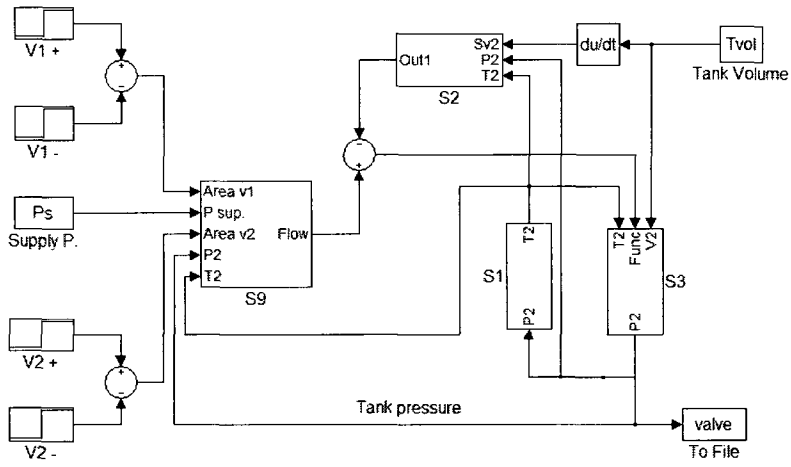

Figure D-1: MATLAB Simulink block diagram for the valve model

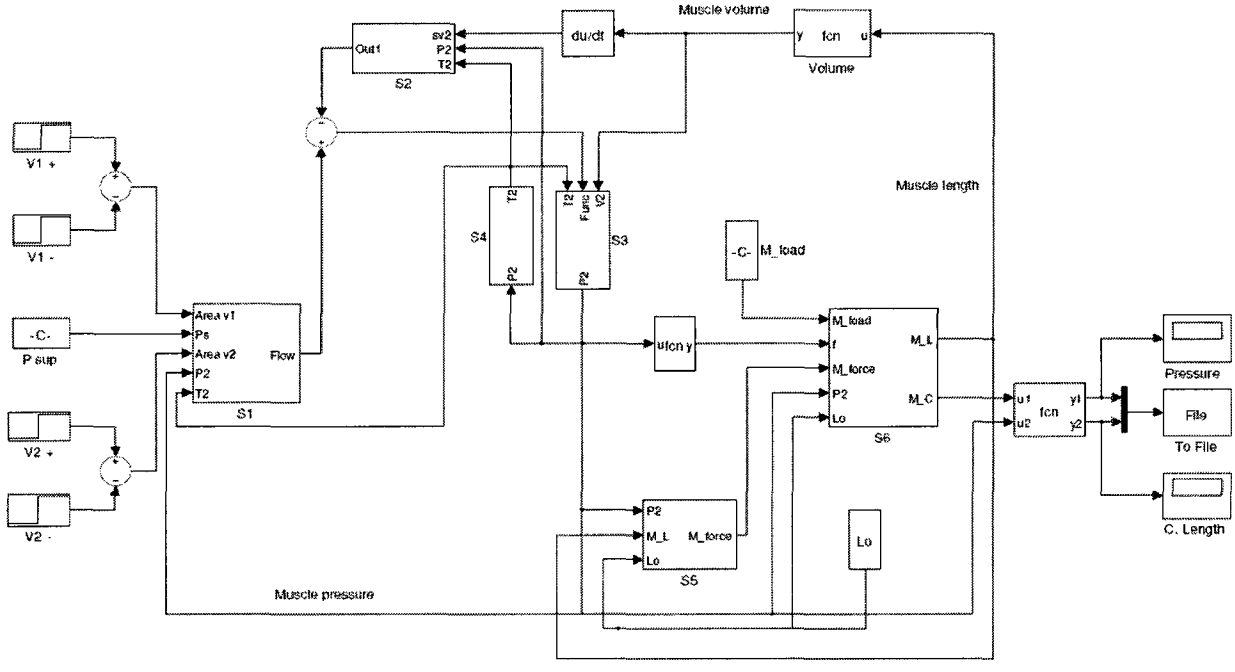

Figure D-2: MATLAB Simulink block diagram for the BPM dynamic model

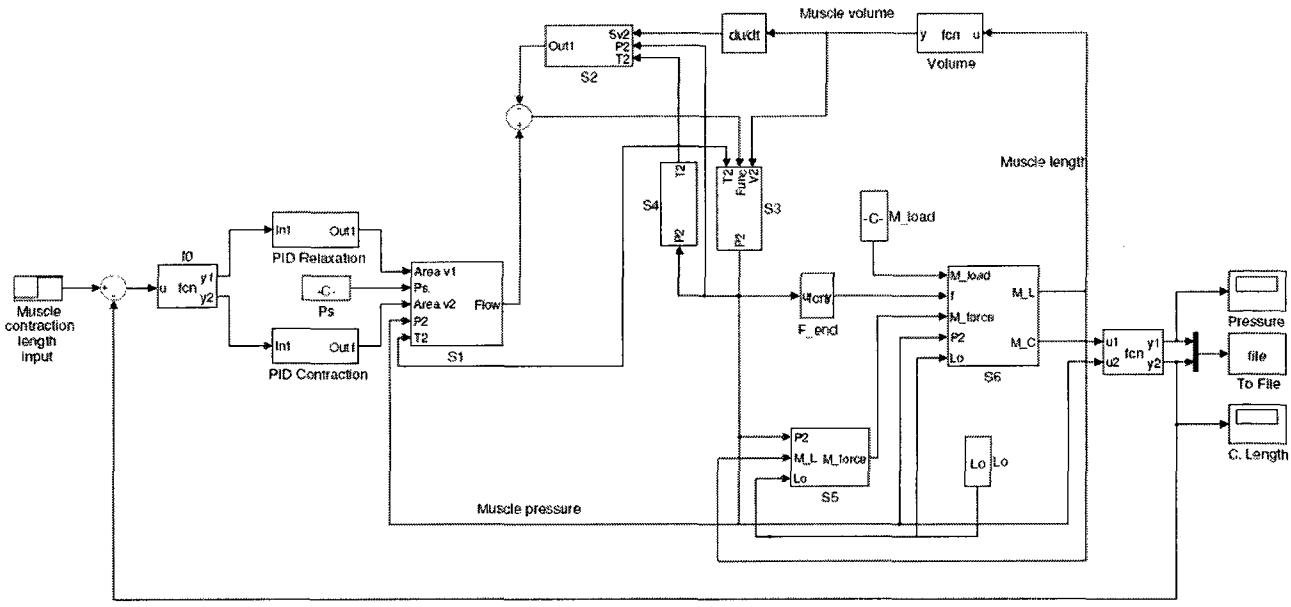

Figure D-3: MATLAB Simulink block diagram for the closed loop system

D.2 LS algorithm MATLAB code

```
% Least Squares Algorithm solution
% assuming a second order system as follows:
%
% y(k) = a1 y(k-1) + a2 y(k-2) + b1 u(k-1) + b2 u(k-2) + e(k)
%
% storing the experimental results in "Data" vector
% the system input sequence u is identified as follows:
u = Data(1,:);
% the system output sequence y is identified:
y  = Data(2,:);
% The regression vector FI that contains the input and output sequence is created as follows:
j=3;
  for i=3:993
  FI(:,j)=[y(i-1);y(i-2);u(i-1);u(i-2)];
  j=j+1;
  end
% the output sequence transpose is created as follows:
Y=y';

% the estimated LS solution parameters are calculated as follows:

Theta        = (FI*FI')^-1*(FI*Y)

% the estimate LS system output is calculated as follows:

Result(:,1)    = FI'*Theta;
```

D.3 Neural Network Programming Codes

MLP Neural Network (NNARX)

```
#include <stdio.h>
#include <math.h>
#include <stdlib.h>
#include <search.h>
#include <iostream>
#include <fstream>
#include <string.h>
#include <time.h>
using namespace std;
//      Functions used in the program
        void        first_last_node                 (void);
        void        open_file                       (void);
        void        compute_output                  (void);
        double      initialize_weight               (double);
        void        init_variables                  (void);
        void        compute_error_steepest_descent  (void);
        void        compute_error_fletcher_Reeves   (void);
        void        reset_delta                     (void);
        void        compute_egrad                   (void);
        void        change_weights                  (void);
        void        print_weights                   (void);
        int         get_rand_line                   (double *array,char *filename);
//      Defining Constants
        #define  MAX                50      // Maximum number of total nodes
        #define  MAXHLAYERS         5       // Maximum number of hidden layers
```

```
#define  EPSILON                    0.5     // Network learning constant
#define  MOMENTUM                   0.2     // Momentum term
#define  ECRIT                      0.01    // Allowable output error for the network
#define  NUMBER_OF_ROWS             335     // number of rows in training file
#define  BUF_SIZE                   400     // buffer size for training data
#define  NUMBER_OF_COLUMNS          3       // number of columns in training file
//       Declare & initialize variables
         int nunits;                                    // total number of nodes in network
         int ninputs                    = 3;            // total number of input nodes in network
         int nhiddenN                   = 3;            // total number of hidden nodes per layer in network
         int nhiddenL                   = 1;            // total number of hidden layers in network
         int noutput                    = 1;            // total number of output nodes in  network
         double  error          [MAX];                  // Error of each output node
         double  delta          [MAX];                  // Error Derivative with respect to input
         double   egrad         [MAX] [MAX];            // Partial derivative of error over partial derivative of
                                                        // weight (error gradient)
         double  begrad         [MAX];                  // Bias Error gradient
         double  dweight        [MAX] [MAX];            // (i+1) weight
         double  dbias          [MAX];                  // (i+1) bias
         double  weight         [MAX] [MAX];            // weight of each network connection
         double  bias           [MAX];                  // threshold
         double  netinput       [MAX];                  // Sum of weight*activation for a node
         double  activation     [MAX];                  // Output Value of a node
         double  target         [MAX];                  // Desired network output Value
         int     first_node_to  [MAX];                  // connection order
         int     last_node_to   [MAX];                  // connection order
         double  ERROR=0;                               // Sum of error
         double  VARERROR               = 0;            // Error Variation, E(t+1) - E(t)
         double  PASTERROR              = 0;            // Past Error, E(t-1)
         int     z                      = 0;
```

```
        int     line_number             = 335;
        double  line[3];
        char    buffer[BUF_SIZE];
        char    current_char;
//      Main Function which will call other functions
 int main()
  {
//      Initialized the random number generator
        time_t current_time;
        struct tm * timeinfo;
        time(&current_time);
        timeinfo = localtime(&current_time);
        srand((unsigned int)current_time);
//      Calculating the number of nodes in the network "nunits"
        nunits = ninputs + noutput + nhiddenN*nhiddenL;
//      output file, Network results are saved in an .csv format
        FILE *output_file_ptr;
        output_file_ptr = fopen("output.csv","w");
if (output_file_ptr == NULL)
    {
        printf("Error, cant open the file!\n");
        return (2);
    }
// Calling 3 functions to initialize network variables
                first_last_node();              // initialize connection orders
                initialize_weight(0.9);         // initialize random value to weight
                init_variables ();              // initialize variable values to zero
// for loop that repeat the training as much as necessary
        int z=0;
        for (int x=0; x<1000000; x++)
```

```
        {
                z++;                    // loop counter
//      for loop that execute the network calculation for the
//      training data one at a time.
                for ( int i=0; i < 200;)
                {
//      Read lines randomly from a file
                get_rand_line(line,"training_data.csv");
                        activation[0] = line[0];
                        activation[1] = line[1];
                        activation[2] = line[2];
                        target[0]           = line[2];
                        i++;
// for loop that could repeat a single training data consequently
// as much it is desired
                        for ( int a=0; a < 1; a++)
                        {
                                compute_output();
                                compute_error_steepest_descent ();
                                compute_egrad ();
                                change_weights();
                        }
                }
// writing to file the sum of error and its variance
                if ( ERROR < ECRIT)
                {
                        print_weights ();
                        break;
                }
                VARERROR = ERROR - PASTERROR;
```

```
                PASTERROR = ERROR;
                fprintf(output_file_ptr, " %f\n", ERROR);
                printf("i is: %13d SUM ERROR IS: %13f\n",z,ERROR);
                ERROR = 0;
        }
        fclose(output_file_ptr);
        return (0);
        }
//*****************************************************************************************
//* Function: first_last_node
//* Description: This function define the order of first/last node number that will feed to the
//* next node
//*****************************************************************************************/
        void    first_last_node(void)
        {
                int i=0;
                int j=0;
//      loop that identifies the first nodes and last node that is connected to the next row node
//      Assuming one Hidden layer
                for ( j= (ninputs+(i*nhiddenN)); j< (nunits - noutput-(nhiddenL-i-1)*nhiddenN) ; j++)
                        {
                        first_node_to [j]= 0;
                        last_node_to [j]= ninputs+i*nhiddenN -1;
                        }
//
                for (i=1;i<=nhiddenL;i++)
                {
                        for ( j= ninputs+(i*nhiddenN); j< nunits - noutput-(nhiddenL-i-1)*nhiddenN ; j++)
{
                                first_node_to [j]= ninputs+((i-1)*nhiddenN);
```

```
                    last_node_to [j]= (ninputs+i*nhiddenN) -1;
                    }
                }
        }
//*****************************************************************************************
//* Function: initialize_weight
//* Description: This function randomly initialize all weight connection within a desired range
//* Note: This function expect a double value for random number generator
//*****************************************************************************************/
        double initialize_weight (double w)
        {
                register int i, j;
                srand( 2635 );
                for (i= 0; i< nunits; i++)
                {
                        for (j=first_node_to[i] ; j<last_node_to[i]+1;j++)
                        {
         weight[i][j] = ( ( double ) rand() / RAND_MAX ) * 2*w + w;
                        }
// initialise all threshold randomly
        bias[i] = ( ( double ) rand() / RAND_MAX );
                }
                return 0;
        }
//*****************************************************************************************
//* Function: init_variables
//* Description: This function randomly initialize network variables
//*
*****************************************************************************************/
        void init_variables (void)
```

```
{
        register int i,j;
        for (i=0; i<nunits; i++)
        {
                delta[i]=0.0;
                error[i]=0.0;
                begrad[i]=0.0;
                for (j=0; j< nunits; j++)
                {
                        egrad[i][j]=0.0;
                }
        }
}
//*****************************************************************************************
//* Function: compute_output
//* Description: This function computes the output of each nodes
//*****************************************************************************************/
        void compute_output(void)
        {
                register int i,j;
                for (i=ninputs; i<nunits; i++)
                {
                        netinput[i] = bias[i];
                        for (j=first_node_to[i]; j<last_node_to[i]+1;j++)
                        {
                                netinput[i] += activation[j]*weight[i][j];
                        }
                        activation[i] = 1.0 / (1.0 + exp((-1.0) * netinput[i]));
                }
        }
```

```
//*****************************************************************************************
//* Function: compute_error_steepest_descent
//* Description: This function achieve the recursive computation of error and delta term
//*****************************************************************************************/
        void compute_error_steepest_descent (void)
        {
                int i,t,j;
                for ( i = ninputs; i<nunits; i++)
                        error[i]=0.0;
                for (i= nunits - noutput,t=0; i<nunits; t++,i++)
                {
                        error[i] = target[t] - activation[i];
//      Mean square error for output node
                        ERROR += error[i]*error[i]/2;
                }
//      propagate the error back to the hidden nodes
                for (i= nunits-1;i>=ninputs;i--)
                {
//      delta(k) = - dE/dy * dy/dx
                        delta[i] = error[i]*activation[i]*(1.0 - activation[i]);
                        for (j = first_node_to[i]; j< last_node_to[i]+1;j++)
                        {
                                error[j] += delta[i]*weight[i][j];
                        }
                }
        }
//*****************************************************************************************
//* Function: compute_egrad
//* Description: This function compute weight error derivative (wed) and bias error derivative (bed)
//*****************************************************************************************/
        void compute_egrad (void)
```

```
        {
                register int i,j;
                for (i=ninputs; i<nunits; i++)
                {
                        for (j = first_node_to[i]; j< last_node_to[i]+1;j++)
                                egrad[i][j] += delta[i]*activation[j];
                                begrad[i] += delta[i];
                }
        }
//*****************************************************************************************
//* Function: change_weights
//* Description: This function update the weight values of the network
//*****************************************************************************************/
        void change_weights (void)
        {
                register int i, j;
                for (i=ninputs; i<nunits;i++)
                {
                        for (j = first_node_to[i]; j< last_node_to[i]+1;j++)
                        {
                                dweight[i][j] = EPSILON * egrad[i][j] + MOMENTUM * dweight[i][j];
                                weight[i][j] += dweight[i][j];
                                egrad[i][j] = 0.0;
                        }
//              bias term
                dbias[i] = EPSILON * begrad[i] + MOMENTUM * dbias[i];
                bias[i] += dbias[i];
                begrad[i] = 0.0;
                }
        }
```

```
//*****************************************************************************************
//* Function: print_weight
//* Description: This fuction give final weight and bias values for network validation purpose
//*****************************************************************************************/
void print_weights (void)
        {
                        FILE *output_file_ptr1;
        output_file_ptr1 = fopen("last_weight.csv","w");
                        if (output_file_ptr1 == NULL)
            {
         printf("Error, cant open the file!\n");
 //          return (0);
                    }
                register int i, j;
                for (i=ninputs; i<nunits;i++)
                {
                        for (j = first_node_to[i]; j< last_node_to[i]+1;j++)
                        {
                        printf("Last weight IS: %10d%10d%10f\n",i,j,weight[i][j]);
                        fprintf(output_file_ptr1,"Last weight IS:, %10d , %10d, %10f\n",i,j,weight[i][j]);
                        }
                        printf("Last Bias IS: %10d  %10f\n",i,bias[i]);
                        fprintf(output_file_ptr1,"Last Bias IS:, %10d , %10f\n",i,bias[i]);
                }
                        fclose(output_file_ptr1);
        }
//*****************************************************************************************
//* Function: get_rand_line
//* Description: This function read a line randomly from a file
//* Note: This function expect the random number generator to be initialized before it is called
```

```
//*****************************************************************************************/
int get_rand_line(double *array,char *filename)
{
        int i=0;
        int j=0;
        int k=0;
        char buffer[BUF_SIZE];
        char current_char;
        int line_number;1+rand()%(NUMBER_OF_ROWS);
        FILE * tab_del_file = fopen(filename, "r" );
        //Get a line number
        line_number=1+rand()%(NUMBER_OF_ROWS);
        //Verify if the file has been open properly
        if(tab_del_file != NULL){
                //Go to the desired line
                for(i=0;i<line_number;i++){
                        //Read the tabdelimited format that you want
                        //Read each column
                        for(k=0;k<NUMBER_OF_COLUMNS;k++){
                                j=0;
                                current_char=fgetc(tab_del_file);
                                while(current_char!=',' && current_char!='\n' && current_char!=EOF &&
j<BUF_SIZE-1){
                                        buffer[j]=current_char;
                                        j++;
                                        current_char=fgetc(tab_del_file);
                                }
                                //Unexpected end of file and buffer overflow
                                if((current_char==EOF && k!=2) ||j==BUF_SIZE-2){
                                        fclose(tab_del_file);
                                        return -1;
```

```
                    }
                    //Terminate the string
                    buffer[j]='\0';
                    //Convert the string to a double
                    array[k]=strtod(buffer,NULL);
                }
            }
            //Close the file after the reading is done
            fclose(tab_del_file);
        }
}
```